



HAL
open science

Effect of membrane content on the acoustical properties of three-dimensional monodisperse foams: Experimental, numerical and semi-analytical approaches

van Hai Trinh

► To cite this version:

van Hai Trinh. Effect of membrane content on the acoustical properties of three-dimensional monodisperse foams: Experimental, numerical and semi-analytical approaches. Acoustics [physics.class-ph]. Université Paris-Est, 2018. English. NNT: . tel-01853287

HAL Id: tel-01853287

<https://hal.science/tel-01853287>

Submitted on 2 Aug 2018

HAL is a multi-disciplinary open access archive for the deposit and dissemination of scientific research documents, whether they are published or not. The documents may come from teaching and research institutions in France or abroad, or from public or private research centers.

L'archive ouverte pluridisciplinaire **HAL**, est destinée au dépôt et à la diffusion de documents scientifiques de niveau recherche, publiés ou non, émanant des établissements d'enseignement et de recherche français ou étrangers, des laboratoires publics ou privés.

Université Paris-Est
École doctorale Sciences, Ingénierie et Environnement

THÈSE

présentée et soutenue publiquement le 11 juillet 2018

pour l'obtention du

Doctorat de l'Université Paris-Est

Discipline: mécanique

par

Van Hai TRINH

**Effect of membrane content on the
acoustical properties of three-dimensional
monodisperse foams: Experimental,
numerical and semi-analytical approaches**

Composition du jury

K. ATTENBOROUGH	Open University (UK)	Rapporteur
F. TOPIN	Aix-Marseille Université (FR)	Rapporteur
N. DAUCHEZ	Université de Technologie de Compiègne (FR)	Examineur
C. PERROT	Université Paris-Est (FR)	Directeur
J. GUILLEMINOT	Duke University (USA)	Co-directeur
V. LANGLOIS	Université Paris-Est (FR)	Co-directeur

Acknowledgments

First of all, I would like to express my special appreciation and thanks to my supervisor, M^dC. (Habil.) Camille PERROT. I have learned a lot from him, both professionally and personally. Thank you *Camille*, for offering me the opportunity to work on a very interesting project. I would like to deeply thank to my first co-supervisor, Asst. Prof. Johann GUILLEMINOT, who significantly helped me addressing the mathematical aspects of this work. I would also like to provide my thanks to Dr. Vincent LANGLOIS, my second co-supervisor. I was very pleased by his suggestions and contributions in this research project.

Collaboratively, I would like to provide my thanks to Dr. Olivier PITOIS for his support in terms of materials elaboration and experimental characterization. I am very pleased to thank him for his valuable comments and contributions. I also thank two former Ph.D. candidates, Dr. Minh Tan HOANG and Dr. Hoang Tuan LUU, for their help and valuable shares at the beginning of this project.

I would like to thank the members of my dissertation committee, Prof. Keith ATTENBOROUGH and Dr. Frédéric TOPIN, for having accepted to serve as referees, and Prof. Nicolas DAUCHEZ, for having accepted to examine this work.

Personally, I deeply thank my parents and my in-laws for their continuous support during the three difficult years I have spent far away from home. For her wonderful understanding during these years, I express my gratitude to Anh Tuyet, my lovely wife. Thank you for late night and early morning chats, and for daily taking care of and educating our daughters, Hai Anh and Hai Yen. My awesome daughters, a source of unending love and motivation, have been interminably awaiting the day when the project would be completed and I would be back home. I would never have done this without their love and encouragement, and I am really thankful to all my family.

Finally, I gratefully acknowledge the financial support from the Government of Vietnam (Project 911). Also, I would like to thank all my friends and colleagues at the Le Quy Don Technical University for their support during the course of this doctoral project.

Paris, July 2018

Van Hai TRINH

Abstract

Noise pollution has become one of the major issues of modern times. Acoustical panels made of solid foamy materials can be used to absorb the noise in a specific frequency range. Modeling the acoustic properties of real foam-based absorbers from the description of their local geometry is essential to achieve desired acoustic target and enable design of these materials from the manufacturing process.

This work is mainly concerned with the determination of the acoustic properties of foams. This is a project carried out as part of a collaboration between a team of physico-chemistry of foams in charge of the development of model materials (Navier laboratory UMR 8205 CNRS) and a team of acousticians responsible for the study of their acoustic properties (MSME laboratory UMR 8208 CNRS). This thesis is structured around three main parts, the content of which is summarized below. 1) The first part deals with the generation of response surfaces by polynomial approximations, in order to have an intermediate model between the micro-macro finite element model and the macroscopic response. Instead of calling the finite element model systematically in an optimization work, we use the response surface that contains the information associated with finite element calculation points and the corresponding interpolations. This manuscript was published in the *AAuA* journal as a fast track publication. 2) The second part deals with a finite element calculation in which a large number of realizations are carried out in order to take into account all the possible combinations when one has fine experimental characterization at the microstructure scale and that one seek to determine the properties of the foam with precision. The manuscript is in preparation and a possible journal for the publication of this manuscript is the journal *Materials and Design*. 3) The third part focuses on the development of a semi-analytical model defined from an available formula to predict the permeability of a circular orifice in a thin plate. This model, used in an appropriate way, makes it possible to calculate the permeability of foams with a constant bubble size but a tuned membrane content. Numerical validations by finite element computations are proposed. The article has been accepted for publication in the journal *Physical Review E*. A general introduction (statement of the problem, theoretical and methodological framework, continuity and complementarity of the papers) and a general conclusion complete these three parts, and make it possible to discuss these contributions.

Keywords: Membrane, monodisperse foams, absorbing materials, transports, acoustics, multiscale method, pore-network simulation, surrogate models.

Résumé

La pollution sonore est devenue l'un des problèmes majeurs des temps modernes. Des isolations acoustiques de protection, telles que des matériaux moussants solides, peuvent être utilisées pour absorber le bruit dans une gamme de fréquences spécifique afin de garantir le silence requis. La modélisation des propriétés acoustiques des absorbeurs réels à base de mousse à partir de la description de leur géométrie locale est essentielle pour atteindre la cible acoustique souhaitée, tandis que la conception de ces matériaux à partir du procédé de fabrication est encore une tâche difficile.

Ce travail concerne principalement la détermination des propriétés acoustiques de mousses. Il s'agit d'un projet mené dans le cadre d'une collaboration entre une équipe de physico-chimie des mousses chargée de l'élaboration de matériaux modèles (Laboratoire Navier UMR 8205 CNRS) et une équipe d'acousticiens chargée de l'étude de leurs propriétés acoustiques (Laboratoire MSME UMR 8208 CNRS). Cette thèse s'articule essentiellement autour de trois parties principales, dont le contenu est résumé ci-dessous. 1) La première partie porte sur la génération de surfaces de réponse par des approximations polynomiales, dans le but de disposer d'un modèle intermédiaire entre le modèle éléments finis micro-macro et la réponse macroscopique. Au lieu d'appeler le modèle éléments finis systématiquement dans un travail d'optimisation, on a recouru à la surface de réponse qui contient l'information associée aux points de calcul éléments finis ainsi que les interpolations correspondantes. Ce manuscrit a été publié dans le journal *AAuA* sous forme de communication rapide. 2) La deuxième partie, porte sur un calcul éléments finis dans lequel un grand nombre de réalisations sont menées de manière à prendre en compte l'ensemble des combinaisons possibles lorsque on dispose de caractérisation expérimentales fines à l'échelle de la microstructure et que l'on souhaite connaître la réponse de la mousse avec précision. Le manuscrit est en préparation et la revue visée pour ce dernier manuscrit est le journal *Materials and Design*. 3) La troisième partie porte sur la mise au point d'un modèle semi-analytique défini à partir d'une formule disponible pour prédire la perméabilité d'une plaque infinie percée par un trou de surface connue. Ce modèle, utilisé de manière appropriée, permet de calculer la perméabilité de mousses dont la taille de bulles est constante et le taux de fermeture de membranes variable. Des validations numériques par éléments finis et expérimentales sont proposées. L'article a été accepté pour publication dans la revue *Physical Review E*. Une introduction générale

(problématique, cadre théorique et méthodologique, continuité et complémentarité des articles) et une discussion générale complètent ces trois parties, et permettent de mettre en perspectives ces contributions par rapport à la littérature existante sur le sujet.

Mots-clés: Membrane, mousses monodispersées, matériaux absorbants, transports, acoustique, méthode multi-échelle, simulation de pores-réseaux, modèles de substitution.

Contents

Acknowledgment	ii
Abstract	iii
List of Tables	xi
List of Figures	xiii
Nomenclature	xxi
I General introduction	1
I.1 Introduction	1
I.2 Study objectives and thesis organization	5
I.2.1 Study objectives	5
I.2.2 Thesis organization	6
I.3 Literature review	7
I.3.1 Models of acoustical porous materials	8
I.3.2 Surrogate-based modeling methodology	12
I.3.3 Characterization of porous media	14
I.4 Numerical approach for modeling acoustical cellular materials	22
I.4.1 Reconstruction of local ordered foam structures	22
I.4.2 Numerical estimations of macroscopic properties	25
II On the construction of multiscale surrogates for design optimization of acoustical materials	31
II.1 Introduction	33

II.2	Methodological aspects	34
II.3	Numerical results	35
II.3.1	Reference solution map	35
II.3.2	Surrogate analysis	37
II.4	Conclusion	40
III	Tuning membrane content of sound absorbing cellular foams: Experimental evidences and multi-scale simulations	41
III.1	Introduction	45
III.2	Membrane induced-effect on sound absorption: Experimental evidence	47
III.2.1	Elaboration of controlled polymer foams	48
III.2.2	Characterization of the foam samples	48
III.2.3	Acoustic measurements	53
III.2.4	Experimental results and discussions	54
III.3	Distinction between aperture size and fraction of closed windows: Numerical simulations	56
III.3.1	Unit cell modeling approach	56
III.3.2	Calculations of visco-thermal parameters	60
III.3.3	Calculations of sound absorbing properties JCAL	63
III.3.4	Results and discussion	63
III.4	Conclusion	68
IV	Permeability of solid foam: Effect of pore connections	73
IV.1	Introduction	76
IV.2	Numerical simulations of foam permeability	77
IV.2.1	FEM simulations of fluid flow	77
IV.2.2	Pore-network simulations	79
IV.3	Results and discussion	81
IV.3.1	Effect of the aperture size	81
IV.3.2	Effect of closed windows: The bond percolation problem in foam	83
IV.3.3	Effective medium model for permeability	89

IV.4 Conclusion	91
V To go beyond PUC modeling	97
V.1 Representative elementary volume of disordered structures	97
V.2 Applications and discussions	100
V.2.1 Foamy structures	100
V.2.2 Computational example	104
V.2.3 Summary of the numerical framework	109
VI Conclusions and future work	111
VI.1 General conclusion	111
VI.2 Future work	113
A A systematic link between microstructure and acoustic properties of foams: A detailed study on the effect of membranes	115
Bibliography	117

List of Tables

I.1	Coefficients in the Delany-Bazley, Miki, Mechel-Ver, and Allard-Champoux empirical models.	9
I.2	The characterized parameters of the granular material sample.	22
III.1	Microstructural characteristics of foam samples.	52
III.2	Transport parameters of the elaborated foam samples.	55
III.3	Equivalent configurations in various symmetry conditions.	59
III.4	PUC characteristics corresponding to foam sample S1-S10. In particular, it illustrates the huge discrepancy between the total number of possible configurations \mathcal{N}_t and the reduced number of reference configurations \mathcal{N}_r	61
IV.1	Structures of simplest closed clusters having k open windows and $k + 1$ pores, and fraction of pores P_k contained within such cluster (= total number of pores being in a closed cluster having k open windows and $k + 1$ pores/total number of pores, N_p). In the “Closed cluster” drawing, open windows having a probability x_{ow} , and closed windows (thin gray lines) have a probability $(1 - x_{ow})$ to black lines.	88
IV.2	Coefficients σ_w for used lattices and weakly disordered foam. Note that for SC, BCC or Kelvin lattices, σ_w is isotropic.	89
V.1	Algorithm for generating the close random packing of equal hard spheres.	100
V.2	The comparison of computational time between two numerical methods. The direct work is conducted with 15 different frequencies.	108

List of Figures

I.1	(Color online) Different acoustical material samples: polymer foam (a), fibrous material (b), granular layer (c), epoxy foam panel (d), and microperforated panel (MPP) (e).	2
I.2	(Color online) The ingoing and the outgoing plane waves at a plane interface between air and a porous material: the material is fixed to an impervious rigid wall (a), and there is a gap of air of thickness d_a between the material and the rigid wall (b). M , M' and M_1 indicate the locations measured the pressures related to estimations of SAC.	3
I.3	(Color online) Measured sound absorption coefficients at normal incidence of various acoustic material samples shown in Figure I.1. The results are shown for: polymer foam (black), fibrous (yellow), MPP (gray), granular sample (magenta), and epoxy panel (green), and the corresponding thicknesses of [20, 20, 1, 20 and 3] mm, respectively. Noted that all measurements were performed by using a three-microphone standing impedance tube shown in Figure I.11(a). Here, there is only a cavity depth d_a of 7 mm used in the case of MPP panel.	3
I.4	(Color online) Morphology of membrane foam structure.	4
I.5	The approximate solution map $(\xi_1, \xi_2) \mapsto \hat{\mathbf{q}}_p(\xi_1, \xi_2)$ (middle) is compared with the reference solution map $(\xi_1, \xi_2) \mapsto \mathbf{q}(\xi_1, \xi_2)$ (left), these results are shown for $p = 15$ and $n_Q = 12$. The corresponding relative error is measured as $\mathcal{D}_p(\xi_1, \xi_2) = \mathbf{q}(\xi_1, \xi_2) - \hat{\mathbf{q}}_p(\xi_1, \xi_2) / \mathbf{q}(\xi_1, \xi_2) $ (right).	15
I.6	Photos of a Hitachi S-3000N variable-pressure Scanning Electron Microscope (VP-SEM) (a) and a LEICA MZ6 Binocular Microscope (b).	16
I.7	Photographs of the local microstructures of a real cellular foam (a) and a fibrous material sample (b).	16
I.8	Distributions of anisotropy degree (a) and normalized cell size (b) as experimentally determined by scanning electron microscopy.	17
I.9	1172 X-ray Microtomograph Skyscan ^[94]	18

I.10	Main steps of the reconstruction process by x-ray micro computed tomography ^[25] : (left) Acquisition of classical radiographies, or “x-ray shadow images” of the real sample; (middle) Reconstruction of bidimensional cross sections of the real sample showing (i) “ring artifacts” and (ii) “starburst artifacts”; (right) Reconstruction of the three-dimensional image of an axial portion of the real sample, after binarisation of the two-dimensional images.	18
I.11	Picture of a standing impedance tube which can be used to measure the acoustic absorption coefficient at normal incidence and characterize material parameters of a semi-phenomenological model (a), picture of a device for measuring of the static airflow resistivity of porous materials (b).	21
I.12	Comparison between measured (line) and characterized (marker) results of normalized effective density (left part) and the normalized effective bulk modulus (right part). The results are obtained from a three-microphone standing tube measurement on the granular layer shown in Figure I.1(c).	21
I.13	The structural candidates (middle and right panels) of foam based on the ideal space-filling cell (left panels). The Kelvin tetrakaidecahedron array (a), the Weaire-Phelan structure based on two kinds of cells, one is an irregular dodecahedron and the other is a hexagonal trapezohedron (b).	23
I.14	The idealized framework of foaming skeleton based on the Kelvin (top) and the Weaire-Phelan (bottom) pattern. The struts are treated as a cylindrical shape and connected to each other at a spherical node. The thin membrane (right parts) in closed-cell foams is idealized by an aperture film having a given closing rate at all cell windows.	24
I.15	The cell unit in Kelvin structure with different ligament shapes: equilateral triangular (left), concave (middle), and circular a variation of cross sectional area along the length (right).	25
II.1	Unit cell and FE mesh ($\phi = 0.97, r_c = 0.6$).	36
II.2	Reference solution map $(\phi, r_c) \mapsto A^{(n)}(\phi, r_c)$ at different frequencies (in Hz).	36
II.3	Graph of the error function $n_{\mathcal{Q}} \mapsto \varepsilon(n_{\mathcal{Q}})$ for $p = 5$ (circles), 10 (diamonds) and 15 (squares).	37
II.4	PDF of the relative error for $p = 15$ and for the set of frequencies shown in Figure II.2.	38

II.5	Solution map for the normal incidence sound absorption coefficient. Solid line: reference; cross markers: surrogate with $p = 10$; point markers: surrogate with $p = 15$. The results are shown for $r_c = 0.1$ (black), 0.2931 (green), 0.4862 (blue), 0.5966 (red), 0.7069 (magenta), and $\phi = 0.9124$ (left panel) and $\phi = 0.9745$ (right panel).	39
II.6	Plots of the averaged absorption coefficients, with $f_0 = 250$ and $f_1 = 5,000$ Hz. The maximum value in each chart is identified with a red cross.	39
III.1	Schematic description of the foaming process.	49
III.2	Characterizations of dried-gelatin foam materials: top view of foam sample (a), degree of anisotropy (b), membrane closure rate (c), and membrane thickness (d).	50
III.3	Morphological properties measured on foam samples for S1(\square), S2(\circ), S3(\diamond), S4(\times), S5(∇), S6(\triangleleft), S7(\star), S8(\triangleright), S9(\triangle), and S10(+). The results are shown for the normalized edge length distributions (a), the normalized face area distributions (b), and the distributions of faces with E edges (c).	51
III.4	Distribution function of the window closure rate measured on foam samples. The results are shown for: S1(\square), S2(\circ), S3(\diamond), S4(\times), S5(∇), S6(\triangleleft), S7(\star), S8(\triangleright), S9(\triangle), and S10(+).	52
III.5	Experimental setup of the three-microphone impedance tube method.	53
III.6	Effect of the mean closure rate on the sound absorption coefficient at normal incidence with a sample thickness of 20 mm and a rigid backing.	54
III.7	PUC: skeleton geometry (a) and pore-space mesh (b).	56
III.8	Illustration of some typical reconstructed PUC corresponding to microstructural characteristics of foam samples S1 to S10. Graphs of the periodic unit cell (a)–(k) corresponding to PUC1–10. Note that, for each PUC, only a configuration among many others is depicted.	57
III.9	(a) Reconstruction of a tetrakaidecahedron cell with a 2-dimensional pattern, direction of x axis is perpendicular with faces 1 and 4; (b) the possible configurations associated to PUC1 ($N_c^{sq} = 1$ and $N_c^{he} = 0$).	58
III.10	The symmetry property of the periodic unit cell.	59
III.11	Major steps of equivalent configuration calculation (a) and graphs associated to steps III. and IV. (b). This figure depicts the simple case where $N_c^{sq} = 1$ and $N_c^{he} = 0$	60

III.12	Dimensionless transport properties for: real foam samples (\times) and 2-parameter models: PUC computation (\circ), EM model (Δ). The mean aperture radius $\langle R_o \rangle$, calculated by including the closed windows ($R_o = 0$), is added (\square) and allows for a comparison with Λ/D_b . Note that the samples S1 to S10 are ordered by increasing mean closure rates. The error bars on computed values of macroscopic parameters are calculated by considering an error on the characterization of $\langle r_{c,o} \rangle$ equal to ± 0.05	64
III.13	Comparison of the dimensionless transports predictions obtained for PUC computations and: the HP method (a, b and c), or the DAD method (d, e and f). The results are shown for: PUC computation values (\circ), HP values (∇), and DAD values (Δ). Note that the samples S1 to S10 are ordered by increasing mean closure rate, $\langle r_c \rangle$	65
III.14	Sound absorption coefficients of samples: experiments (orange filled zone), PUC computations with $\phi = 0.98$ (blue filled zone with full line), PUC computations with $\phi = \phi_{o,computed}$ (red filled zone with dashed line). The results are shown from top to bottom as: foams S1 to S5 (left panels), and foams S6 to S10 (right panels). The curves are calculated by using the computed macroscopic parameters shown in Fig. III.12, and their uncertainty are related to the estimation of errors on macroscopic parameters calculated by considering an error on the characterization of $\langle r_{c,o} \rangle$ equal to ± 0.05	66
III.15	(a) Detail of the coordinates of the basic vertex in the 1/48th open unit cell having ligaments of equilateral triangular cross-section of edge size r and length of L . (b) Diagram as a top view of the skeleton showing the relations between the angular and length parameters at the node and several ligaments.	70
IV.1	PUC with fully open windows (a), with partially closed windows by the same aperture size(b), identical aperture rate (c), definitions of the aperture size t_o and the window size t_w (d).	77
IV.2	FEM macro-scale samples: skeleton mesh (a) and porosity mesh (b). For sake of visibility, a mesh of size $2\sqrt{2} \times 2\sqrt{2} \times 2$ (D_b units) is depicted.	78
IV.3	Network structures used in pore-network simulations.	80

IV.4 (a) FEM predictions at identical aperture size with $\phi = 0.98$, (b) FEM predictions at identical aperture rate for various ϕ , (c) permeability as a function of the mean wall apertures: FEM results (blue dot for identical aperture, green dot for identical rate, red cross for “no wall” foam with ϕ varying from 0.8 to 0.99), pore-network simulations with Sampson local permeabilities and $N_v = 14$ (blue line for identical aperture, green line for identical rate). Note that the mean wall aperture is calculated without including the four square windows, which are parallel to the macroscopic flow direction $\langle t_{o,eq} \rangle / D_b = (2t_{o,sq} + 8t_{o,hex}) / 10D_b$	82
IV.5 Dimensionless permeability $K(x_{ow})/K(1)$ as a function of the open window fraction x_{ow} for FEM simulation (black square) and pore-network simulations (blue cross and red dot) on samples mixing two local permeabilities with various ratios k_{hex}/k_{sq} and having a Kelvin structure ($N_v = 14$). Error bars are calculated using (maximal value–minimal value)/2.	83
IV.6 Pore-network simulations: Highest of the largest cluster of the interconnected pores (black diamond) and fraction of open porosity (green diamond) as a function of the open window fraction x_{ow} for $N_v = 14$ and large samples $N_p \sim 10^6$. Green line corresponds to fraction of open porosity calculated by using Eq. (IV.6a).	84
IV.7 Pore-network simulations: (a) dimensionless permeability $K(x_{ow})/K(1)$ as a function of the open window fraction x_{ow} for various neighbor pore number N_v (arrows point to the abscissa $x_{ow} = x_{ow}^* = 2/N_v$); (b) the same data with another abscissa $(x_{ow} - x_{ow}^*) / (1 - x_{ow}^*)$	85
IV.8 Fraction of closed porosity, $1 - R_{op}$ (a) and excess fraction of open windows within the open pore space (b) as a function of the reduced fraction of open windows for various neighbor pore numbers N_v and large sample ($N_p \sim 10^6$). Dashed lines correspond to theoretical curves calculated in considering the first simplest closed clusters i.e., Eqs. (IV.5a) and (IV.5b). Full line corresponds to curves calculated by using approximate formulas [Eqs. (IV.6a) and (IV.6b)].	86
IV.9 Pore-network simulations: (a) $(x'_{ow} - x_{ow}^*) / (1 - x_{ow}^*)$ as a function of open window fraction x_{ow} for various neighbor pores number N_v , (b) Open porosity fraction (dashed line) and open porosity fraction without dead ends (full line) as a function of the open window fraction x_{ow} for $N_v = 6$ (black) and $N_v = 14$ (green).	87
IV.10 Comparison between EM model with network simulations (black diamond) for various neighbor pore numbers. “EM0” (dashed blue line) is based on the global open window fraction [Eq. (IV.9)], and “EM1” (red line) is based on the open window fraction within pore space [Eq. (IV.10)].	90

IV.A.1 (a) Cross-section of foam, (b) geometrical of a half pore representative of pores contained inside the foam cross section. Note that we have to consider $n + 1$ configurations for the position p of the window associated with the permeability k_i . Figure depicts the case $p = 2$	93
IV.A.2 For each lattice, bonds per unit cross section (gray area) considered for the calculation of σ_w . A couple $(\alpha_p, \text{fraction of bonds } p_b \text{ included within cross section})$ are associated to each bond. σ_w is calculated by $\sigma_w = \sum \alpha_p p_b D_b^2 / \text{area}$	94
IV.A.3 Comparison of EM model predictions (full line) to network simulations (cross) with $N_v = 14$	95
V.1 (left) Close packed configuration at a density $\eta_p = 0.612$ for a random packing of 1024 mono-sized spheres, and (right) the corresponding random foam with a Voronoi partitioning.	98
V.2 Three-dimensional solid foam skeleton representing the interconnected polyhedrons from the Voronoi tessellation (left part) and detail of a typical polyhedron with a focusing on its vertex interconnection (right part).	99
V.3 Graphs of finite element model of skeleton frame (left part, i.e., 1 379 316 tetrahedral elements) and pore domain (right part, i.e., 1 660 493 tetrahedral elements). For the sake of visibility, these FE meshes are created from a quarter of the assembled foam presented in Figure V.2, and here they present an open cell foam structure having a porosity of 0.914.	101
V.4 Distribution of cells with F faces (left) and faces with E edges (right) in compared with Matzke's experimental data and numerical simulations provided by Kraynik and co-workers.	102
V.5 Graphs of the normalized cell volume (left part) and the normalized edge length (right part) distributions of Voronoi random foam in compared with previous numerical works.	102
V.6 Graphs of multi-sized disc packing with the Gaussian (a), Gama (b), and graded (c) distributions, and the corresponding Voronoi patterns of 2D foam structure (d,e,f), respectively.	103
V.7 Unit cell finite meshes: a model of 269 931 tetrahedra used to open-cell structure (a), and a model of 469 358 tetrahedra used for the closed-cell one (b).	105

V.8	Asymptotic fields for the representative element volume. Hybrid method: (a) low-frequency scaled velocity field $\mathbf{k}_{oxx} [\times 10^{10} \text{ m}^2]$, (b) high-frequency scaled velocity field $\mathbf{E}_x / \nabla \varphi [-]$ for an external unit field \mathbf{e}_x , and (c) low-frequency scaled temperature field $\mathbf{k}'_0 [\times 10^{10} \text{ m}^2]$. Direct method: [(d,e,f)] and [(g,h,i)] are respectively shown for real parts of dynamic viscous and thermal permeability distributions $\mathbf{k}_{xx} [\times 10^{10} \text{ m}^2]$ and $k' [\times 10^{10} \text{ m}^2]$ at three frequencies 40 Hz, 2000 Hz, and 5000 Hz (from left to right).	106
V.9	Real (left) and imaginary (right) parts of the effective density. The results are shown for: hybrid numerical (continuous lines), direct numerical (circle symbols) methods, and open-cell foam (thin objects), and closed-cell foam (thick objects).	107
V.10	Real (left) and imaginary (right) parts of the effective bulk modulus. The indicated legends are the same as illustrated in Figure V.9.	107
V.11	The sound absorption coefficient at normal incidence of the foams obtained from hybrid (lines) and direct (circles) simulations. Thin and thick objects are for the foam without and with membranes, respectively. The sample thickness is equal to 25 mm.	108

Nomenclature

Most acronyms and variables used are described within the section that they are introduced. Below, the more frequently occurring ones are presented.

Notion	Definition
$A^{(n/d)}(\omega)$	Normal incidence/diffuse field sound absorbing coefficient
A_{po}, A_i	Area of window face
A_{el}	Area of open aperture
A_s	Cross-sectional area of sample
c_0	Sound speed in air
C_v	Specific heat at constant pressure
C_p	Specific heat at constant volume
C_{gel}	Gelatin concentration
D, D_b	Cell size
\mathcal{D}_p	Relative error
\mathcal{D}	Center distance of two spheres
d_{in}, d_{out}	Diameter of spherical particle
d_a	Air depth between rigid wall and sample
E	Number of edges per cell face
F	Number faces per cell
f	Frequency
$\mathcal{F}, \mathcal{F}'$	Dimensionless viscous and thermal shape functions
H_{sp}	Height of interconnected pores
H_{ip}	Heights of pores
J	Cost function
K_a	Module adiabatic air incompressibility
$K(\omega)$	Dynamic bulk modulus
K	Global permeability
k_0	Static viscous permeability
k'_0	Static thermal permeability
$\underline{\mathbf{k}}$	Dynamic viscous permeability
\underline{k}'	Dynamic thermal permeability

Notion	Definition
$k(\omega)$	Wave number
k_i	Local permeability
\bar{k}	Mean local permeability
L_l, L_{li}	Length of ligament
M, M'	Non-dimensional shape factors
$\mathcal{N}_t, \mathcal{N}_r$	Configuration numbers
N_o, N_c	Number of partially and fully closed windows in unit cell
N_{pr}	Prandtl number
N	Number of spheres
\mathbb{N}	Natural numbers
N_{pr}	Prandtl number
N_{ow}	Number of open windows
N_p	Total number of pores
N_v	Maximal numbers of neighbor pores
n_Q	Number of quadrature rule
n, d	Number of dimensions
\mathcal{P}	Distribution function
P, P'	Non-dimensional shape factors
P_0	Atmospheric pressure
P_{α_i}	Legendre polynomial of order α_i
P_k	Fraction of pores
p	Sound pressure
p	Order of polynomial expansion
Q	Volume fluid flow rate
\mathbb{R}	Euclidean space
r	Ligament size
r_c	Membrane closure rate
R_{op}	Fraction of percolating porosity
t_w	Windows size
t_o	The size of the wall aperture
u	Local fluid temperature field
\mathbf{v}	Local fluid velocity field
x_o, x_c	Fraction of partially and fully closed windows
x_{ow}	Fraction of open windows
x_{ow}^*	Critical concentration
x'_{ow}	Fraction of open windows
x_p	Percolation threshold
Z_0	Air impedance
$Z_s(\omega)$	Surface impedance
$Z_c(\omega)$	Characteristic impedance

Notion	Definition
$\langle \bullet \rangle$	Spatial average
Δ	Laplace operator
∇	Gradient operator
ΔP	Pressure drop
α	Multi-index
α	Normal incidence sound absorbing coefficient
α_i, β_i	Polynomial order
$\tilde{\alpha}(\omega)$	dynamic tortuosity
$\underline{\alpha}$	Average sound absorbing coefficient
α_∞	High frequency tortuosity
α_0	Static viscous tortuosity
α'_0	Static thermal tortuosity
β	Combination factor
$\tilde{\beta}(\omega)$	Dynamic compressibility
γ	Ratio of specific heats
δ	Membrane size
δ_{ij}	Kronecker delta
δ_{\max}	Maximum membrane size
δ_{ow}	Rate of aperture
ε	Scale ratio
η	Air dynamic viscosity
η_p	Solid fraction
κ	Thermal conductivity of air
κ_i	Initial contraction rate
Λ'	Thermal characteristic length
Λ	Viscous characteristic length
λ	Wave length
ν	Air kinematic viscosity
ξ	Normalized vector-valued parameter
ρ_0	Air density
$\rho(\omega)$	Dynamic density
σ	Static flow resistivity
σ_w	Structural coefficient
ϕ	Porosity
ω	Angular frequency
ϖ	Dimensionless viscous angular frequency
ϖ'	Dimensionless thermal angular frequency

Chapter I

General introduction

I.1 Introduction

“No one on our planet can escape the unwanted sound that we call noise – a disturbance to our environment escalating so rapidly as to become one of the major threats to the quality of our lives” (Chapter 1, *The impact of noise pollution: A socio-technological introduction*^[1]). Noise is defined as unwanted or harmful outdoor sounds caused mainly by mechanical machines, industrial and daily activities^[2,3] that affect both health and human behavior^[3,4]. Additionally, technological and industrial development brings about noise pollution, which currently entails growing environmental problems. Both the social direct and indirect impacts could be of major economic importance today. Overall, the costs arising from harm caused by noise are enormous, estimated to be around 13 billion € per year in the EU^[5].

It is well known that the knowledge that is being developed by scientists in the fields of acoustics could contribute to the redesigning of noisy machinery and processes, or/and the elaboration of the recommendations and solutions in the field of noise abatement. It is particularly highlighted in the continuous growth of patents and research work published in a number of peer-reviewed journals in this area.

To deal with the problems of noise, sound absorbing materials are one of the potentially major original remedies. Academics and scientists are progressively interested in finding an answer to the question of how materials are to the best of their sound absorption ability. Basically, a sound absorbing material, having a porous structure, is composed of a matrix based on solid skeleton^[6] and a pore space (e.g., cavities, channels or interstices^[7]) so that sound waves are able to propagate through them. Due to the combination of dissipation mechanisms when the air propagates within a porous medium, its freely propagating sound energy is absorbed^[8]. The acoustic performance of absorbing materials is governed by the mechanisms of acoustic energy dissipation during wave propagation in these media. The acoustic dissipation can be decomposed into two predominant mechanisms^[9]: dissipation by

visco-inertial effects and dissipation by thermal conduction.

In acoustics, different approaches have been developed to predict a link between microstructure properties and macroscopic acoustical performance of porous media^[10]. They can be categorized into three main types: (i) theoretical method^[11–16], which focuses on finding a theoretical understanding, leading to better understand the mathematical and physical bases of the macroscopic equations governing acoustic dissipation phenomena; (ii) experimental method^[17,18], which involves conducting a lot of laboratory measurements on samples of varying microstructural parameters; (iii) numerical method^[19–25], whereby the studies are mainly based on simulations centered on a combination of a numerical framework with an advanced computing method. Besides, recent studies include hybrid approaches combining numerical or/and analytical estimations of key physical parameters used as input data in empirical/semi-phenomenological models^[26–28].

Considering microstructural configurations, porous absorbing materials can be classified into three main types^[29]: cellular foam [Figures I.1(a) and I.7(a)], fibrous material [Figures I.1(b) and I.7(b)], and granular media [Figure I.1(c)], (also see legends within detailed images in Figure I.3). In some specific industrial applications, thin panels made of functional foams [i.e., epoxy foam, Figure I.1(d)] or microperforated structures [Figure I.1(e)] are also considered for their potential acoustic absorption.

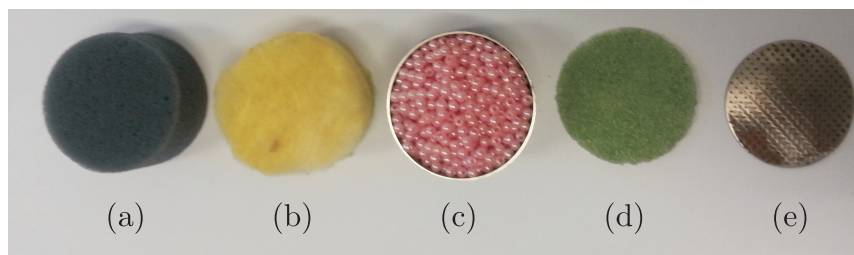


Figure I.1: (Color online) Different acoustical material samples: polymer foam (a), fibrous material (b), granular layer (c), epoxy foam panel (d), and microperforated panel (MPP) (e).

For acoustical materials, a common property of interest is their sound absorption coefficient (SAC). This parameter is used to refer to the proportion of the sound energy that an acoustical layer is able to absorb. The absorption coefficient is related to the reflection coefficient at the surface of a layer, in which the reflection factor is the ratio of the pressures created by the outgoing and the ingoing waves at the surface of the layer^[9] (see Figure I.2). One may observe that the absorption coefficient varies from 0 (total reflection) to 1 (total absorption). In the literature, based on considering the angular θ of the outgoing waves, two versions of the sound absorption coefficient are presented^[29]: the SAC at normal incidence with $\theta = 0^\circ$, and the SAC at oblique incidence with θ ranging from θ_{\min} to θ_{\max} (see e.g., $[0^\circ, 90^\circ]$ ^[30]).

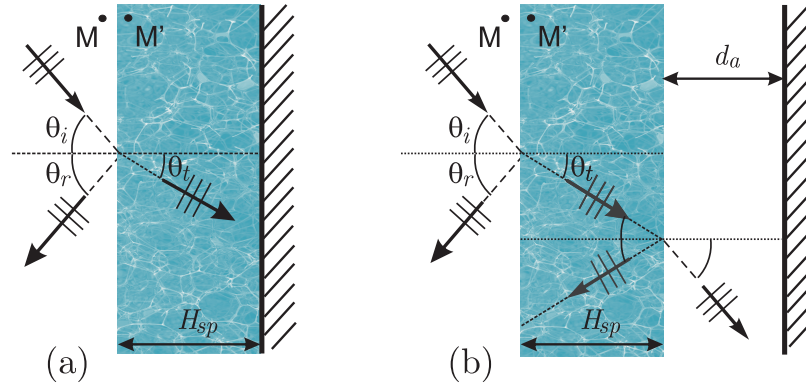


Figure I.2: (Color online) The ingoing and the outgoing plane waves at a plane interface between air and a porous material: the material is fixed to an impervious rigid wall (a), and there is a gap of air of thickness d_a between the material and the rigid wall (b). M , M' and M_1 indicate the locations measured the pressures related to estimations of SAC.

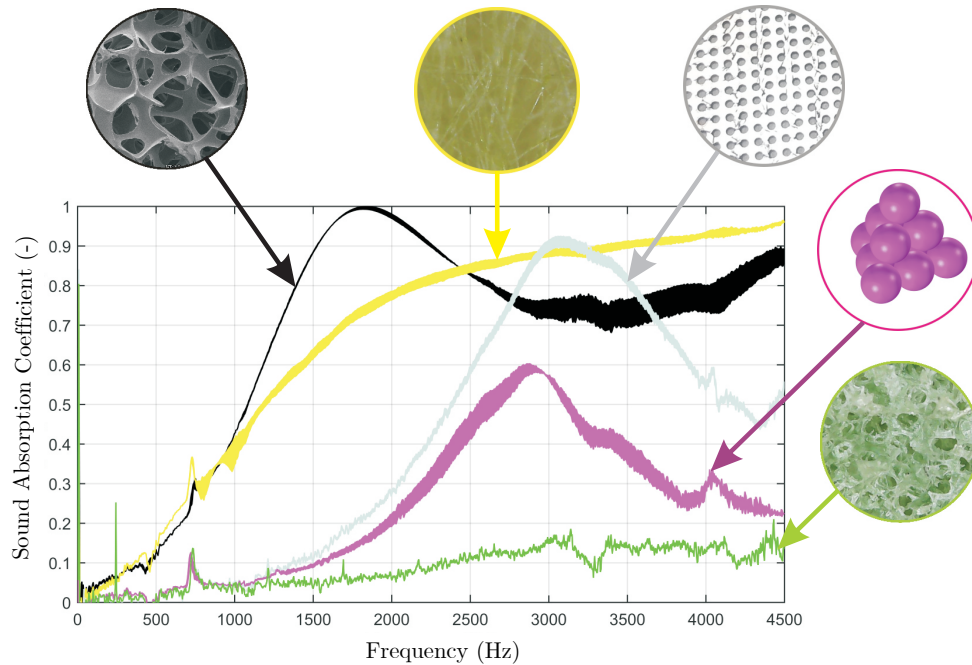


Figure I.3: (Color online) Measured sound absorption coefficients at normal incidence of various acoustic material samples shown in Figure I.1. The results are shown for: polymer foam (black), fibrous (yellow), MPP (gray), granular sample (magenta), and epoxy panel (green), and the corresponding thicknesses of [20, 20, 1, 20 and 3] mm, respectively. Noted that all measurements were performed by using a three-microphone standing impedance tube shown in Figure I.11(a). Here, there is only a cavity depth d_a of 7 mm used in the case of MPP panel.

For illustration purposes about the materials as well as the functional properties of acoustic absorption, Figure I.3 presents the corresponding sound absorption coefficient at normal incidence of the material samples provided in Figure I.1. The frequency range of interest is from 4 to 4500 Hz. It may be seen that, for a layer with the same thickness of 20 mm, the typical absorbers (e.g., cellular foam, fibrous and granular materials) show differently their interesting acoustic absorbing performances. Note that the polymer foam, MPP and granular sample absorption spectra show quarter compressional wavelength resonances. Because of the rigid backing, the particle velocity at the wall is zero (node). Therefore, the maximum velocity (in absolute value) of the air occurs at the interface between the air and the porous media (M and M') in the impedance tube (antinode). At the air/porous medium interface, because the particle velocity oscillations correspond to an extremum, the losses due to viscous effects are maximized. Such a phenomenon corresponds to a peak in the sound absorption spectra, whose position therefore depends at a given sample thickness only on the sound speed (complex valued) within the materia. In order to understand how effectively these materials work in their acoustical properties, we need to investigate the microstructure influence on the macroscopic acoustical properties of absorbing-based materials. Consequently, the present work focusing on acoustical foams is mainly concerned with this main aim.

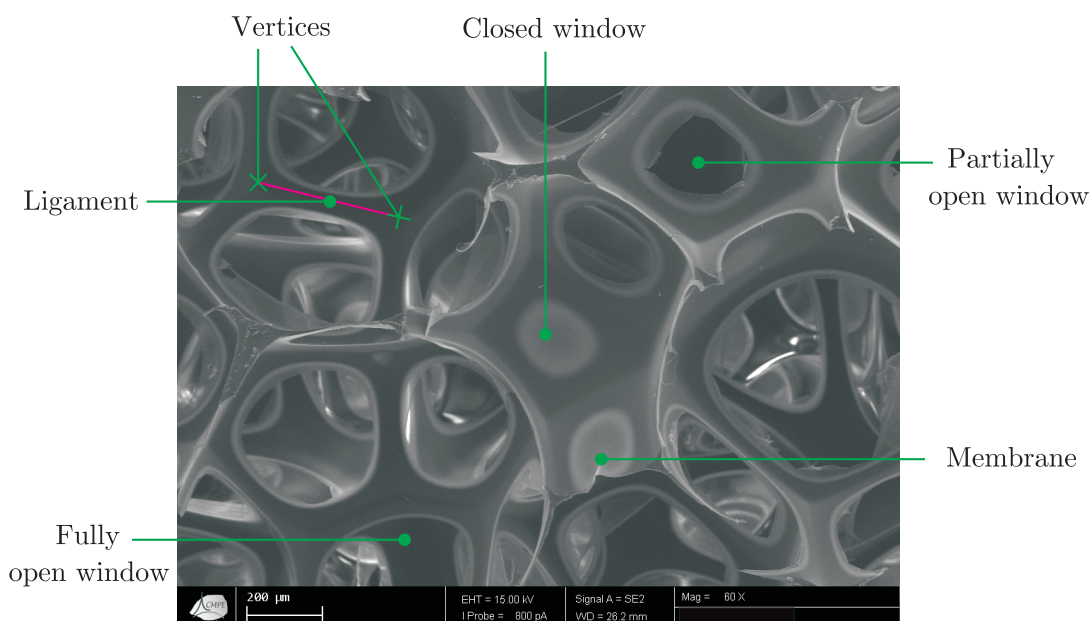


Figure I.4: (Color online) Morphology of membrane foam structure.

In the following of the manuscript, we are interested in studying the sound absorption properties of cellular foam. Foam is dispersion of gas in liquid or solid matrix. Its structure is made of membranes (also called films or liquid foams), ligaments or Plateau's borders,

(junction of three membranes) and vertices or nodes (junction of four ligaments), see Figure I.4. Whereas closed membranes are necessary to ensure the mechanical stability of liquid foam^[31], membranes can be open or totally absent in solid foams, allowing for the foam cells (pores) to be connected through windows.

Acoustical foams have been more interested in applications as advanced materials because they are less energy-consuming during their production, energy-saving during their use, and more efficient in the recycling process. However, lack of knowledge about relationships between micro-geometry and functional macroscopic properties of cellular foams is a recent scientific and technical barrier.

I.2 Study objectives and thesis organization

I.2.1 Study objectives

The general objective of this thesis is to model the acoustic behavior of a foam-based material through the multiscale modeling approach in order to investigate the dependence of transports and acoustical properties of elaborated materials on their geometric parameters. To achieve this goal, the following steps are necessary:

- ◇ Modeling microstructural foam structure and computing macroscopic properties.
 - Reconstruction of the representative elementary volume (REV) of both ordered and disordered cellular foam structures.
 - Computations of effective parameters of foam materials based on both direct and hybrid approaches.
- ◇ Construction of multiscale surrogates for optimization of acoustical materials.
 - Performing multiscale computations for reference macroscopic responses as a function of microstructural properties.
 - Building a surrogate model in order to speed up the optimization with respect to macroscopic properties based on polynomial chaos expansion technique.
- ◇ Experimental characterization of elaborated material samples.
 - Morphological characterization of several foam samples elaborated with the same density and the same monodisperse pore size but different values of the closure rate of the windows separating the foam pores.
 - Performing a set of experimental measurements to determine the air flow resistivity and acoustical properties of foam samples.

- ◇ Characterization of a link between microstructure and macro-scale behavior.
 - Application of equivalent configuration frameworks to numerical estimations of non-acoustical and acoustical properties of studied materials, these results are then compared to experimentally measured values.
 - Investigation of effects of membrane levels on the macroscopic properties.
- ◇ Numerical and semi-analytical predicting permeability of membrane foams.
 - Permeability estimations of partly open-cell foams.
 - Use of pore-network simulation and self-consistent model to investigate global permeability of membrane foams.

Note that this thesis is a part of an academic collaboration between four institutions:

- Multiscale Modeling and Simulation Laboratory (UMR 8208 CNRS), Paris-Est Marne-La-Vallée University, France.
- Geomaterials and Environment Laboratory (EA 4508), Paris-Est Marne-La-Vallée University, France.
- Navier Laboratory (UMR 8205-CNRS), IFSTTAR Institute, France.
- Department of Civil and Environmental Engineering, Duke University, Durham, NC 27708, USA.

The work of the doctoral student is supported by a fellowship awarded by the Government of Vietnam (Project 911). This work was part of a project supported by the French National Research Agency under Grants No. ANR-13-RMNP-0003-01 and No. ANR-13-RMNP-0003-03.

I.2.2 Thesis organization

The dissertation proceeds in the following way.

To begin with, we present a brief introduction about the sound absorbing materials and their acoustic absorption property. In the second section, a literature review on some existing empirical/semi-phenomenological models of acoustic materials and surrogate-based technique is introduced. We describe also some imaging techniques to clarify morphology of porous materials, and elaborated methods widely used to measure some macroscopic qualities (e.g., transports). In the third section, we provide a brief description of the numerical approach for modeling cellular material, which is later used as our numerical tool to carry out this project. We first describe a configuration of the representative element volume based on the

space-filling pattern of equal volume cells. Both existing numerical methods in the acoustic characterization of the porous material as an equivalent fluid are then introduced.

The main contributions of this thesis are structured around three papers presented as three following chapters. Chapter II deals with the optimizing problems of acoustic materials. The main difficulty in that context is the need to construct a direct map from the key microstructural features to the macroscopic response of homogenized acoustical properties. We investigate the potential of surrogate models (polynomial chaos expansions) to accurately approximate this mapping. The present approach uses Legendre orthogonal polynomials and enables appropriate convergence over the parameter space to be ensured. Chapter III is devoted to simulating the acoustic macro-behavior of partially closed-cell polymeric foams, typically their absorption coefficient by using numerical homogenization techniques at microstructure scale. This link is realized through the scaling of an idealized 3D PUC, which represents statistically the pore shape as a regular array of polyhedrons including membranes interconnecting the pores in the actual foam morphology. Multiscale computations are carried out in order to determine the intrinsic parameters of the foam samples, by solving asymptotically the viscous Navier-Stokes flow at low frequencies, the inertial Laplace potential flow at high frequencies, and the thermal conduction at low frequencies. In Chapter IV, we focus our interest on studying the permeability which is one of the most interesting physical parameters of cellular porous materials. We study the effects of membranes separating the foam pore connectivity on permeability. We begin with finite element model of partly open cell foams in order to find a local link between permeability and the membrane aperture size. With this local law, pore-network simulations and effective medium model are conducted to reproduce the finite element results and handle the permeability and percolation problem with foam structure on various lattices. The obtained results clarify the effect of the presence of membranes on foam permeability. In Chapter V, we further consider random foam structures. The local geometrical property of slightly and highly disordered foams is reconstructed as a representative element volume based on Voronoi patterns. A numerical example is provided in order to show the consistent results between the direct and hybrid numerical approach and confirm the advantages of the hybrid framework in terms of computational efficiency.

Finally, we present a general conclusion of the dissertation as well as include some directions for future work. Last but not least, Appendix A contains our preliminary results as a full paper in the sixth Biot Conference on Poromechanics, July 9–13th, 2017.

I.3 Literature review

In this section, a review of the literature on models of acoustical properties of acoustic absorbing materials and on characterizations of porous media is provided. In the first part, we present a bibliographical revision about empirical and semi-phenomenological models of

acoustic absorbing materials. Concerning the surrogate-based frameworks, the second part includes a short introduction to some selected methods that have been regularly used to reconstruct multiscale surrogate responses based on a given sampling of reference functions. In the third part, we briefly describe the morphology characterization by several advanced image techniques, and the experimentally characterizing of material behavior as physical properties (e.g., transports) by using some direct and indirect approaches.

I.3.1 Models of acoustical porous materials

Phenomenological approaches aim at looking for acoustic models for complex geometries, starting from solutions associated with simpler geometries for which analytical solutions exist, by introducing one or more shape factors depending on the local geometry. Inspired by Kirchoff's theory^[32], one of the first phenomenological models is that of [Zwikker and Kosten \(1949\)](#)^[33] with the hypothesis that the porous material consists of a network of parallel circular cylindrical pores, treating viscous effects and thermal conductivity separately. Equivalent to the model of Zwikker and Kosten, [Biot \(1956a,1956b\)](#)^[34,35] developed a theory on the propagation of elastic waves in a saturated porous medium. The equivalent works of Zwikker and Kosten and Biot are basic phenomenological models. Subsequently, several other models have proposed to modify these basic theories in order to extend their fields of application^[13,36-39]. These phenomenological approaches serve an important foundation in terms of principle understanding. However, they are more or less inaccurate or limited according to the applied types of materials. Nowadays, the semi-phenomenological models, more precise and predictive, are the most used. Focusing on motionless assuming of skeleton materials, different levels of modeling the acoustics of porous media will be presented in the forthcoming parts. It should be remarked that since only sound absorption is considered in the Thesis, the elasticity of polymer foams is not very important. It is likely to be more important for transmission or when foams are used for vibration absorption.

I.3.1.1 Empirical model

Methodologically, empirical modeling is one of the most common ways used for finding a general behavior on the basis of observations and experiments. Originally [Delany-Bazley \(1970\)](#)^[40] proposed an empirical model to describe sound propagation in highly porous materials (e.g., a fibrous material with porosity close to 1). This empirical law has been widely used in acoustic material characterizations because of two features that the equations are simple, and only one resistivity parameter is needed. After numerous measurements for materials of varying resistivity and a specific frequency range, Delany and Bazley established the laws which estimate the characteristic impedance Z_c and the complex wave number k as

a function of material flow resistivity.

$$\begin{aligned} Z_c &= \rho_0 c_0 \left[(1 + C_{11} X^{-n_{11}}) - j C_{12} X^{-n_{12}} \right], \\ k &= \frac{\omega}{c_0} \left[(1 + C_{21} X^{-n_{21}}) - j C_{22} X^{-n_{22}} \right], \end{aligned} \quad (\text{I.1})$$

in which ρ_0 is the air density, c_0 is the sound speed in air, $X = \rho_0 f / \sigma$ with f and ω the frequency and the angular frequency of the sound waves, σ is the airflow resistivity and j is the imaginary unit, $j = \sqrt{-1}$. The authors also mentioned a range of validity for their empirical law as $0.01 \leq X \leq 1$.

Table I.1: Coefficients in the Delany-Bazley, Miki, Mechel-Ver, and Allard-Champoux empirical models.

Coefficients	Delany-Bazley model ^[40]	Miki model ^[41]	Mechel-Ver model ^[42]		Allard-Champoux model ^[43]
			$X \leq 0.025$	$X > 0.025$	
C_{11}	0.0585	0.0700	0.0668	0.0235	0.0571
n_{11}	0.750	0.632	0.707	0.887	0.754
C_{12}	0.0878	0.1070	0.196	0.0875	0.0870
n_{12}	0.730	0.632	0.549	0.770	0.732
C_{21}	0.0975	0.1090	0.1350	0.1020	0.0978
n_{21}	0.700	0.618	0.646	0.705	0.700
C_{22}	0.1948	0.1600	0.3960	0.1790	0.1890
n_{22}	0.590	0.618	0.458	0.674	0.595

The Miki^[41] and Mechel-Ver^[42] models are also well-known empirical laws with conventional predictions of acoustic property. In the Miki study, the Delany-Bazley model was modified to obtain a real positive value at a wider frequency range and generalized with the models with respect to porosity, tortuosity and the pore shape factor ratio. The equations of Delany-Bazley were also corrected by Mechel and Ver as functions of a dimensional parameter, density by the quotient, between frequency and resistivity. Three models have the same formula structure as presented in Eq. (I.1), but the different values of coefficients are listed in Table I.1. Following the Delany and Bazley model, a number of empirical models were proposed for either some specific frequency ranges and/or different types of materials^[17,18,44–46]

Allard and Champoux (1992)^[43] developed an empirical model in which the dynamic density and the dynamic compressibility are defined with an additional validation at low frequencies where the equations of Delany and Bazley provide unphysical predictions (i.e., the negative real parts of the surface impedance and of the complex density, see Ref.^[47]). In the Allard and Champoux empirical model, two dynamic parameters are given as follows,

$$\begin{aligned} \rho(\omega) &= \rho_0 \left(1 + \frac{1}{j2\pi} \frac{1}{X} G_1(X) \right), \\ K(\omega) &= \gamma P_0 \left(\gamma - \frac{\gamma - 1}{1 + \left(\frac{1}{j} \frac{1}{8\pi N_{pr}} \right) X^{-1} G_2(X)} \right)^{-1}, \end{aligned} \quad (\text{I.2})$$

where $G_1(X)$ and $G_2(X)$ are the functions of X as $G_1(X) = \sqrt{1 + j\pi X}$ and $G_2(X) = 4\pi N_{pr} G_1$ with X as indicated in Eq. (I.1), N_{pr} is the Prandtl number, γ is the specific heat ratio of air and P_0 is the air equilibrium pressure.

It may be noted that, for air at normal temperature and atmospheric pressure $\rho_0 = 1.2$ kg/m³, $N_{pr} = 0.702$, $\gamma = 1.4$, $P_0 = 101\,320$ N/m², and using $k = \omega \sqrt{\rho(\omega)/K(\omega)}$ and $Z_c = \sqrt{\rho(\omega)K(\omega)}$, the Allard-Champoux model has also the two quantities are calculated with the same expressions of Delany and Bazley as Eq. (I.1), but the coefficients are different as listed in Table I.1.

Several other empirical models suggesting a relationship between acoustic parameters and structural characteristics can be found in several works of fibrous materials^[48–50]. In series of works related to cellular acoustic foams with and without membranes^[27], Doutres and co-workers proposed a combining method based on several empirical laws (estimated both analytically and experimentally) of non-acoustic parameters as a function of local geometrical features (e.g., porosity, cell size, reticulated rate of membranes). Under these observed laws, the authors used semi-phenomenological acoustic models (see Subsection I.3.1.2) to successfully characterize the acoustical properties of the foamy porous material.

It may be stated that, recently, these empirical models could be including limitations on the modeling of acoustic porous materials having advanced morphologies (e.g., complexity of membrane content^[46,51], polydispersity of fibers^[52]).

I.3.1.2 Semi-phenomenological model

In order to give a physical basis to the description of sound propagation in porous media, we proposed a brief description, in the frequency domain, selected semi-phenomenological models involving several physical parameters. The air in the porous frame is replaced by an equivalent fluid that presents the same bulk modulus $K(\omega)$ as the saturating air and a dynamic density $\rho(\omega)$ that takes into account the viscous and the inertial interaction with the frame. Using this pair of dynamic parameters, the wave number k and the characteristic impedance Z_c may be estimated to describe the acoustical properties of a medium^[9].

Johnson et al. (1987)^[12] presented a semi-phenomenological model with four macroscopic parameters (the resistivity σ , the open porosity ϕ , the high frequency tortuosity α_∞ , the viscous characteristic length Λ). Johnson et al. developed a formula to describe the complex density. They studied the viscous dissipation effects of a Newtonian fluid saturating

a rigid and isotropic porous medium subjected to a pressure gradient oscillating through the sample. They further assumed that the wavelength is much greater than the pore size and that the thermal conductivity of the fluid is negligible. Later, this model was modified and improved by other authors to introduce new parameters related to the finer account of physics.

Based on the Johnson et al. work, [Champoux and Allard \(1991\)](#)^[13] introduced an expression for the dynamic bulk modulus involving the effects of heat dissipation. To take these effects into account, Champoux and Allard proposed a new model by adding a parameter characterizing the high frequency asymptotic behavior of the thermal response named the thermal characteristic length Λ' . The approach followed by Champoux and Allard is similar to that of Johnson and co-workers^[13] in treating viscous effects. The thermal characteristic length is an intrinsic parameter of the material which is purely geometrical, it coincides with the viscous length in the case of a material composed of uniform and non-intersected pores. From this, the visco-inertial dissipative and thermal effects match the dynamic density and the dynamic bulk modulus, respectively, as given by

$$\rho(\omega) = \rho_0 \alpha_\infty \left[1 + \frac{\sigma \phi}{j \omega \rho_0 \alpha_\infty} \sqrt{1 + j \frac{4 \alpha_\infty^2 \eta \rho_0 \omega}{\sigma^2 \Lambda^2 \phi^2}} \right], \quad (\text{I.3a})$$

and

$$K(\omega) = \gamma P_0 \left[\gamma - (\gamma - 1) \left(1 - j \frac{8 \kappa}{\Lambda'^2 C_p \rho_0 \omega} \sqrt{1 + j \frac{\Lambda'^2 C_p \rho_0 \omega}{16 \kappa}} \right) \right]^{-1}. \quad (\text{I.3b})$$

[Lafarge \(1993,1997\)](#)^[15,53] modified the Champoux and Allard model (1991) concerning heat dissipation by introducing a new parameter, the static thermal permeability k'_0 . This factor is used to characterize thermal dissipation phenomena at low frequencies. This leads to a modified expression of the dynamic bulk modulus as compared with the original work by [Champoux and Allard \(1991\)](#), it is given as

$$K(\omega) = \gamma P_0 \left[\gamma - (\gamma - 1) \left(1 - j \frac{8 \phi \kappa}{k'_0 C_p \rho_0 \omega} \sqrt{1 + j \frac{4 k'_0{}^2 C_p \rho_0 \omega}{\kappa \Lambda'^2 \phi}} \right) \right]^{-1}. \quad (\text{I.4})$$

[Pride et al. \(1993\)](#)^[16] found that the imaginary part of the dynamic tortuosity (or dynamic viscous permeability) in the Johnson et al. model^[12] is underestimated in the case of a fluid subjected to strong variations of sections along the acoustic wave path. Therefore a new macroscopic parameter, the low-frequency viscous tortuosity, was proposed to improve the low-frequency asymptotic behavior of viscous dissipations. Similarly, [Lafarge \(1997\)](#)^[15] refined their model by correcting the low frequency behavior of heat dissipation by adding the low frequency thermal tortuosity. As a result, the enhanced version of two dynamic

parameters is given in the forms,

$$\rho(\omega) = \rho_0 \alpha_\infty \left[1 + \frac{\sigma \phi}{j \omega \rho \alpha_\infty} \left(1 - P + P \sqrt{1 + j \frac{M}{2P^2} \frac{\alpha_\infty \rho_0 \omega}{\sigma \phi}} \right) \right], \quad (\text{I.5a})$$

and

$$K(\omega) = \gamma P_0 \left[\gamma - (\gamma - 1) \left(1 - j \frac{8 \kappa \phi}{k'_0 C_p \rho_0 \omega} \left(1 - P' + P' \sqrt{1 + j \frac{M'}{2P'^2} \frac{k'_0 C_p \rho_0 \omega}{\kappa \phi}} \right) \right) \right]^{-1}, \quad (\text{I.5b})$$

where four non-dimensional shape factors are defined as a function of material parameters,

$$M = \frac{8 \eta \alpha_\infty}{\sigma \Lambda^2 \phi}, \quad M' = \frac{8 k'_0}{\Lambda'^2 \phi}, \quad P = \frac{M}{4(\alpha_0/\alpha_\infty - 1)}, \quad P' = \frac{M'}{4(\alpha'_0 - 1)}. \quad (\text{I.6})$$

In summary, the three semi-phenomenological models previously described may be used to estimate the frequency dependent visco-inertial and thermal responses of porous media. The Johnson-Champoux-Allard (JCA) model involves 5 parameters (ϕ , σ , α_∞ , Λ , and Λ'), the Johnson-Champoux-Allard-Lafarge (JCAL) model is adding parameter k'_0 , and the Johnson-Champoux-Allard-Pride-Lafarge (JCAPL) model uses a set of 8 parameters (ϕ , σ , α_∞ , Λ , Λ' , k'_0 , α_0 and α'_0).

Recently, these semi-phenomenological models are being widely used to characterize various acoustical materials. Their input parameters can be estimated experimentally as mentioned previously. Alternatively, they can be computed by solving numerically several governing equations over a representative element volume of porous media (see Section I.4).

I.3.2 Surrogate-based modeling methodology

Theoretical modeling and computational simulations are key ingredients to understand a complex system, entity, phenomenon or process. An increase in model runtime generally requires degrading the fidelity of the model, either in the numerical solver (using, e.g., a coarser discretization) or by introducing a low-fidelity approximation of the physical model. In this context, surrogate models are computationally tractable, cheaper models designed to approximate (in some sense) the dominant features of a complex model. These models are also known as metamodels^[54], reduced models^[55], response surfaces^[56], model emulators^[57], proxy models^[58], and lower fidelity models^[59]. Metamodels can be used, for instance, to approximate cost or state functions in optimization loops. More specifically, consider a computational model associated with a given system, and denote by \mathbf{m} the vector of input parameters. Assume that \mathbf{m} belongs to some admissible closed set $\mathcal{S}_m = \times_{i=1}^n [a_i, b_i]$ in \mathbb{R}^n , and let $\mathbf{q} \in \mathcal{S}_q \subseteq \mathbb{R}^d$ be a d -dimensional quantity of interest. Assume now that one is interested in optimizing a given functional $\mathbf{m} \mapsto J(\mathbf{q}(\mathbf{m}))$, the evaluation of which is computationally expensive. In order to simplify exposure at this stage, assume that $J(\mathbf{q}(\mathbf{m})) = \mathbf{q}(\mathbf{m})$. A

classical remedy to circumvent the computational burden then consists in constructing a surrogate mapping $\hat{\mathbf{q}}$ that properly approximates \mathbf{q} (that is, the map $\mathbf{m} \mapsto \hat{\mathbf{q}}(\mathbf{m})$ approaches the solution map $\mathbf{m} \mapsto \mathbf{q}(\mathbf{m})$ in some sense). Several approaches were proposed in the last two decades to construct surrogates. Among them, we may list here the radial basis functions^[60], the weighted trigonometric approximation^[61], high-dimensional model representation^[62,63], Kriging models^[64], moving least square approximation method^[65], methods of separated variables representations^[66], or artificial neural networks^[67]. For smooth reference maps, polynomial series are natural candidates^[68–70] and will be considered thereafter.

Let us illustrate this approach on a basic example. Upon introducing the normalized vector-valued parameter $\boldsymbol{\xi}$ such that $[-1, 1] \ni \xi_i := 2/(b_i - a_i)m_i + (a_i + b_i)/(a_i - b_i)$ for $1 \leq i \leq n$, the surrogate model $\hat{\mathbf{q}}$ is then sought for as a polynomial map in $\boldsymbol{\xi}$:

$$\hat{\mathbf{q}}(\boldsymbol{\xi}) = \sum_{\boldsymbol{\alpha}} \hat{\mathbf{q}}_{\boldsymbol{\alpha}} P_{\boldsymbol{\alpha}}(\boldsymbol{\xi}), \quad (\text{I.7})$$

where $\boldsymbol{\alpha}$ is a multi-index in \mathbb{N}^n , $P_{\boldsymbol{\alpha}}$ is the multidimensional Legendre polynomial defined as $P_{\boldsymbol{\alpha}}(\boldsymbol{\xi}) = \prod_{i=1}^n P_{\alpha_i}(\xi_i)$, and P_{α_i} is the univariate Legendre polynomial of order α_i . The Legendre polynomials $\{P_{\alpha}(\xi)\}_{\alpha \geq 1}$ satisfy the following recurrence relation^[71]:

$$P_{\alpha+1}(\xi) = \frac{2\alpha+1}{\alpha+1} \xi P_{\alpha}(\xi) - \frac{\alpha}{\alpha+1} P_{\alpha-1}(\xi), \quad (\text{I.8})$$

in which $P_0(\xi) = 1$ and $P_1(\xi) = \xi$ for all $\xi \in [-1, 1]$. From the orthogonality of these basic polynomials, namely

$$\langle P_{\boldsymbol{\alpha}}, P_{\boldsymbol{\beta}} \rangle := \frac{1}{2^n} \int_{([-1,1])^n} P_{\boldsymbol{\alpha}}(\mathbf{x}) P_{\boldsymbol{\beta}}(\mathbf{x}) d\mathbf{x} = \prod_{i=1}^n \frac{\delta_{\alpha_i \beta_i}}{2\alpha_i + 1}, \quad (\text{I.9})$$

where δ is the Kronecker delta, it follows that

$$\hat{\mathbf{q}}_{\boldsymbol{\alpha}} = \left(\prod_{i=1}^n (2\alpha_i + 1) \right) \langle \hat{\mathbf{q}}, P_{\boldsymbol{\alpha}} \rangle. \quad (\text{I.10})$$

The choice of this polynomial basis ensures that the surrogate is uniformly accurate over the parameter space, so that no bias (noise) is generated in the evaluation of the cost function. The computation of the coefficients $\hat{\mathbf{q}}_{\boldsymbol{\alpha}}$ requires the evaluation of n -dimensional integrals, and various techniques have been proposed in the literature to address this issue. Standard or enhanced (i.e., nested, sparse, etc.) quadrature rules may be invoked for small values of n , while (advanced) Monte Carlo simulation techniques may be used for much higher dimensions (see, e.g., Ref.^[72]). Below, a Gauss-Legendre quadrature rule (with N_Q points) is used for illustration purposes.

It follows from Eq. (I.7) that the approximant, truncated at order p , is given by

$$\hat{\mathbf{q}}_p(\boldsymbol{\xi}) := \sum_{\boldsymbol{\alpha} \in \mathbb{N}^n, |\boldsymbol{\alpha}|=0}^p \hat{\mathbf{q}}_{\boldsymbol{\alpha}} P_{\boldsymbol{\alpha}}(\boldsymbol{\xi}) = \sum_{\boldsymbol{\alpha} \in \mathbb{N}^n, |\boldsymbol{\alpha}|=0}^p \hat{\mathbf{q}}_{\boldsymbol{\alpha}} P_{\alpha_1}(\xi_1) P_{\alpha_2}(\xi_2) \dots P_{\alpha_n}(\xi_n), \quad (\text{I.11})$$

where $\boldsymbol{\xi} = (\xi_1, \xi_2, \dots, \xi_n)$ and $|\boldsymbol{\alpha}| := \sum_{i=1}^n \alpha_i$. The coefficients are then estimated [see Eq. (I.10)] as

$$\hat{\mathbf{q}}_{\boldsymbol{\alpha}} \approx \prod_{i=1}^n \frac{2\alpha_i + 1}{2^n} \sum_{i=1}^{N_{\mathcal{Q}}} w_i \hat{\mathbf{q}}(\boldsymbol{\xi}^{(i)}) P_{\boldsymbol{\alpha}}(\boldsymbol{\xi}^{(i)}) , \quad (\text{I.12})$$

in which $\{w_i\}_{i=1}^{N_{\mathcal{Q}}}$ and $\{\boldsymbol{\xi}^{(i)}\}_{i=1}^{N_{\mathcal{Q}}}$ are the weights and points of the quadrature rule. In practice, the evaluation of the multiscale model at the quadrature points is obtained by mapping back the reduced variables onto the physical ones, and convergence must be characterized with respect to both p (which controls the global order of the polynomial series) and $n_{\mathcal{Q}} = (N_{\mathcal{Q}})^{1/2}$ (which controls the convergence of the quadrature rule, for a fixed order of expansion p). Note that the convergence analyses with respect to the parameters of the formulation, namely the order p of the expansion and the total number $n_{\mathcal{Q}}$ of quadrature points, must be carried out.

For demonstration purposes, consider the following two-dimensional example in which the target function is defined as a combination of Legendre polynomials:

$$\mathbf{q}(\xi_1, \xi_2) = P_6(\xi_1)P_9(\xi_2) + 3P_{10}(\xi_1)P_5(\xi_2), \quad (\text{I.13})$$

The results shown in Fig. I.5 confirm that the reference response can properly be reproduced with an error close to 10^{-14} , using a sampling of $12^2 = 144$ evaluations of the reference map.

I.3.3 Characterization of porous media

I.3.3.1 Morphology characterization

In material engineering and science, the interest in studying the morphological property has been arising among industrial and academic communities over the past century. The study of local geometry material plays a very important role in the science of materials mainly because the macroscopic material properties are highly dependent on the local microstructural features. Knowledge of the material microstructures allows to interpret and explain their physically functional properties. In this respect, a comprehensive study of morphology can provide essential information for the advanced numerical simulations at some scales to determine and predict their macroscopic characteristics. Based on this micro-macro link, it is convenient to define a geometrical configuration for a specific target of the macroscopic parameter. Thanks to the recent advances in technology it became possible to switch to techniques that provide two-dimensional and three-dimensional images of material microstructures such as porous media for example. The microstructure is widely characterized at different scales by conventional two-dimensional imaging techniques: optical microscopy and electron microscopy, which have been completed recently by more advanced three-dimensional imaging techniques such as the different types of tomography and especially the X-ray microtomography. These methods can produce digital images which may be extracted from quantitative parameters

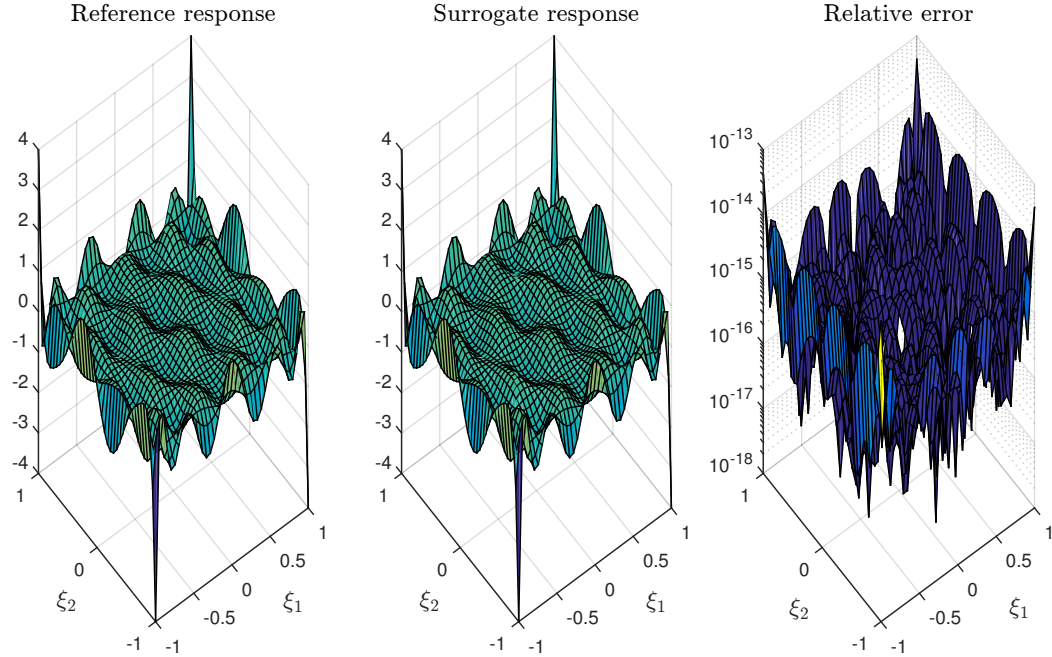


Figure I.5: The approximate solution map $(\xi_1, \xi_2) \mapsto \hat{q}_p(\xi_1, \xi_2)$ (middle) is compared with the reference solution map $(\xi_1, \xi_2) \mapsto \mathbf{q}(\xi_1, \xi_2)$ (left), these results are shown for $p = 15$ and $n_Q = 12$. The corresponding relative error is measured as $\mathcal{D}_p(\xi_1, \xi_2) = |\mathbf{q}(\xi_1, \xi_2) - \hat{q}_p(\xi_1, \xi_2)|/|\mathbf{q}(\xi_1, \xi_2)|$ (right).

of the microstructure. It should be noted that here we narrow the scope to the image techniques for man-made porous materials with *macropores* (with sizes > 50 nm). Although a large number of different types of microscopes have been developed and applied in different applications, the following briefly presents the image techniques that are commonly used for the characterization of porous materials.

Two-dimensional image techniques:

So far, many advanced scanning techniques were put into practice; however, 2D imaging techniques such as optical microscopy, scanning and transmission electron microscopy, and scanning probe microscopy are quite well developed [73]. In porous media imaging field, both optical and electron microscopy techniques are very useful in characterizing tools for a variety of scales [74] as well as materials [75–77]. Figure I.6 presents photos of (left) a S-3000N Hitachi Scanning Electronics Microscope (available at the Centre characterization of materials (CCM) at the Université de Sherbrooke, Canada), and (right) a LEICA MZ6 Binocular Microscope (available at the Navier Laboratory at the Paris-Est University, France). In general, two-dimensional images may be used for characterizing a number of microstructural features such as porosity, specific surface area, and pore and particle sizes of a porous medium. In

researches on geometry, transports, and acoustics of typical porous materials, 2D image techniques are widely used for various structures: liquid foams^[78], solid foams^[26,28,75,79], fibrous materials^[77,80], granular media^[76,81,82]. Figure I.7 shows two scanning electronic micrographs of common absorbing materials [i.e., foam structure (left image) and fibrous structure (right image)]. Based on the observed images, some microstructural qualities of these porous materials may be characterized (i.e., cell size, and anisotropy degree of foam structures^[79,83], fibrous angular orientation in fibrous materials^[77]).

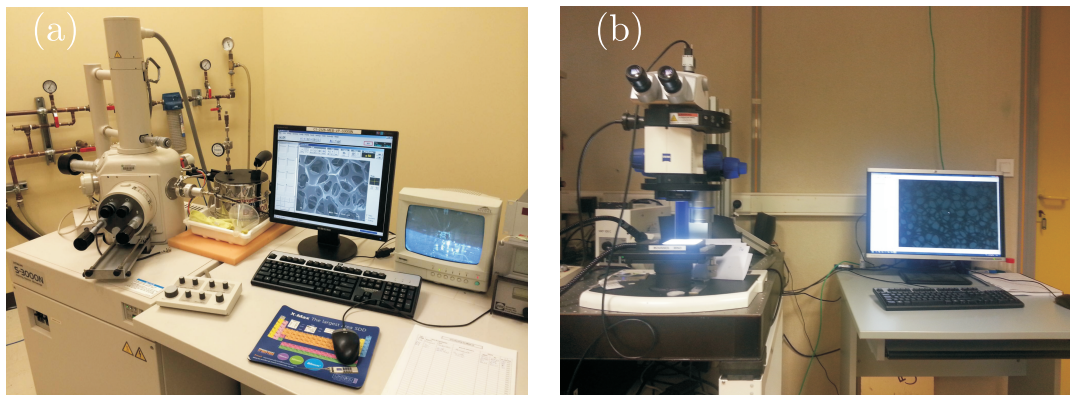


Figure I.6: Photos of a Hitachi S-3000N variable-pressure Scanning Electron Microscope (VP-SEM) (a) and a LEICA MZ6 Binocular Microscope (b).

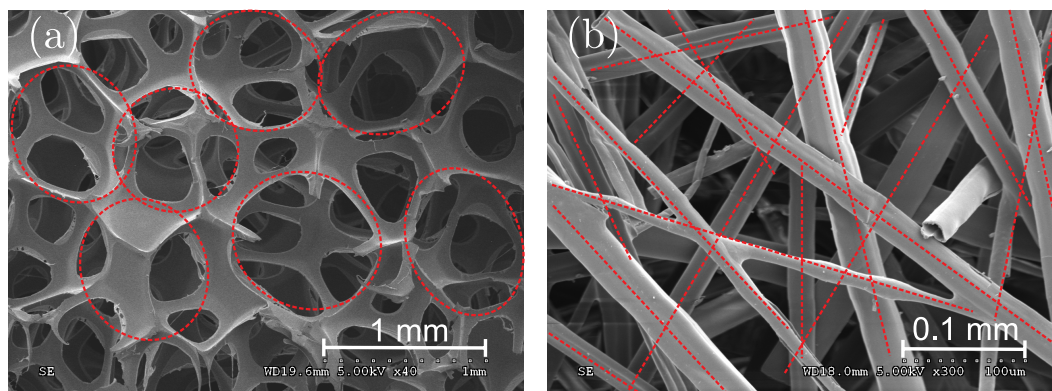


Figure I.7: Photographs of the local microstructures of a real cellular foam (a) and a fibrous material sample (b).

To demonstrate the characterizing process, we experimentally measure two morphological parameters from a set of fifteen foam images with a calibration as shown in Figure I.7(a). The observed ellipses surrounding cell vertices in the observation plane can provide information about the cell size and its anisotropy degree. Over these fitting ellipses, the distributions of anisotropy degree and normalized cell size are obtained. As illustrated in Figure

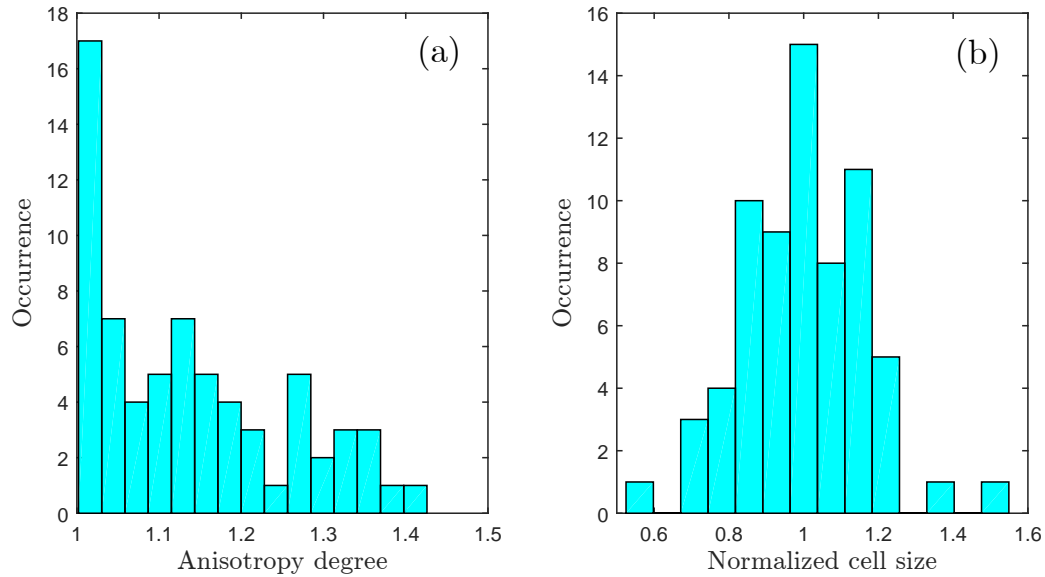


Figure I.8: Distributions of anisotropy degree (a) and normalized cell size (b) as experimentally determined by scanning electron microscopy.

I.8, the sample has a shape anisotropy degree with a Gama distribution having a mean value of roughly 1.15. In terms of polydisperse level, the normalized cell size result shows a good fitting to a normal distribution having a mean of 1 and a standard deviation of 0.16.

In comparison with recent advanced techniques, it is seen that the 2D image microscopic techniques have the advantages of being rapid and inexpensive and easy to implement. However, porous medium characterization working based on 2D images requires some post-processing steps in order to obtain essential information or representative models.

Three-dimensional image techniques:

Three-dimensional scanning is an advanced technique for capturing the 3D shape of an object and storing the data as a three-dimensional model (virtual model) in which, the scanned virtual 3D model is almost ready for further using purposes. In porous media characterization, three-dimensional microscopic reconstruction typically requires a stack of 2D data which is obtained by using X-ray microtomography such as tomography and X-ray computed tomography. A stochastically equivalent 3D reconstruction of porous media can be rebuilt from 2D image data by various techniques such as the Joshi-Quiblier-Adler approach^[84–87], the single cut-Gaussian Random field approach^[88], and the Karhunen-loeve expansion-based approach^[89].

A realistic structure representing a real medium with the detailed description can be



Figure I.9: 1172 X-ray Microtomograph Skyscan [94].

obtained by a scanner machine with a given resolution. This may be encountered when studying the representative elementary volume of a porous material is generally characterized by advanced imaging techniques [i.e., micro-computed tomography (μ CT)] associated with statistical tools originating from mathematical morphology^[90] used in order to generate a porous sample statistically identical to the real one such that the disordered nature of porous media is preserved^[91–93].

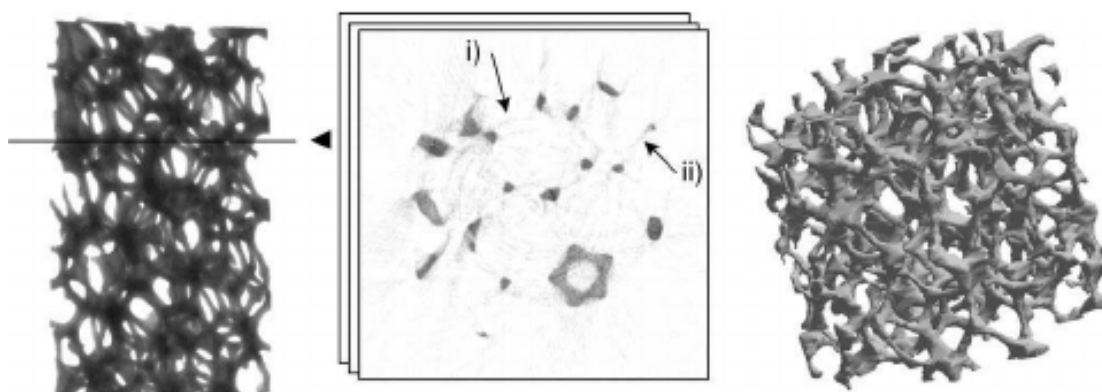


Figure I.10: Main steps of the reconstruction process by x-ray micro computed tomography^[25]: (left) Acquisition of classical radiographies, or “x-ray shadow images” of the real sample; (middle) Reconstruction of bidimensional cross sections of the real sample showing (i) “ring artifacts” and (ii) “starburst artifacts”; (right) Reconstruction of the three-dimensional image of an axial portion of the real sample, after binarisation of the two-dimensional images.

For foams without membranes, using X-ray microtomography allows reconstructing the microstructure of open-cell metal foams^[25,93]. Figure I.10 shows a typical reconstructing process by using 3D scanning technique with the SkyScan 1172 scanner (Figure I.9^[94]). For materials made of fibers, their representative 3D microstructure models can be achieved also by computed tomography using X-ray absorption contrast^[92,95]. Recently, micro-computed tomography was used as a tool to characterize granular materials with various shapes of a

particle such as spherical fillers, flake fillers, and rod fillers^[96]. It should be noted that the requirement of operating parameters of a 3D machine is dependent on the contrast between material phases (e.g., fluid and solid phases of the porous sample) and the ratio scale between their components. A partially open-cell foam has very thin membranes (e.g., film thickness, less than $1.5 \mu\text{m}$, is about $1/500$ times the cell scale of $810 \mu\text{m}$ ^[83]), or a hollow-fiber structure has a very small ratio between fibrous thickness and radius, such materials require either a scanner having a corresponding high resolution or a reduction of imaging sample size.

Obviously, 3D scanning techniques provide a number of advantages such as an accurate and detailed representation of the scanned volume, and require of little to no pre-processing. Once the scanning microstructures are available, they may be used for computing at a global scale for computing at global scale a number of macroscopic material properties such as permeability, capillary pressure, heat transfer coefficient, acoustic absorption, effective elastic parameter, etc. In addition, working on the 3D reconstructed volume allows varying systematically characteristics of the microstructure in order to simulate or predict the behavior of materials. However, because the structures are more realistic they may also be actually more difficult to parametrize so that it is hardly possible to study how the microstructural features are related to the macro-performances and to clearly identify the optimal configurations.

I.3.3.2 Physical property characterization

In acoustics, one of the available models applied to predict the macroscopic performance of porous materials was proposed originally by Biot (1956a, 1956b)^[34,35]. This consists of a set of five parameters known as the Biot parameters: the porosity, the airflow resistivity, the tortuosity, the thermal characteristic length, and the viscous characteristic length. Various methods have been developed to measure and estimate these parameters (see Refs.^[97–99] for a survey).

The porosity ϕ of a porous medium is a fraction of the continuous fluid volume (e.g., air) over the total volume. This parameter may be measured by several methods. A simple method is proposed by Beranek, (1942)^[100], in which the porous material is saturated with water and placed in an airtight chamber that is connected to a manometer. Another simple method is to directly measure the medium's total volume V_t , the porous material is then crushed to remove all the void space, and the volume V_s of the solid phase is measured. The porosity is then given by $\phi = 1 - V_s/V_t$. Alternatively, the solid volume can be measured through as $V_s = m_s/\rho_s$, in which m_s and ρ_s are the mass and the density of solid materials, respectively. Following the Beranek's principle, Champoux et al. (1991)^[101] developed a very elaborate device involving a micrometre and a differential pressure transducer. Salissou and Panneton, (2008)^[102] proposed a method using the perfect gas law where the open porosity is deduced from the measured sample mass at four static pressures. It can be also mentioned the ASTM D6226–05 standard test^[103] as an alternative method that can measure porosity

by using a gas pycnometer.

In porous materials, tortuosity α_∞ is an intrinsic characteristic which usually is defined as the ratio of the actual length of the pores to the body length of the material^[33]. This factor can be deduced experimentally through an electrical method based on the resistivity of the material upon saturation with a conducting fluid when the field of the current and the microscopic speed of the fluid are equivalent^[11,12]. A method using ultrasound wave, proposed by [Fellah et al. \(2003a, 2003b\)](#)^[104,105], can measure both ϕ and α_∞ . This ultrasound method, however, is only suitable for materials with rigid structures, so for a non-rigid frame in order to reduce the vibration of the frame skeleton a temperature controlled chamber (i.e., at -20°C ^[51]) or steel nails^[106,107] should be used. [Allard et al. \(1994\)](#)^[108] developed a method to determine tortuosity based on the determination of the high-frequency limit for the complex phase velocity.

The static airflow resistivity σ , an important physical property of porous materials, is defined as the pressure difference over flow velocity per unit length. For a certain microstructural material, this parameter may be measured by several approaches^[109]. The original works focusing on the determination and the measurements of resistance to air flow through to porous material were proposed by [Beranek \(1942\)](#)^[100], and [Brown and Bolt, \(1942\)](#)^[110]. Their method uses a vacuum to produce a pressure drop across a specimen of porous material for which there is no temporal variation under steady-state conditions. Two parameters, the pressure drop between two faces of the tested specimen and the volumetric airflow rate, are measured. More commonly, a measurement of flow resistivity may be found in the standard test method ASTM C-522, ISO 9053^[111], and [Stinson and Daigle \(1988\)](#)^[112]. A photo of a device for measurements of airflow resistivity is shown in the right part of [Figure I.11](#).

The characteristic lengths referring to the thermal Λ' and viscous Λ characteristic length of a porous material take the thermal and viscous dissipation into account, respectively. In porous media, the energy loss through heat occurs in the part where the cells are stretched, and the energy loss by viscosity occurs in the narrow part. These lengths are therefore related to the shape of the apertures inside the porous material. The length Λ' defined as twice the average volume-to-surface ratio of the pores, has been evaluated through a non-acoustic method from the measurement of the specific area using the standard Brunauer-Emmet-Teller (BET) technique which involves gas molecule measurements of the skeleton pores. Based on the BET technique, [Lemarinier et al. \(1995\)](#)^[113] and [Henry et al. \(1995\)](#)^[114] used krypton gas in order to increase the precision of the measurement. An ultrasonic attenuation can also be used to measure both characteristic lengths by the saturating fluid for the porous material^[115,116]. This method determines the viscous Λ and thermal Λ' characteristic lengths from the exploitation of the dispersion curves in air- and helium-filled materials. [Moussatov et al. \(2001\)](#)^[117] developed an ultrasonic method that considers the evolution of the speed of sound and the attenuation inside the material due to changing of the static pressure of the gas saturating the material. The method allows an estimation of three parameters of the

sample materials: the tortuosity, and the viscous and thermal characteristic lengths.

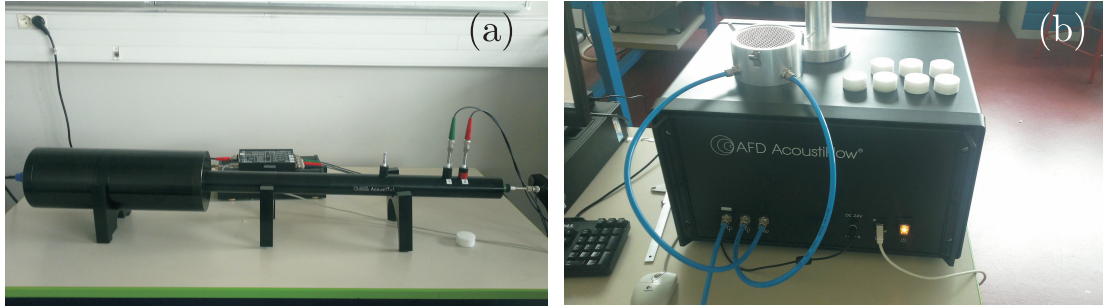


Figure I.11: Picture of a standing impedance tube which can be used to measure the acoustic absorption coefficient at normal incidence and characterize material parameters of a semi-phenomenological model (a), picture of a device for measuring of the static airflow resistivity of porous materials (b).

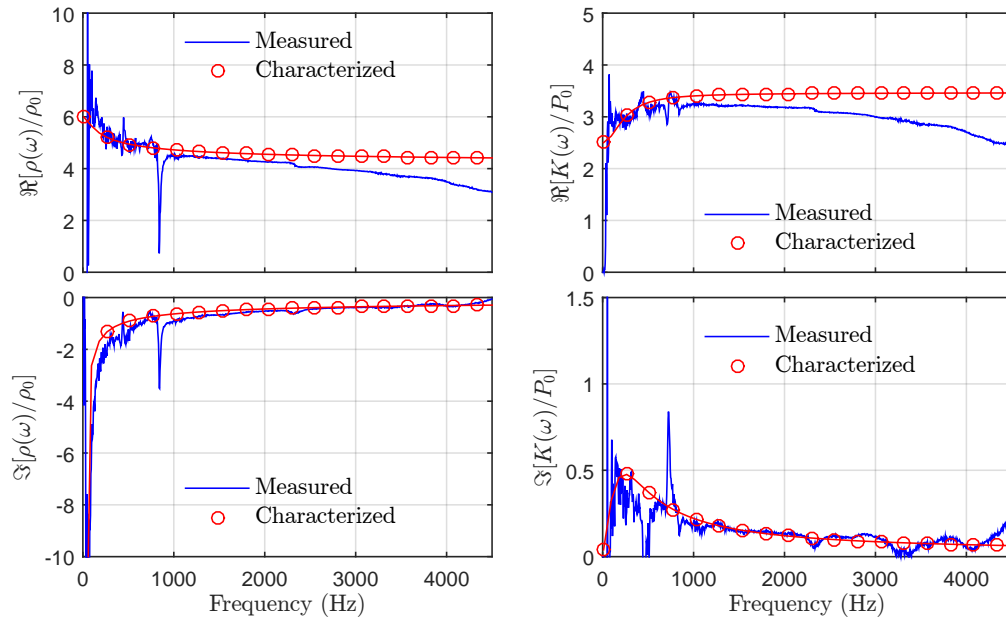


Figure I.12: Comparison between measured (line) and characterized (marker) results of normalized effective density (left part) and the normalized effective bulk modulus (right part). The results are obtained from a three-microphone standing tube measurement on the granular layer shown in Figure I.1(c).

Besides the laboratory approaches stated above, some alternative indirect methods are also widely used. Two geometry parameters (ϕ , Λ') can be defined by using image technique with the reconstruction of local geometrical features (e.g., an original and simple idea of image

processing with a hit list^[118]). Having the representative element volume reconstructed by 2D or 3D image techniques, these factors and other morphology properties may be estimated numerically with their mathematical definitions.

Alternatively, [Panneton and Oly](#)^[107,119,120] proposed an indirect characterization method for determining the intrinsic parameters of porous materials by means of a standing three-microphone tube test (see the left part of Figure I.11). The dynamic density $\rho(\omega)$ and bulk modulus $K(\omega)$ properties of tested materials are estimated according to experimental data with two measured pressure transfer functions. Based on the JCAL model, the static air flow resistivity, the high frequency tortuosity, and the viscous characteristic length are estimated from the measured data of the dynamic mass density, and the measured dynamic bulk modulus allows to deduce the thermal characteristic length and the thermal permeability. The following table give the example of a granular layer. Based on the data of the impedance tube experiment, Table I.2 presents the results of characterized transport properties.

Table I.2: The characterized parameters of the granular material sample.

Parameter	Λ' (μm)	Λ (μm)	σ (Nm^{-4}s)	k'_0 ($\times 10^{-10}\text{m}^2$)	α_∞ (-)
Value	1050 ± 74	545 ± 46	1500 ± 115	78 ± 10	1.65 ± 0.21

As may be seen in Figure I.12, the characterized effective properties of the equivalent fluid for the porous granular sample are in very good agreement with experimental data.

I.4 Numerical approach for modeling acoustical cellular materials

This section presents a basic approach applied to model numerically acoustical cellular materials. Firstly, the reconstruction task of local geometrical of foam-based materials having regular structures is carried out based on an ordered packing of space-filling cells. Using homogeneous techniques of representative elementary volumes, the transports and effective properties of an equivalent fluid of studied materials are then estimated using two existing numerical frameworks named as direct method and hybrid method.

I.4.1 Reconstruction of local ordered foam structures

In the 1960s, various simple idealized open and closed cell structures were used to model the physical behavior of cellular materials and to derive respective constitutive equations to predict their behavior: open cell of rubber foams^[121], open foamed elastic materials^[122],

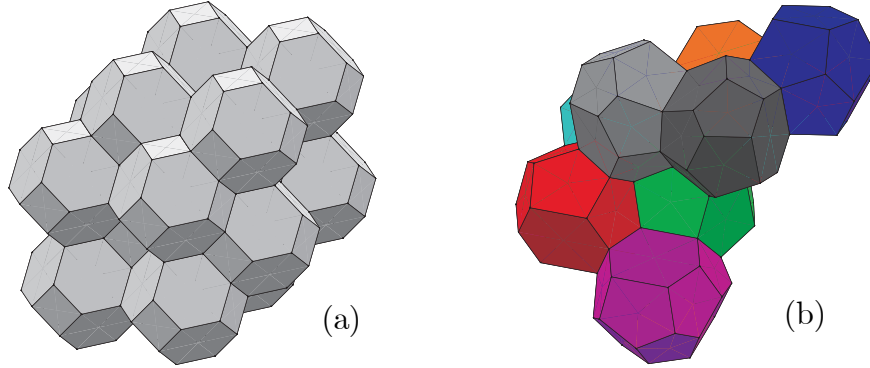


Figure I.13: The structural candidates (middle and right panels) of foam based on the ideal space-filling cell (left panels). The Kelvin tetrakaidecahedron array (a), the Weaire-Phelan structure based on two kinds of cells, one is an irregular dodecahedron and the other is a hexagonal trapezohedron (b).

closed-cell structures^[123], cancellous bone^[124]. The idealized periodic unit cell is often considered in the simplified shape (e.g., hexagonal tiling^[125], cube^[126], tetrakaidecahedron^[25], irregular dodecahedron-tetrakaidecahedron^[127]). A tetrakaidecahedra pattern based on the space partition of equal-volume cells was proposed in 1887 by Lord Kelvin^[128]. This idealized structure based on tetrakaidecahedric cells reconstructed by translations of the classical body-centered cubic lattice. The Kelvin cell [see Figure I.13(a)] has been successfully used for idealizing foams. For isotropic structures, the ligament length of the Kelvin cell is equal to L_l , that is determined by the cell size of $D_b = 2\sqrt{2}L_l$. The number of faces per cell is 14 (six squares and eight hexagons), and the number of edges per face is equal to $5.14 \approx (6 \times 4 + 8 \times 6)/14$. These values seem to be close to the main distribution of 14-faced cells and 5-edged faces presented in previous works Matzke (1946)^[78] and Kraynik et al. (2003)^[129]. An observed good agreement between predicted and measured results of sound absorption coefficients (i.e., results from acoustic modeling of several series samples of highly porous polyurethane foam^[26,27,130]) shows that Kelvin packing as a good periodic unit cell may be used to simulate and understand the acoustic performance of these materials.

However, a series of works related to foam morphology^[78,129,131,132] indicated also that the proportion of 5-edged faces is more than 50%. The resulting length distribution in the foam generated by minimum energy approach showed that the length varying from to 0.75 to 1.25 of the average length, and the maximum occurrence of the average length is around 30% even in a relaxed structure^[129,132]. These features of morphology can be covered by a structure named the Weaire-Phelan structure consisting of eight equal volume cells [two irregular dodecahedron and six like-tetrakaidecahedron, Figure I.13(b)] proposed by Denis Weaire and Robert Phelan in the year of 1994^[133]. This equal volume cell pattern could be a good candidate of an idealized unit cell for foaming structures^[127].

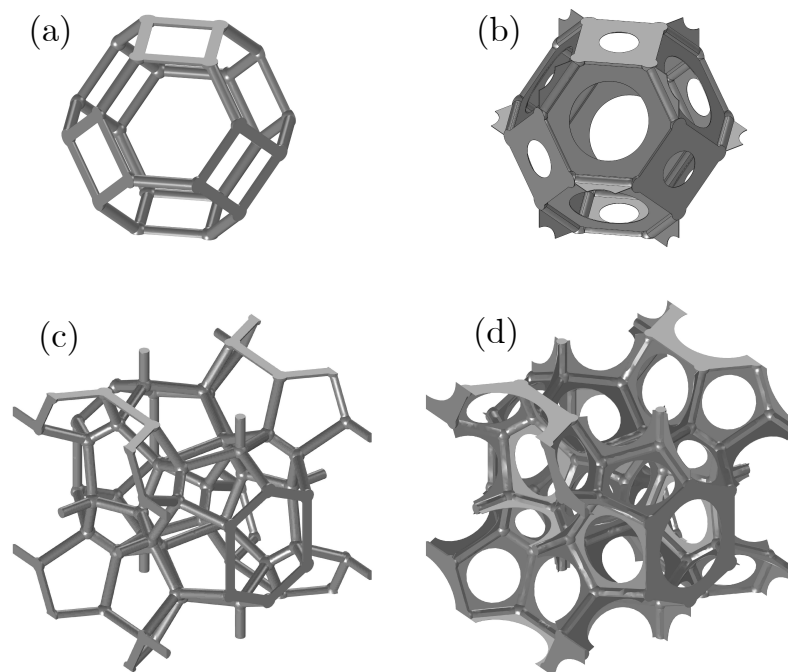


Figure I.14: The idealized framework of foaming skeleton based on the Kelvin (top) and the Weaire-Phelan (bottom) pattern. The struts are treated as a cylindrical shape and connected to each other at a spherical node. The thin membrane (right parts) in closed-cell foams is idealized by an aperture film having a given closing rate at all cell windows.

It is seen that not only the cell shape but strut or ligament shape is also interested in various works associated with cellular morphology and properties. In real cellular foams, the ligaments seem to have a concave or Plateau border shape [Figure I.15(b)], however this can be treated as several simple cross-sections such as circle [Figures I.14(a) and I.14(c)], triangle [Figure I.15(a)], square, or some polygons^[134]. In practice, some frameworks based on struts with simple shapes could not be a difficult task by using CAD software or directly generating in the commercial finite element software packages (e.g., COMSOL, ABAQUS, etc.), whereas it might not be easy to create ligament shape that mimics with the real morphology of materials. For an example of concave shape [Figure I.15(b)], this shape can be evolved from an original equilateral triangular one [Figure I.15(a)] by using Surface Evolver^[135]. Figure I.15(c) also depicts a skeleton of Kelvin unit cell based on cylindrical ligaments having a variation of the cross-sectional area along the length, such a shape was used to study Aluminium foam morphology^[136].

In terms of membrane cellular foams, thin membranes or solid films have an interesting influence on acoustical performance^[28,75,79,130,137]. At a certain cell scale, membranes may close partly or fully the pore cells^[27,83], so that the morphology connectivity of the closed-cell structure is sometimes still more different from the case of open-cell in terms of modeling

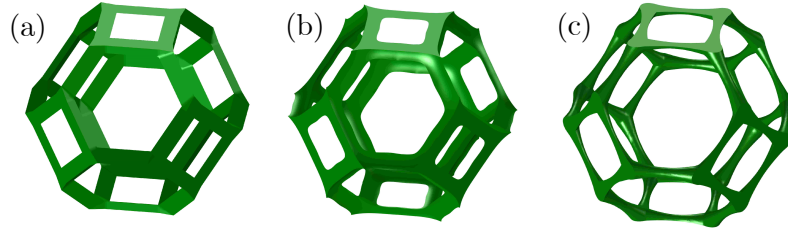


Figure I.15: The cell unit in Kelvin structure with different ligament shapes: equilateral triangular (left), concave (middle), and circular a variation of cross sectional area along the length (right).

and characterizing. Membrane connectivity may change the propagation behavior of the sound wave in such cellular materials. To take the membrane level into account, several parameters are provided such as membrane closed rate^[130,138], reticulated ratio^[27,79], cell openness^[28,139]. The Kelvin and Weaire-Phelan unit cells with a membrane closing rate in cell walls are shown in the right parts of Figure I.14.

I.4.2 Numerical estimations of macroscopic properties

Multiscale asymptotic modeling is a homogenization technique which is suitable for analysing of wave propagation in porous materials^[140]. In the simplified case where the porous solid phase is assumed to be perfectly rigid, one may consider the porous medium as an equivalent fluid subject to visco-thermal dissipations through two parameters: the effective mass density and the effective bulk modulus. Numerically, two following numerical approaches are most used to compute these effective qualities based on the up-scaling homogeneous technique of representative elementary volumes. These two numerical models of interest are introduced as the ‘hybrid’ (i.e., effective fluid at very low and high frequency regimes) and ‘direct’, where ‘direct’ means completely numerical at each frequency of interest.

I.4.2.1 Direct approach

In order to describe the linear acoustic phenomena occurring in a porous medium, a direct approach is used to solve the frequency-domain viscous-thermal governing equations and associated boundary conditions for harmonic waves characterized by frequency.

In a porous medium with an assumption that its solid skeleton is rigid perfectly, the governing equations of fluid properties in the pore domain Ω_f and on the fluid-solid interface $\partial\Omega$ may be written by,

$$\frac{p}{P_0} = \frac{\rho}{\rho_0} + \frac{\tau}{\tau_0} \quad \text{in } \Omega_f, \quad (\text{I.14a})$$

$$\rho_0 j \omega \mathbf{v} = -\nabla p + (\lambda + \mu) \nabla(\nabla \cdot \mathbf{v}) + \mu \Delta \mathbf{v} \quad \text{in } \Omega_f, \quad (\text{I.14b})$$

$$j\omega \frac{\rho}{\rho_0} = -\nabla \cdot \mathbf{v} \quad \text{in } \Omega_f, \quad (\text{I.14c})$$

$$\rho_0 j\omega C_p \tau = j\omega p + \kappa \Delta \tau \quad \text{in } \Omega_f, \quad (\text{I.14d})$$

$$\mathbf{v} = 0, \quad \tau = 0 \quad \text{on } \partial\Omega, \quad (\text{I.14e})$$

in which p , τ , \mathbf{v} , and ρ are respectively the fluid pressure, temperature, velocity, and density fields. The shear and bulk viscosities, specific heats at constant pressure, and heat conductivity are denoted by μ , λ , C_p , and κ , respectively.

Let us introduce two scales: the unit length l of the periodicity of a periodic structure on the micro-scale, and the frequency-dependent wavelength L . Assuming that the two scales differ significantly and that the scale ratio $\varepsilon = l/L$ is much smaller than 1. A space variable on macro-scale x and a space variable on micro-scale y are introduced in the asymptotic method. Following Sanchez-Palencia^[140], the asymptotic expansions of physical variables (\mathbf{v} , p , and τ) are given below:

$$\begin{aligned} \mathbf{v} &= \mathbf{v}^{(0)}(x, y) + \varepsilon \mathbf{v}^{(1)}(x, y) + \varepsilon^2 \mathbf{v}^{(2)}(x, y) + \dots, \\ p &= p^{(0)}(x, y) + \varepsilon p^{(1)}(x, y) + \varepsilon^2 p^{(2)}(x, y) + \dots, \\ \tau &= \tau^{(0)}(x, y) + \varepsilon \tau^{(1)}(x, y) + \varepsilon^2 \tau^{(2)}(x, y) + \dots. \end{aligned} \quad (\text{I.15})$$

We also have the forms of the gradient and Laplacian operators as follows:

$$\nabla = \nabla_x + \frac{1}{\varepsilon} \nabla_y, \quad \Delta = \Delta_x + \frac{2}{\varepsilon} \Delta_{xy} + \frac{1}{\varepsilon^2} \Delta_y. \quad (\text{I.16})$$

Rescaling the viscosity and conductivity coefficients by ε^2 in order to consider the viscous-thermal effects to occur at the micro-scale^[141], the momentum balance Eq. (I.14b) and energy equations Eq. (I.14d) can be rewritten as,

$$\rho_0 j\omega \mathbf{v} = -\nabla p + \varepsilon^2 (\lambda + \mu) \nabla (\nabla \cdot \mathbf{v}) + \varepsilon^2 \mu \Delta \mathbf{v}, \quad (\text{I.17a})$$

$$\rho_0 j\omega C_p \tau = j\omega p + \varepsilon^2 \kappa \Delta \tau. \quad (\text{I.17b})$$

Substituting the asymptotic series of physical variables in Eqs. (I.14c), (I.17a), (I.17b), these equations may be expressed in the following forms,

$$j\omega \left(\frac{p^{(0)} + \varepsilon p^{(1)} + \dots}{P_0} - \frac{\tau^{(0)} + \varepsilon \tau^{(1)} + \dots}{T_0} \right) = - \left(\nabla_x + \frac{1}{\varepsilon} \nabla_y \right) \cdot \left(\mathbf{v}^{(0)} + \varepsilon \mathbf{v}^{(1)} + \dots \right), \quad (\text{I.18a})$$

$$\begin{aligned} \rho_0 j\omega \left(\mathbf{v}^{(0)} + \varepsilon \mathbf{v}^{(1)} + \dots \right) &= - \left(\nabla_x + \frac{1}{\varepsilon} \nabla_y \right) \left(p^{(0)} + \varepsilon p^{(1)} + \dots \right) + \\ &\quad \varepsilon^2 (\lambda + \mu) \left(\nabla_x + \frac{1}{\varepsilon} \nabla_y \right) \left[\left(\nabla_x + \frac{1}{\varepsilon} \nabla_y \right) \cdot \left(\mathbf{v}^{(0)} + \varepsilon \mathbf{v}^{(1)} + \dots \right) \right] + \\ &\quad \varepsilon^2 \mu \left(\Delta_x + \frac{2}{\varepsilon} \Delta_{xy} + \Delta_y \right) \cdot \left(\mathbf{v}^{(0)} + \varepsilon \mathbf{v}^{(1)} + \dots \right), \end{aligned} \quad (\text{I.18b})$$

$$\rho_0 j\omega C_p \left(\tau^{(0)} + \varepsilon \tau^{(1)} + \dots \right) = j\omega \left(p^{(0)} + \varepsilon p^{(1)} + \dots \right) - \varepsilon^2 \left(\Delta_x + \frac{2}{\varepsilon} \Delta_{xy} + \Delta_y \right) \left(\tau^{(0)} + \varepsilon \tau^{(1)} + \dots \right). \quad (\text{I.18c})$$

Separating orders, at order ε^{-1} , it is implied that the fluid velocity may be considered as locally incompressible ($\nabla_y \cdot \mathbf{u}^{(0)} = 0$), and the macro-scale pressure is constant at the micro-scale ($\nabla_y p^{(0)} = 0$). At order ε^0 , it is found that

$$j\omega \left(p^{(0)}/P_0 - \tau^{(0)}/T_0 \right) = -\nabla_x \cdot \mathbf{v}^{(0)} - \nabla_y \cdot \mathbf{v}^{(1)}, \quad (\text{I.19a})$$

$$\rho_0 j\omega \mathbf{v}^{(0)} = -\nabla_y p^{(1)} - \nabla_x p^{(0)} + \mu \Delta_y \mathbf{v}^{(0)}, \quad (\text{I.19b})$$

$$\rho_0 j\omega C_p \tau^{(0)} = j\omega p^{(0)} + \kappa \Delta_y \tau^{(0)}. \quad (\text{I.19c})$$

At a given frequency, the following linear relationships are obtained^[15],

$$\mathbf{v}^{(0)}(x, y) = -\frac{\mathbf{k}(y, \omega)}{\mu} \cdot \nabla_x p^{(0)}, \quad p^{(1)}(x, y) = -\boldsymbol{\pi}(y, \omega) \cdot \nabla_x p^{(0)} + \hat{p}^{(1)}(x), \quad (\text{I.20a})$$

$$\tau^{(0)}(x, y) = -\frac{k'(y, \omega)}{\kappa} j\omega \tau^{(0)}(x). \quad (\text{I.20b})$$

Substituting two formulae of Eq. (I.20a) into Eq. (I.19b), and using $\nabla_y \hat{p}^{(1)} = 0$, we obtain the micro-scale dynamic viscous permeability,

$$\rho_0 j\omega \frac{\mathbf{k}(y, \omega)}{\mu} + \nabla_y \boldsymbol{\pi}(y, \omega) - \Delta_y \mathbf{k}(y, \omega) = \mathbf{I}. \quad (\text{I.21})$$

Similarly, the micro-scale dynamic thermal permeability is governed as,

$$\rho_0 j\omega C_p \frac{k'(y, \omega)}{\kappa} - \Delta_y k'(y, \omega) = 1. \quad (\text{I.22})$$

In summary, by employing the multi-scale asymptotic method, one can obtain the following decoupled set of partial differential equations (PDEs)^[24,142]:

(i) Momentum equation with no-slip boundaries,

$$j\omega \frac{\rho_0}{\mu} \mathbf{k} + \nabla \boldsymbol{\pi} - \Delta \mathbf{k} = \mathbf{I} \quad \text{with} \quad \nabla \cdot \mathbf{k} = 0 \quad \text{in} \quad \Omega_f, \quad (\text{I.23a})$$

$$\mathbf{k} = 0 \quad \text{on} \quad \partial\Omega, \quad (\text{I.23b})$$

$$\mathbf{k} \quad \text{and} \quad \boldsymbol{\pi} : \Omega - \text{periodic}. \quad (\text{I.23c})$$

(ii) Energy equation with isothermal boundaries,

$$\frac{\rho_0 N_{pr}}{\mu} j\omega \rho_0 k' - \Delta k' = 1 \quad \text{in} \quad \Omega_f, \quad (\text{I.24a})$$

$$k' = 0 \quad \text{on} \quad \partial\Omega, \quad (\text{I.24b})$$

$$k' : \Omega - \text{periodic}. \quad (\text{I.24c})$$

We can determine directly the macro-scale effective density and effective bulk modulus,

$$\begin{aligned} \rho(\omega) &= \frac{\mu\phi}{j\omega} \underline{\mathbf{k}}^{-1}, \\ K(\omega) &= \gamma P_0 \left[\gamma - (\gamma - 1) \frac{\rho_0 N_{pr}}{\mu} \frac{j\omega \underline{k}'}{\phi} \right]^{-1}, \end{aligned} \quad (\text{I.25})$$

where N_{pr} is the Prantdl number, and the dynamic viscous permeability $\underline{\mathbf{k}}$ and thermal permeability \underline{k}' are estimated as follows,

$$\underline{\mathbf{k}} = \phi \langle \mathbf{k} \rangle, \quad \underline{k}' = \phi \langle k' \rangle. \quad (\text{I.26})$$

The notion $\langle \cdot \rangle$ refers to an averaging operator over the domain of interest, in the fluid phase $\langle \cdot \rangle_{\Omega_f} = \int_{\Omega_f} (\cdot) dV / \int_{\Omega_f} dV$.

I.4.2.2 Hybrid approach

From a macroscopic perspective, the fluid equivalent approach is applied where a rigid porous medium is substituted by an effective fluid characterized by the dynamic density and bulk modulus. The frequency-dependent function of effective density and bulk modulus of the air in pores are related to dynamic tortuosity $\tilde{\alpha}(\omega)$ and dynamic compressibility $\tilde{\beta}(\omega)$ as follows:

$$\rho(\omega) = \rho_0 \tilde{\alpha}(\omega), \quad K(\omega) = \frac{K_a}{\tilde{\beta}(\omega)}, \quad (\text{I.27})$$

where ρ_0 is the density of air at rest, $K_a = \gamma P_0$ is the air adiabatic bulk modulus, P_0 is the atmospheric pressure, $\gamma = C_p/C_v$ is the specific heat ratio at constant temperature with C_p and C_v being the specific heat capacity at constant pressure and volume, respectively.

The dynamic viscous tortuosity defined by analogy with the response of an ideal (non-viscous) fluid whose components are real-valued and frequency independent,

$$\rho_0 \tilde{\alpha}_{ij}(\omega) \frac{\partial \langle v_j \rangle}{\partial t} = -G_j. \quad (\text{I.28})$$

$\tilde{\alpha}_{ij}(\omega)$ is related to the dynamic viscous permeability $\tilde{k}_{ij}(\omega)$ by $\tilde{\alpha}_{ij}(\omega) = \nu\phi/j\omega\tilde{k}_{ij}(\omega)$ in which, $\nu = \eta/\rho_0$ is the air kinematic viscosity, and η is the air viscosity.

Similarly, a compressibility effect is also observed at macro-scale in the acoustic response of a thermo-conducting fluid filled porous media, where a second convenient response factor is the normalized dynamic compressibility $\tilde{\beta}(\omega)$ which varies from the isothermal to the adiabatic value when frequency increases,

$$\frac{\tilde{\beta}(\omega)}{K_a} \frac{\partial \langle p \rangle}{\partial t} = -\nabla \cdot \langle \mathbf{v} \rangle, \quad (\text{I.29})$$

here, $\tilde{\beta}(\omega)$ is directly related to the dynamic (scalar) thermal permeability^[15] by means of the relation $\tilde{\beta}(\omega) = \gamma - (\gamma - 1)j\omega\tilde{k}'(\omega)/\nu'\phi$ with $\nu' = \kappa/\rho_0 C_p$.

Based on a locally plane interface, having no fractal character, the long-wavelength frequency dependence of the visco-thermal response factors $\tilde{\alpha}_{ij}(\omega)$ and $\tilde{\beta}(\omega)$ have to respect definite and relatively universal behaviors^[12,143,144] (namely causality through the Kramers-Kronig relation), similarly to the models used for relaxation phenomena in dielectric properties. The equivalent dynamic tortuosity of the material and the equivalent dynamic compressibility of the material are $\tilde{\alpha}_{eqij}(\omega) = \tilde{\alpha}_{ij}(\omega)/\phi$ and $\tilde{\beta}_{eq}(\omega) = \phi\tilde{\beta}(\omega)$.

Simple analytic admissible functions for the fluid phase effective properties of isotropic porous media are^[12,13,15]:

$$\tilde{\alpha}(\omega) = \alpha_\infty \left[1 + \frac{\mathcal{F}(\varpi)}{j\varpi} \right], \quad (\text{I.30a})$$

$$\tilde{\beta}(\omega) = \gamma - (\gamma - 1) \left[1 + \frac{\mathcal{F}'(\varpi')}{j\varpi'} \right]^{-1}, \quad (\text{I.30b})$$

where \mathcal{F} and \mathcal{F}' representing dimensionless viscous and thermal shape functions are given:

$$\mathcal{F}(\varpi) = 1 - P + P\sqrt{1 + \frac{j\varpi M}{2P^2}}, \quad (\text{I.31})$$

$$\mathcal{F}'(\varpi') = 1 + P' + P'\sqrt{1 + \frac{j\varpi' M'}{2P'^2}},$$

and dimensionless viscous ϖ and thermal ϖ' angular frequencies are estimated by the following expression:

$$\varpi = \frac{\omega\rho_0 k_0 \alpha_\infty}{\eta\phi}, \quad \varpi' = \frac{\omega\rho_0 k'_0 N_{pr}}{\kappa\phi}, \quad (\text{I.32})$$

where N_{pr} is the Prandtl number, and κ is the coefficient of the thermal conduction. Factors M and M' represent dimensionless viscous and thermal shape factors, respectively, while P and P' represent dimensionless supplementary parameters (see Eq. I.6).

It can be seen that the frequency-dependent descriptions of effective density $\rho(\omega)$ and effective buck modulus $K(\omega)$ were reconstructed based on a set of 8 parameters involving ϕ , Λ' , Λ , k'_0 , k_0 , α_∞ , α_0 and α'_0 . Excluding two geometrical parameters (the porosity ϕ and the thermal characteristic length Λ'), the six remaining factors are computed numerically by an analytics-based approach that was introduced as the hybrid numerical method in the literature. The main advantage of this approach is solving three static asymptotic boundary value problems (BVPs) involving Stokes, Laplace, and diffusion-controlled reaction equations. These equations yield as follows:

- (i) Stokes problems or viscous flow for computations of the static viscous permeability k_0 and the static viscous tortuosity α_0 ^[12,145,146]:

$$\eta\Delta\mathbf{v} - \nabla p = -\mathbf{G} \quad \text{with} \quad \nabla \cdot \mathbf{v} = 0 \quad \text{in} \quad \Omega_f, \quad (\text{I.33a})$$

$$\mathbf{v} = 0 \quad \text{on } \partial\Omega, \quad (\text{I.33b})$$

$$\mathbf{v} \text{ and } p \text{ are } \Omega - \text{periodic}, \quad (\text{I.33c})$$

where $\mathbf{G} = \nabla p^m$ is the macroscopic pressure gradient acting as a source term, \mathbf{v} and p are the velocity and pressure of the fluid, respectively.

- (ii) Laplace problems or inertial flow for computations of the high frequency tortuosity α_∞ and the viscous characteristic length Λ ^[11]:

$$\nabla \cdot \mathbf{E} = 0 \quad \text{with } \mathbf{E} = -\nabla\varphi + \mathbf{e} \quad \text{in } \Omega_f, \quad (\text{I.34a})$$

$$\mathbf{E} \cdot \mathbf{n} = 0 \quad \text{in } \partial\Omega, \quad (\text{I.34b})$$

$$\varphi \text{ is } \Omega - \text{periodic}, \quad (\text{I.34c})$$

where \mathbf{e} is a given macroscopic electric field, \mathbf{E} the solution of the boundary problem having $-\nabla\varphi$ as a fluctuating part, and \mathbf{n} is the unit normal to the boundary of the pore region.

- (iii) Thermal conduction problems or thermal effect for computations of the static thermal permeability k'_0 and the static thermal tortuosity α'_0 ^[53]:

$$\nabla^2 u = -1 \quad \text{in } \Omega_f, \quad (\text{I.35a})$$

$$u = 0 \quad \text{on } \partial\Omega. \quad (\text{I.35b})$$

Chapter II

On the construction of multiscale surrogates for design optimization of acoustical materials

Preface

- **Authors and establishments:**

- **Van Hai TRINH**, Ph.D. student, Université Paris-Est, Laboratoire Modélisation et Simulation Multi Echelle, MSME UMR 8208 CNRS, 77454 Marne-La-Vallée, France.
- **Johann GUILLEMINOT**, Assistant professor, Department of Civil and Environmental Engineering, Duke University, Durham, NC 27708, USA.
- **Camille PERROT**, Associate professor, Université Paris-Est, Laboratoire Modélisation et Simulation Multi Echelle, MSME UMR 8208 CNRS, 77454 Marne-La-Vallée, France.

- **State of publication:**

- Journal: Acta Acustica united with Acustica **104**(1), 1-4.
- Submitted date: 21 October 2017; Published date: 10 January 2018.

- **Contribution of the paper:**

When micro-macro link is already predicted by numerical works with a costly computational time consumption, this paper describe techniques for handling this challenging by reconstruction a surrogate model. This metamodel allows to achieve the desired accuracy with the least possible number of sample points of reference value. In practice,

we expand the macroscopic property of interest such as sound absorption coefficient of acoustic materials as a truncated series of orthogonal polynomials with the two variables that are the considered microstructural parameters. The results of the numerical example show that the proposed framework allows the sound absorbing property to be predicted over an appropriate frequency range (a relative error, less than 2%, is observed). In term of computational cost, the evaluation of the cost function with surrogate model took about 128 seconds for a grid defined with 100×100 sampling points, whereas proceeding with the reference multiscale computation, for each configuration, it is required about 156 seconds (where only one quarter of the cell is used, by periodicity). Besides working on acoustical application concerned here, the present method can be readily developed to accommodate other constraints such as elastic properties in a multi-objective formulations. It should finally be noticed that, for real industrial application with multi-layer absorbers, this framework can be broaden for high-dimensional problems with more input parameters of interest by working on a sparse grid only.

- **V. H. Trinh's contributions:** V. H. T. performed the numerical works and participated in discussing the results and writing the manuscript.

On the construction of multiscale surrogates for design optimization of acoustical materials

V. H. Trinh,^{1,2,†} J. Guillemot,^{3,‡} and C. Perrot^{1,§}

¹⁾ Université Paris-Est, Laboratoire Modélisation et Simulation Multi Echelle, MSME UMR 8208 CNRS, 77454 Marne-La-Vallée, France, {[†]van-hai.trinh, [‡]camille.perrot}@u-pem.fr.

²⁾ Le Quy Don Technical University, Hanoi, Vietnam.

³⁾ Department of Civil and Environmental Engineering, Duke University, Durham, NC 27708, USA, [§]johann.guillemot@duke.edu.

Summary

This paper is concerned with the use of polynomial metamodels for the design of acoustical materials, considered as equivalent fluids. Polynomial series in microstructural parameters are considered, and allow us to approximate the multiscale solution map in some well-defined sense. The relevance of the framework is illustrated by considering the prediction of the sound absorption coefficient. In accordance with theoretical results provided elsewhere in the literature, it is shown that the surrogate model can accurately approximate the solution map at a reasonable computational cost, depending on the dimension of the input parameter space. Microstructural and process optimization by design are two envisioned applications.

DOI: [10.3813/AAA.919139](https://doi.org/10.3813/AAA.919139)

II.1 Introduction

The inverse design of materials has recently gained popularity in both academia and industry. Materials by design approaches typically require (i) the construction of a mapping between the microstructural features at some relevant scale and the properties of interest (with a desired level of accuracy), and (ii) the design of an optimization algorithm that can efficiently explore innovative solutions. In this paper, we investigate the use of a multiscale-informed polynomial surrogate to define an approximation of the macroscopic acoustical properties in terms of microstructural variables.

Let \mathbf{m} denote the vector of microstructural parameters to be optimized, and assume that \mathbf{m} belongs to some admissible closed set $\mathcal{S}_{\mathbf{m}} = \times_{i=1}^n [a_i, b_i]$ in \mathbb{R}^n . Let $\mathbf{q} \in \mathcal{S}_{\mathbf{q}} \subseteq \mathbb{R}^d$ be some macroscopic quantity of interest. Microstructural design optimization then consists in

finding, using an *ad hoc* computational strategy, the optimal value \mathbf{m}^{opt} of \mathbf{m} (which may be non-unique) minimizing some application-dependent cost function J such that $J(\mathbf{q}) = J(\mathbf{q}(\mathbf{m})) =: J(\mathbf{m})$, by an abuse of notation:

$$\mathbf{m}^{opt} = \operatorname{argmin}_{\mathbf{m} \in \mathcal{S}_m} J(\mathbf{m}) . \quad (\text{II.1})$$

In practice, solving the above optimization problem (which is not convex and may exhibit many local minima) requires performing multiscale simulations a large number of times, especially for large values of n . A classical remedy to this computational burden relies on the construction of a surrogate mapping $\hat{\mathbf{q}}$ that properly approximates \mathbf{q} (that is, the map $\mathbf{m} \mapsto \hat{\mathbf{q}}(\mathbf{m})$ approaches the solution map $\mathbf{m} \mapsto \mathbf{q}(\mathbf{m})$ in some sense) and remains much cheaper to evaluate than full-field upscaling simulations. Available techniques include the use of neural networks, response surfaces^[147] and reduced-order models^[148]. Once the approximation has been defined, the optimal solution is then defined as

$$\mathbf{m}^{opt} = \operatorname{argmin}_{\mathbf{m} \in \mathcal{S}_m} \hat{J}(\mathbf{m}) , \quad \hat{J}(\mathbf{m}) = J(\hat{\mathbf{q}}(\mathbf{m})) . \quad (\text{II.2})$$

II.2 Methodological aspects

The definition of the surrogate model $\hat{\mathbf{q}}$ involves key theoretical questions (such as the characterization of convergence rates), as well as algorithmic concerns (related to the design of efficient strategies to build the metamodel, for instance). These issues have attracted much attention in various fields, especially for the computational treatment of partial differential equations, and an extensive review on this topic is beyond the scope of this letter (see e.g.,^[148] for a survey, as well as^[149,150] and the references therein for convergence results). Despite this fact, the use of metamodeling remains quite unexplored in the multiscale analysis of acoustic properties. Since the reference map $\mathbf{m} \mapsto \mathbf{q}(\mathbf{m})$ typically introduces some smoothness due to its multiscale nature, polynomial approximation techniques are natural candidates for the construction of $\hat{\mathbf{q}}$ (see e.g.,^[150]). Upon introducing the normalized vector-valued parameter $\boldsymbol{\xi}$ such that $[-1, 1] \ni \xi_i = 2/(b_i - a_i)m_i + (a_i + b_i)/(a_i - b_i)$ for $1 \leq i \leq n$, the surrogate model $\hat{\mathbf{q}}$ is then sought for as a polynomial map in $\boldsymbol{\xi}$:

$$\hat{\mathbf{q}}(\boldsymbol{\xi}) = \sum_{\boldsymbol{\alpha}} \hat{\mathbf{q}}_{\boldsymbol{\alpha}} P_{\boldsymbol{\alpha}}(\boldsymbol{\xi}) , \quad (\text{II.3})$$

where $\boldsymbol{\alpha}$ is a multi-index in \mathbb{N}^n , $P_{\boldsymbol{\alpha}}$ is the multidimensional Legendre polynomial defined as $P_{\boldsymbol{\alpha}}(\boldsymbol{\xi}) = \prod_{i=1}^n P_{\alpha_i}(\xi_i)$, and P_{α_i} is the univariate Legendre polynomial of order α_i (see e.g., Chapter 8 in^[151]). From the orthogonality of these polynomials, namely

$$\begin{aligned} \langle P_{\boldsymbol{\alpha}}, P_{\boldsymbol{\beta}} \rangle &= \frac{1}{2^n} \int_{([-1,1])^n} P_{\boldsymbol{\alpha}}(\mathbf{x}) P_{\boldsymbol{\beta}}(\mathbf{x}) d\mathbf{x} \\ &= \prod_{i=1}^n \frac{\delta_{\alpha_i \beta_i}}{2\alpha_i + 1} , \end{aligned} \quad (\text{II.4})$$

where δ is the Kronecker delta, it follows that

$$\hat{\mathbf{q}}_{\alpha} = \left(\prod_{i=1}^n (2\alpha_i + 1) \right) \langle \hat{\mathbf{q}}, P_{\alpha} \rangle . \quad (\text{II.5})$$

The choice of this polynomial basis ensures that the surrogate is uniformly accurate over the parameter space, so that no bias (noise) is generated in the evaluation of the cost function. The computation of the coefficients $\hat{\mathbf{q}}_{\alpha}$ necessitates the evaluation of n -dimensional integrals, and various techniques have been proposed in the literature to address this issue. Standard or enhanced (i.e. nested, sparse, etc.) quadrature rules can be invoked for small values of n , while (advanced) Monte Carlo simulation techniques can be used for much higher dimensions (see e.g., [72]). Below, a Gauss-Legendre quadrature rule is used for illustration purposes.

II.3 Numerical results

II.3.1 Reference solution map

In the sequel, we consider the optimization of a tetrakaidecahedron structure (see Figure II.1) for sound absorption purposes, and seek an approximation of the normal incidence sound absorption coefficient $A^{(n)}$ as a function of both the macroscopic porosity ϕ and the membrane closure rate $r_c = \delta/\delta_{\max}$. For later use, let $A^{(d)}$ be the sound absorption coefficient for a diffuse field excitation (see Eqs. (7–9) in [30]). Note that in a more general setting, the interpolation of intrinsic parameters, such as transport properties, is more appropriate, since they constitute primary variables enabling the prediction of e.g., frequency dependent response functions. Depending on the context, $A^{(n)}$ is indexed by either the frequency f or the angular frequency $\omega = 2\pi f$. We then adopt the notation $A^{(n)}(\phi, r_c; f)$ (or $A^{(n)}(\phi, r_c; \omega)$), and any variable temporarily fixed may be dropped with no notational change (when ϕ and r_c are fixed, the absorption coefficient simply reads as $A^{(n)}(f)$ or $A^{(n)}(\omega)$). While changes in the porosity ϕ can be imposed in various ways, we presently consider adapting the ligament thickness r (as shown Figure II.1) and the size D of the unit cell remains constant and equal to 0.8 mm. Furthermore, the same closure rate is imposed on all faces of the structure, which reflects both the assumed periodicity and processing constraints. Following the notations introduced in § II.1, \mathbf{m} is identified with the vector (ϕ, r_c) and $\mathbf{q} = (A^{(n)})$; hence, $n = 2$ and $d = 1$. For a given value of the microstructural parameters, $A^{(n)}(\omega)$ is obtained as $A^{(n)}(\omega) = 1 - |(Z_s(\omega) - Z_0)/(Z_s(\omega) + Z_0)|^2$, where Z_0 is the air impedance and $Z_s(\omega)$ is the normal incidence surface impedance of the equivalent fluid. For a layer of thickness L_s ($L_s = 20$ mm below), $Z_s(\omega)$ reads as $Z_s(\omega) = -jZ_c(\omega) \cot(k_c(\omega)L_s)$, where j is the imaginary unit, $Z_c(\omega)$ is the characteristic impedance and $k_c(\omega)$ denotes the wave number (with the time convention: $+j\omega t$). These quantities can be expressed in terms of

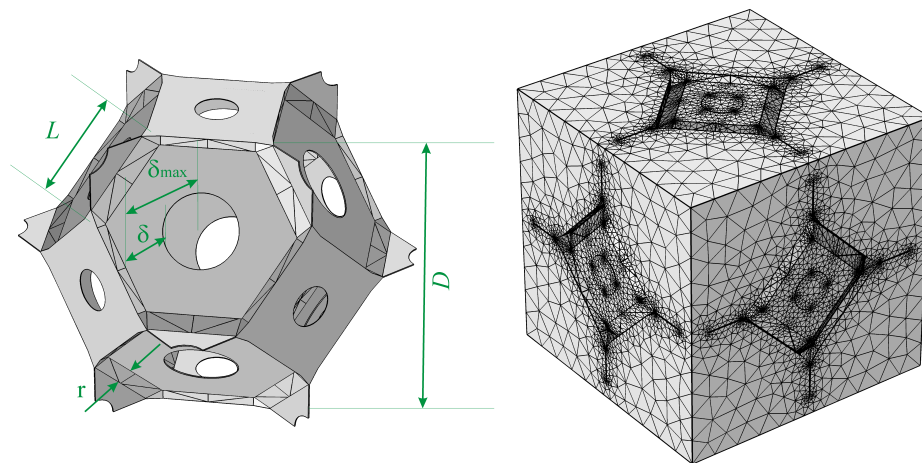


Figure II.1: Unit cell and FE mesh ($\phi = 0.97$, $r_c = 0.6$).

the effective density $\rho_{\text{eff}}(\omega)$ and effective bulk modulus $K_{\text{eff}}(\omega)$ as $Z_c(\omega) = \sqrt{\rho_{\text{eff}}(\omega)K_{\text{eff}}(\omega)}$ and $k_c(\omega) = \omega\sqrt{\rho_{\text{eff}}(\omega)/K_{\text{eff}}(\omega)}$. The effective properties can be estimated by using the semi-phenomenological JCAPL model^[12,13,15,16], which involves transport properties that are obtained by solving a set of independent boundary value problems (BVPs) (Stokes, potential flow and thermal conduction equations; see e.g., Chapter 5 in^[9] and Appendix B in^[26] for a condensed presentation of this model). In this work, these BVPs are solved by using the finite element method (at convergence, the mesh associated with the complete cell contains 214, 412 tetrahedral elements; see Figure II.1) and the commercial software COMSOL Multiphysics. For a given configuration (i.e. for given values of ϕ and r_c), the averaged computation time for the multiscale simulations is about 156 seconds. The reference solution map is shown in Figure II.2 for various frequencies.

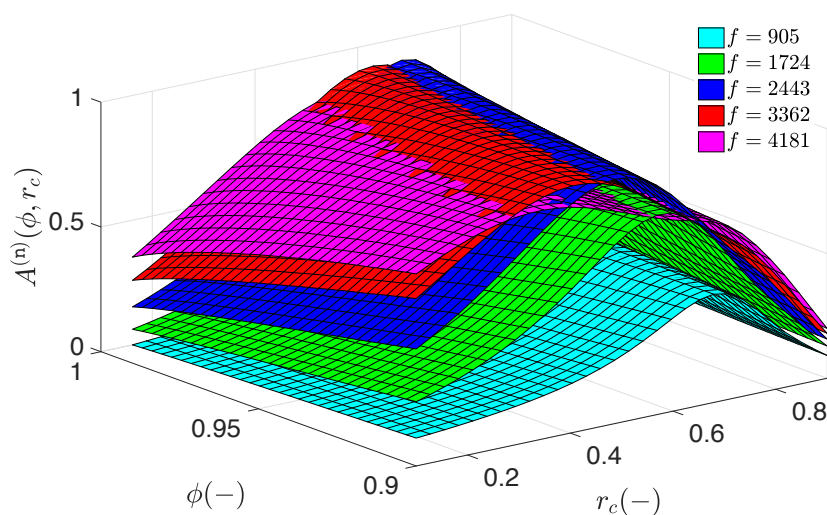


Figure II.2: Reference solution map $(\phi, r_c) \mapsto A^{(n)}(\phi, r_c)$ at different frequencies (in Hz).

II.3.2 Surrogate analysis

It follows from Eq. (II.3) that the approximant, truncated at order p , is given by

$$\hat{\mathbf{q}}_p(\boldsymbol{\xi}) = \sum_{\alpha \in \mathbb{N}^2, |\alpha|=0}^p \hat{\mathbf{q}}_\alpha P_\alpha(\boldsymbol{\xi}), \quad (\text{II.6})$$

where $\boldsymbol{\xi} = (\xi_1, \xi_2)$, $|\alpha| = \sum_{i=1}^n \alpha_i$ and $P_\alpha(\boldsymbol{\xi}) = P_{\alpha_1}(\xi_1)P_{\alpha_2}(\xi_2)$. The reduced coordinate ξ_1 corresponds to ϕ , and ξ_2 represents the closure rate r_c . The coefficients are then estimated (see Eq. II.5) as

$$\hat{\mathbf{q}}_\alpha \approx \frac{(2\alpha_1 + 1)(2\alpha_2 + 1)}{4} \sum_{i=1}^{N_Q} w_i \hat{\mathbf{q}}(\boldsymbol{\xi}^{(i)}) P_\alpha(\boldsymbol{\xi}^{(i)}), \quad (\text{II.7})$$

in which $\{w_i\}_{i=1}^{N_Q}$ and $\{\boldsymbol{\xi}^{(i)}\}_{i=1}^{N_Q}$ are the weights and points of the quadrature rule. Evaluating the multiscale model at the quadrature points represents offline stage (distributed) computations in which the reduced variables are mapped back onto the physical ones (i.e. ϕ and r_c). Convergence must be characterized with respect to both p (using e.g., a L^2 metric for increasing orders of expansion) and $n_Q = (N_Q)^{1/2}$ (for a fixed order of expansion p). In practice, the value of n_Q can be determined by analysing the convergence of the function $n_Q \mapsto \varepsilon(n_Q) = \|\hat{\mathbf{q}}_\alpha(n_Q) - \hat{\mathbf{q}}_\alpha(n_Q + 1)\|^2 / \|\hat{\mathbf{q}}_\alpha(n_Q)\|^2$, where the dependence of $\hat{\mathbf{q}}_\alpha$ on n_Q is made explicit (see Eq. (II.7)). In what follows, n_Q is determined such that $\varepsilon(n_Q) \leq 10^{-2}$ (see Figure II.3).

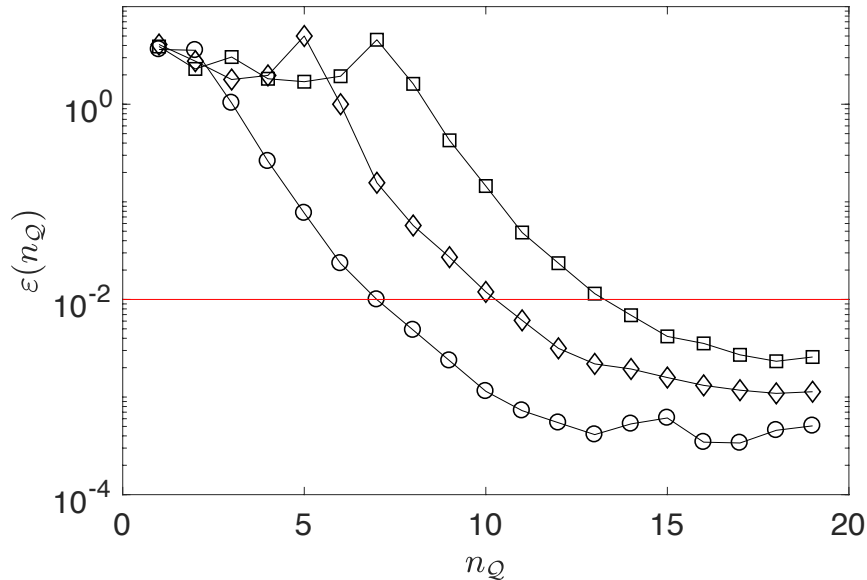


Figure II.3: Graph of the error function $n_Q \mapsto \varepsilon(n_Q)$ for $p = 5$ (circles), 10 (diamonds) and 15 (squares).

Let \mathcal{D}_p be the relative error measure defined as $\mathcal{D}_p(\phi, r_c) = |A^{(n)}(\phi, r_c) - \hat{A}_p^{(n)}(\phi, r_c)| / A^{(n)}(\phi, r_c)$,

where $\hat{A}_p^{(n)}$ is the estimate of the sound absorption coefficient (normal incidence) obtained with the surrogate model at order p . The probability density function of \mathcal{D}_p obtained for $\phi \in [0.9, 0.99]$ and $r_c \in [0.1, 0.9]$ (with a total of 900 combinations evaluated) is shown in Figure II.4, for $p = 15$ (with $n_Q = 14$, implying that 196 computations are necessary to calibrate the surrogate model). As expected, uniform convergence over the parameter space

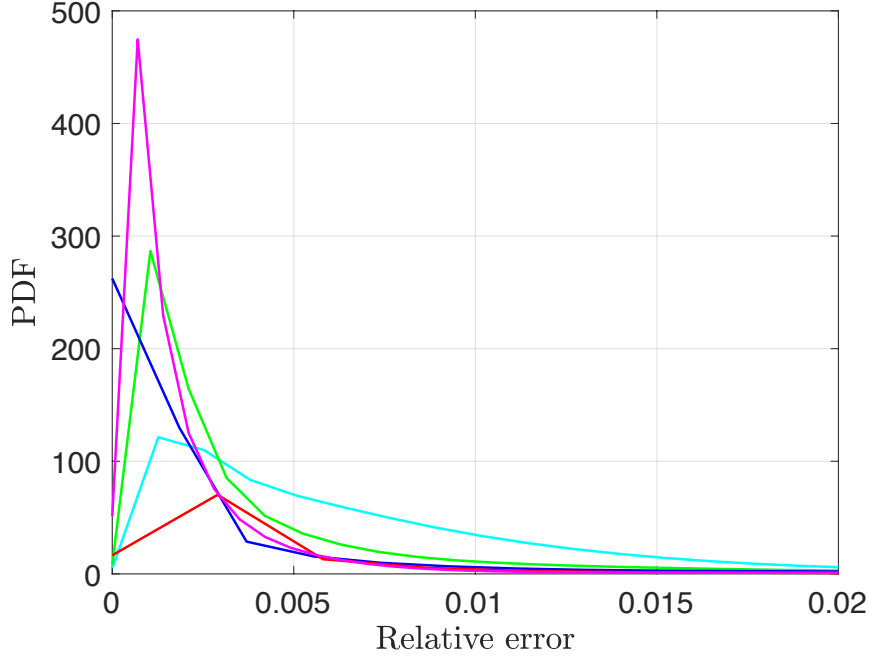


Figure II.4: PDF of the relative error for $p = 15$ and for the set of frequencies shown in Figure II.2.

is observed, with a relative error that is typically less than 2%, regardless of the frequency under consideration. It should be noticed that the apparent ordering in mean and variance, which both decrease when the frequency increases, is due to the frequency dependency of the normalizing absorption coefficient (see Figure II.2). The accuracy of the approximation can also be assessed over a wide range of frequencies, as shown in Figure II.5 for $p = 10$ ($n_Q = 11$) and $p = 15$ ($n_Q = 14$).

Let us now consider the optimization problem given by Eq. (II.2), and consider, for $\mathbf{m} = (\phi, r_c)$, the cost function $\hat{J}(\mathbf{m}) = -\hat{\mathbf{q}}_\beta(\mathbf{m})$, with $\beta \in [0, 1]$ and

$$\hat{\mathbf{q}}_\beta(\mathbf{m}) = \beta \hat{\underline{A}}_p^{(n)}(\mathbf{m}) + (1 - \beta) \hat{\underline{A}}_p^{(d)}(\mathbf{m}) \quad (\text{II.8})$$

where $\hat{\underline{A}}_p^{(n)}(\mathbf{m})$ and $\hat{\underline{A}}_p^{(d)}(\mathbf{m})$ are the averages of the sound absorption coefficients, approximated with the surrogate, over the frequency interval $[f_0, f_1]$:

$$\hat{\underline{A}}_p^{(k)}(\mathbf{m}) = \frac{1}{f_1 - f_0} \int_{f_0}^{f_1} \hat{A}_p^{(k)}(\mathbf{m}; f) df, \quad (\text{II.9})$$

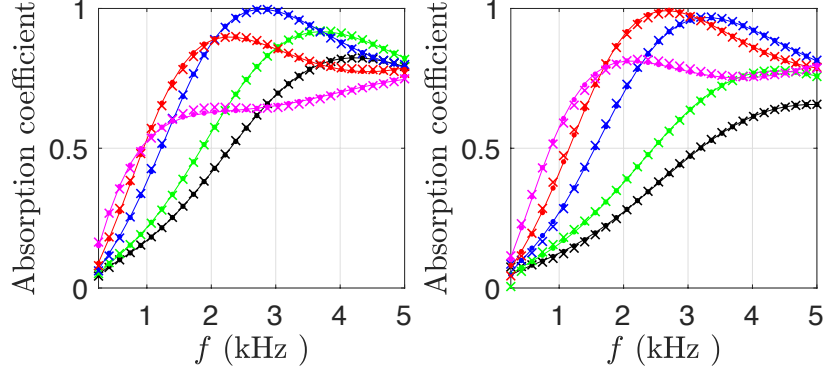


Figure II.5: Solution map for the normal incidence sound absorption coefficient. Solid line: reference; cross markers: surrogate with $p = 10$; point markers: surrogate with $p = 15$. The results are shown for $r_c = 0.1$ (black), 0.2931 (green), 0.4862 (blue), 0.5966 (red), 0.7069 (magenta), and $\phi = 0.9124$ (left panel) and $\phi = 0.9745$ (right panel).

where k stands either for n or d . Note that the dependence of \hat{q} on p is not reported to simplify notation. The charts showing the approximated sound absorption coefficients are reported in Figure II.6, and can be used to evaluate the performance of the material over ranges of values induced by process variability. Once calibrated, the surrogate model allows

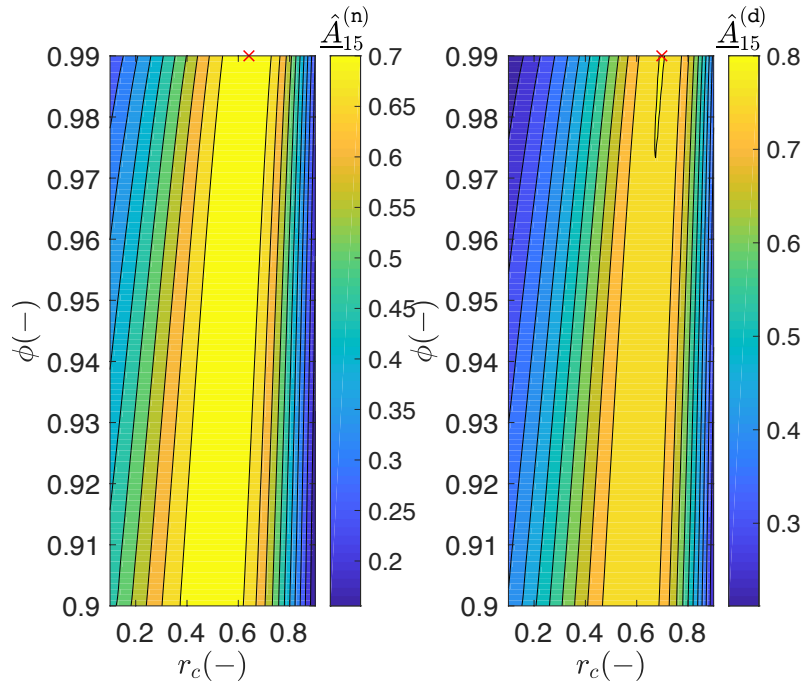


Figure II.6: Plots of the averaged absorption coefficients, with $f_0 = 250$ and $f_1 = 5,000$ Hz. The maximum value in each chart is identified with a red cross.

the cost function to be evaluated at a negligible computational expense, which opens up many

possibilities to design optimal microstructures (pore size, membrane content) under constraints related to different acoustical parameters. Whereas the proposed application was concerned with transport and sound absorbing only, it should finally be noticed that the approach can readily accommodate other constraints related to mechanical and sound insulation properties in a multi-objective formulation.

II.4 Conclusion

In this work, we have investigated the potential of polynomial metamodels to accurately approximate mappings between key microstructural features and homogenized acoustical properties. The approach relies on orthogonal polynomials and enables appropriate convergence over the parameter space to be ensured. It is shown that the framework allows the sound absorption coefficient to be predicted over an appropriate range of frequencies, so that the optimization of microstructures under various types of constraints can be envisioned at a reasonable computational cost to support the design for noise reducing materials and structures (COST Action CA15125).

Acknowledgments

The work of V. H. Trinh was supported by a fellowship awarded by the Government of Vietnam (Project 911). The work from C. Perrot was supported in part by the French National Research Agency under Grant No. ANR-13-RMNP-0003-01.

Chapter III

Tuning membrane content of sound absorbing cellular foams: Experimental evidences and multi-scale simulations

Preface

- **Authors and establishments:**

- **Van Hai TRINH**, Ph.D. student, Université Paris-Est, Laboratoire Modélisation et Simulation Multi Echelle, MSME UMR 8208 CNRS, 77454 Marne-La-Vallée, France.
- **Vincent LANGLOIS**, Ph.D. doctor, Université Paris-Est, Laboratoire Géomatériaux et Environnement, LGE EA 4508, 77454 Marne-La-Vallée, France.
- **Johann GUILLEMINOT**, Assistant professor, Department of Civil and Environmental Engineering, Duke University, Durham, NC 27708, USA.
- **Camille PERROT**, Associate professor, Université Paris-Est, Laboratoire Modélisation et Simulation Multi Echelle, MSME UMR 8208 CNRS, 77454 Marne-La-Vallée, France.
- **Yacine KHIDAS**, Ph.D. doctor, Université Paris-Est, Laboratoire Navier, NAVIER UMR 8205 CNRS, 77454 Marne-La-Vallée, France.
- **Olivier PITOIS**, Ph.D. doctor, Université Paris-Est, Laboratoire Navier, NAVIER UMR 8205 CNRS, 77454 Marne-La-Vallée, France.

- **State of publication:**

- Journal: Materials & Design.
- Submitted date: August 2018.

- **Contribution of the paper:**

This paper is devoted to characterizing the link between microscopic structural and macroscopic properties of studied membrane materials. A further parametric analysis based on unit-cell modeling is carried out to understand the effect of the microstructural parameters on the acoustical behavior of such the materials. An effective technique was developed to measure the proportion of closed cells and the size distribution of apertures for open-wall cells. Then, for each foam sample, a representative unit cell as the tetrakaidecahedron shape is reconstructed including a framework of the equivalent configurations, and then used for numerical homogenization computations. This work is confirmed by a validation in which numerical results are further compared with experimental data. Chapter IV gives details of the permeability calculation used at the end of Chapter III and includes considerations of percolation and local permeability.

- **V. H. Trinh's contributions:** V. H. T. conducted the acoustical measurements and performed the data analysis (characterization of microstructures and macroscopic parameters). V. H. T. performed the numerical calculations, participated in writing the manuscript, and discussing the results.

Tuning membrane content of sound absorbing cellular foams: Experimental evidences and multi-scale simulations

V. H. Trinh^{1,2,†}, V. Langlois^{3,‡}, J. Guillemot^{4,§},
C. Perrot^{1,¶}, Y. Khidas^{5,|†}, and O. Pitois^{5,|‡}

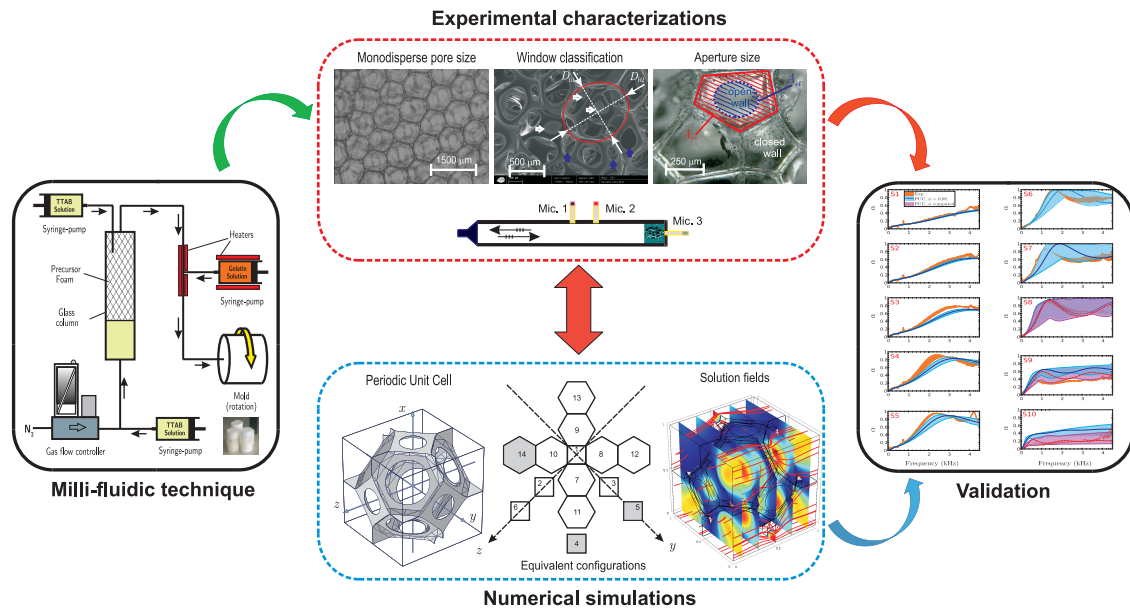
¹⁾ Université Paris-Est, Laboratoire Modélisation et Simulation Multi Echelle, MSME UMR 8208 CNRS, 77454 Marne-la-Vallée, France, {[†]van-hai.trinh,[¶]camille.perrot}@u-pem.fr.

²⁾ Le Quy Don Technical University, Hanoi, Vietnam.

³⁾ Université Paris-Est, Laboratoire Géomatériaux et Environnement, LGE EA 4508, 77454 Marne-la-Vallée, France, [‡]vincent.langlois@u-pem.fr.

⁴⁾ Department of Civil and Environmental Engineering, Duke University, Durham, NC 27708, USA, [§]johann.guillemot@duke.edu.

⁵⁾ Université Paris-Est, Laboratoire Navier, NAVIER UMR 8205 CNRS, 77454 Marne-la-Vallée, France, ^{|†}yacine.khidas@u-pem.fr, ^{|‡}olivier.pitois@ifsttar.fr.



Graphical abstract

Highlights

- Polymeric foam with monodispersed pore size and tunable membrane content were obtained using milli-fluidic techniques at constant porosity.
- Micrograph images revealed that a proper description of the membrane content requires the respective proportions of closed windows and opened windows, and the distribution of aperture sizes of opened windows.
- Tuning membrane content enabled to progressively modify the sound absorbing behavior at constant pore size from the open-cell to the closed-cell configurations.
- The calculation of visco-thermal parameters on a periodic model statistically built from the three-dimensional geometry of real foams is able to reproduce the membrane-induced effect observed on real foams.
- Tuned membrane content showed interesting specific sound absorbing properties between the open-cell and closed-cell foams.

Abstract

This work is focused on tailoring cellular foam membranes for sound absorption. Several foam configurations with a constant porosity and varying membrane content were first elaborated by using milli-fluidic techniques. This approach allows transport and sound absorbing properties to be continuously tuned on purpose, from open-cell to closed-cell foams. The morphology of these foams was then investigated using optical micrograph images. Microstructural descriptors such as the proportions of closed and opened windows and aperture size were specifically analyzed. The associated transport and sound absorbing properties were subsequently characterized using airflow resistivity and three-microphone standing wave tube measurements. The numerical reconstruction of foam samples was next addressed by considering a Periodic Unit Cell (PUC) approach on Kelvin cells. The transport properties of these virtual samples were determined by numerical homogenization, performing sequential evaluations of the parameters that govern visco-thermal losses. To overcome the limitation induced by the size of the numerical model at the pore scale, an averaging procedure was proposed. The results show that the PUC model can be used to accurately predict the transport and sound absorbing behaviors of interest. The relevance of the multiscale estimations for acoustic properties is demonstrated over the entire range of membrane content.

III.1 Introduction

Cellular foams are attractive materials for structural, thermal, and acoustical applications due to their lightweight and high specific surface area properties^[152,153]. Therefore, they were the focus of much attention during the past three decades (Gibson and Ashby, 1988; Warren and Kraynik, 1988)^[152,154]. The design of lightweight structures aims, above all, at an optimal compromise between structural properties, transport properties and acoustical performance. Ultimately, the sought-for solution should be compatible with some industrial requirements (large-scale production requirements). The microstructure-informed prediction of some physical properties of interest for a porous medium provides a theoretically sound basis for conducting optimization analyses. It can be approached in various ways, using phenomenological or truly multiscale frameworks on idealized (e.g., periodic) or random foam morphologies. Moreover, crystalline foams, and more particularly those prepared from milli-fluidic techniques, are primary regarded as model systems by physicists, due to their equal-volume pore and well-controlled polymer properties^[155]. As such, they may therefore represent a critical step in the understanding of their structure-property relations. Here, we report that the acoustical properties of tailored membrane-based cellular foams can be directly determined from numerical homogenization performed on an idealized foam mimicking the microstructure of a real foam.

Even if viscous dissipation is the main losses mechanism, modeling the acoustical properties of rigid porous medium requires to consider both the visco-inertial and thermal effects^[9]. At low frequencies, when the wavelength is much larger than the typical pore size (i.e., scale separation), visco-inertial and thermal effects might be decoupled: the visco-inertial effects are conveniently described by a macroscopically averaged fluid velocity which can be represented at macroscale by a frequency-dependent density (Johnson, 1986, Johnson et al., 1987)^[12]; and the thermal effects are described by analogy with a macroscopically averaged fluid temperature represented at macroscale by a frequency-dependent bulk modulus^[15]. Then, as long as the scale separation is valid, the dynamic behaviors of density and bulk modulus can be approximated by analytic expressions compatible with the low- and high-frequency asymptotic solutions associated to each losses mechanism. If, both effects share an intrinsic parameter which is the porosity of the open pore-space, ϕ_{op} , each mechanism also owns some specific parameters. For visco-inertial effects, three additional parameters were introduced: (1) the Darcy static permeability, k_0 , governing the low frequency behavior of effective density; (2) the tortuosity, α_∞ , associated to the high frequency regime for which the flow pattern is identical with that for an ideal fluid, except in the boundary layer (the viscous skin depth becomes much smaller than any characteristic pore size); (3) the viscous characteristic length, Λ , is a pore-volume-to-surface ratio of the pore-solid interface in which each area or volume element is weighted according to the local value of the velocity field

in the high frequency regime which represents a dynamically connected pore size entering into the analytic properties of the high-frequency limit. Regarding thermal effects, and by analogy with the viscous ones, at least two parameters were added: (4) the static thermal permeability, k'_0 , associated to the low frequency regime, which links the pressure time derivative to the macroscopic excess temperature, (5) the thermal characteristic length, Λ' , which is defined as a generalized hydraulic radius also entering into the analytic properties of the high-frequency limit. As, at high frequency, the excess temperature is everywhere the same in the pore space because this quantity is related to the adiabatic compression of the air in the material and depends only on the excess acoustic pressure that is constant at the pore scale, the effective bulk modulus is then equal to the adiabatic bulk modulus and no additional parameter is necessary. All the five previous parameters which constitutes the input parameters of the Johnson-Champoux-Allard-Lafarge model (JCAL), can be characterized experimentally^[107,120]. The relationships between these parameters and the microstructure of porous materials can be inferred in various ways: (A) by considering solutions associated to idealized structures (for example, a network of aligned tubes as in Refs.^[9,12,34,35], (B) by using semi-empirical relations based on power laws obtained on idealized structures and calibrated on experimental measurements, as done by Gibson et al.^[152] for mechanical and transport properties of cellular materials, or by Allard and Champoux for acoustical properties of fibrous materials^[9], (C) by homogenization method^[156–158] performed on numerical periodic structures mimicking the microstructure of real porous medium. For porous medium having a complex pore-space, specific tools using mathematical morphology^[90] and probability theory were used in order to generate numerical samples that are consistent with observed data with advanced imaging techniques (e.g., micro computed tomography)^[91,92,159]. Finally, as an alternative way to the approach (C) which consists to compute the only asymptotic transport parameters, numerical homogenization method can be used to compute the overall dynamic response functions of the porous medium – frequency by frequency – associated to the visco-thermal effects^[24,159–162].

These different approaches have been used to study the acoustical properties of cellular foams. Depending on various factors such as the formulation, processing conditions and post-processing operations^[27,79,153], the microstructures of cellular foams can be characterized by the fraction of closed windows^[27,28,79,163] or by membrane aperture rates^[153]. In the case of polyurethane foams, a more complex distribution of membranes is observed and involves both fully closed and partially-open windows^[75]. Concerning the acoustical properties, the effect of closed windows was studied by Doutres et al.^[27,79] with a semi-empirical approach (B), and by Park et al.^[28] with a numerical homogenization approach (C) performed on a Kelvin cell (tetrakaidecahedron) microstructure. The effect of the window aperture was studied by Perrot et al. with the approach (C) performed on a Kelvin structure. By another approach, based on the numerical homogenization of Biot equations, Goa et al. have studied

the acoustic properties of foams having both open and closed windows. They have proposed a homogenization model based on a simple mixing law built by parallel association of two types of cells: fully open cells (without any membrane) and partially closed cells. The Biot theory^[34,35] used by these authors makes it possible to take into account the effect of the deformations of the solid skeleton, but is probably not the most appropriate to study in detail the viscous and thermal losses^[12]. Numerical homogenization methods performed on an appropriated structure (C), such as Kelvin or Weaire Phelan structures, encapsulate both realistic (the model and the geometry of the foam are quantitatively comparable) and parametrizable salient features^[164,165] of the real microstructure, allowing cellular morphology modifications to be accounted for across the scales^[10]. This builds up an appropriate framework of discussion with chemists. At the present time, however, there was no optimal morphological configuration rising from this category which was shown to be manufactured.

Within this context, this study aims at (i) exploring whether milli-fluidic techniques^[155] can be used to tune the membrane content of cellular foams (and therefore, the transport and sound absorbing properties of these materials); (ii) assessing the effects of the membrane distribution on the sound absorbing and underlying visco-thermal properties; (iii) developing a model to predict the evolution of these macroscopic properties as a function of the aforementioned distribution. This model will be compared to other formulations proposed elsewhere in the literature, such as the Doutres et al. (DAD) model^[27,28,79,163] (which accounts for the fraction of fully opened/fully closed windows) and the Hoang and Perrot (HP) model, which is based on a homogeneous closure rate of membranes^[138,166,167].

This paper is organized as follows. In the first section, we present a simple but efficient elaboration route for obtaining low-density monodispersed polymeric foams with a tuned membrane content at constant porosity. The membrane distribution and acoustical properties of the foams thus produced are then studied using optical photomicrographs and airflow resistivity, combined with three-microphone standing wave tube measurements. In order to analyze the relationship between the membrane distribution and sound absorbing properties, a three-dimensional regular unit cell model is subsequently proposed. A comparison between the experimental values and the numerical predictions is finally provided on relevant quantities of interest.

III.2 Membrane induced-effect on sound absorption: Experimental evidence

In the next section, we detail experiments conducted on real solid foams. In particular, the foaming process, the microstructural characterization and the measurements of normal incidence sound absorption and of the macroscopic parameters are presented.

III.2.1 Elaboration of controlled polymer foams

We elaborate solid polymer foam samples having fixed values for both gas volume fraction and monodisperse bubble diameter D_b , but a tunable membrane content. The experimental procedure can be described as follows (see Fig. III.1).

1. A monodisperse precursor aqueous foam is generated. Foaming liquid, i.e., TTAB (Tetradecyl Trimethyl Ammonium Bromide) at 3 g/L in water, and nitrogen are pushed through a T-junction allowing the bubble size control by adjusting the flow rate of each fluid. Produced bubbles are collected in a glass column and a constant gas fraction over the foam column is set at 0.99 by imbibition from the top with foaming solution^[168].
2. An aqueous gelatin solution is prepared at a mass concentration C_{gel} within the range 12-18%. The temperature of this solution is maintained at $T \approx 60^\circ\text{C}$ in order to remain above the sol/gel transition ($T_{(s/g)} \approx 30^\circ\text{C}$).
3. The precursor foam and the hot gelatin solution are mixed in a continuous process thanks to a mixing device based on flow-focusing method^[169,170]. By tuning the flow rates of both the foam and the solution during the mixing step, the gas volume fraction can be set, $\phi_0 = 0.8$. Note also that the bubble size is conserved during the mixing step. The resulting foamy gelatin is continuously poured into a cylindrical cell (diameter: 40 mm; height: 40 mm) which is rotating around its axis of symmetry at approximately 50 rpm. This process allows for gravity effects to be compensated until the temperature decreases below $T_{(s/g)}$.
4. The cell is let at rest during one hour, at 5°C , and is then placed in a climatic chamber ($T = 20^\circ\text{C}$ and RH = 30%) for a week. During this stage, water evaporates from the samples and the gas volume fraction increases significantly.
5. After unmolding, a slice (thickness: 20 mm; diameter: 40 mm) is cut. The slice is used to perform acoustical measurements, while the cut extremities are used for microstructure characterizations^[75] (i.e., the peripheral surface is used to measure the pore size^[31]).

III.2.2 Characterization of the foam samples

III.2.2.1 Pore volume fraction

As the density of dried gelatin was measured to be 1.36, volume and weight measurements of the dried foam samples allow the pore volume fraction to be determined. For the gelatin concentrations used in this study, the pore volume fraction is found to vary between 0.977 and 0.983. In the sequel, this parameter is considered constant and equal to 0.980 ± 0.003 .

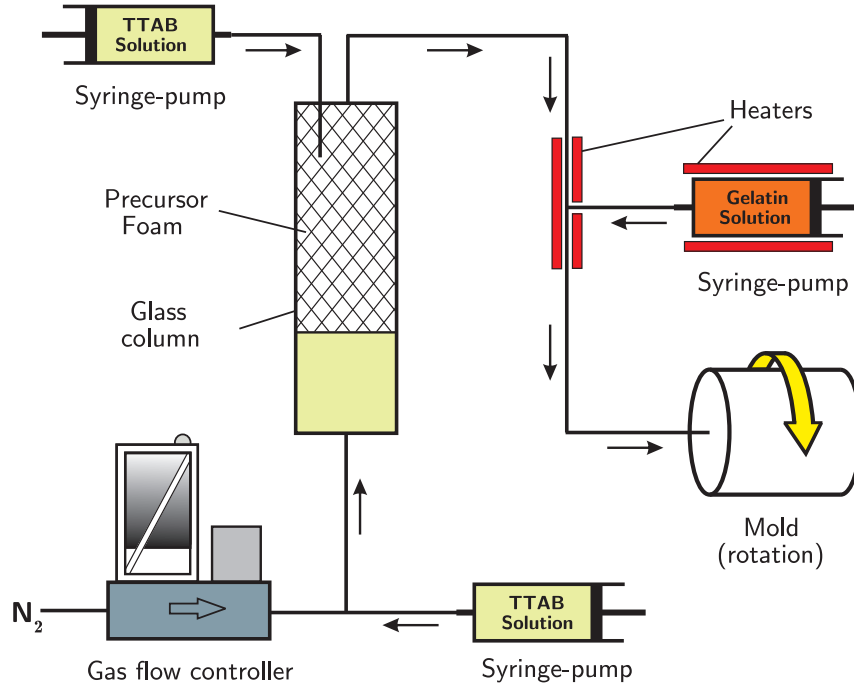


Figure III.1: Schematic description of the foaming process.

III.2.2.2 Pore size

Through a preliminary calibration, the observation of the sample surface (see Fig. III.2a) allows for the pore (bubble) size to be measured. The calibration procedure can be described as follows. Bubbles collected in the glass column (precursor in the Fig. III.1) were first sampled and squeezed between two glass plates separated by $100 \mu\text{m}$. The surface was next measured and using volume conservation, the bubble gas volume and mean bubble diameter D_b were determined (with a precision of 3%). Moreover, the mean length L_p characterizing the Plateau borders of the precursor foam at the column wall was measured. It is found that $D_b = (1.68 \pm 0.06)L_p$, with $D_b = 810 \pm 30 \mu\text{m}$ for all samples. This relation can be used to estimate the pore size in the dried gelatin samples.

In addition, the degree of anisotropy was assessed by controlling the value of the ratio D_{b1}/D_{b2} (see Fig. III.2b). Note that this degree is also considered in both the axial and radial directions. In practice, this ratio is typically smaller than 1.15 for all samples, so that the effect of geometric anisotropy will be neglected from now on.

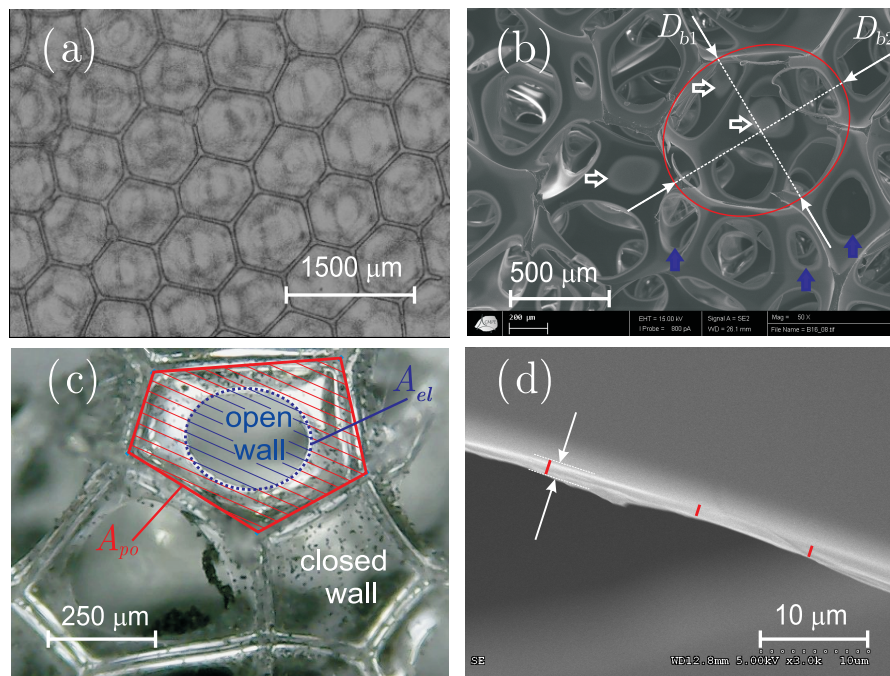


Figure III.2: Characterizations of dried-gelatin foam materials: top view of foam sample (a), degree of anisotropy (b), membrane closure rate (c), and membrane thickness (d).

III.2.2.3 Cell wall characteristics

In this work, cell walls have been characterized by observing the top and bottom surfaces of samples through a microscope (see Fig. III.2).

In terms of cellular morphology properties, the distribution of the number edges per faces shown in Fig. III.3c is in close agreement with previous experimental^[78,131] and numerical^[129,132] studies. The measured morphological properties, such as the edge length and face area distributions shown in Fig. III.3a–b, are very close to results shown in Refs.^[129,132] for foams with a monodispersed or relaxed structure. The periodic unit cell modeling is based on a Kelvin cell and is described in Section III.3.1. The locations of the distribution peaks observed in Fig. III.3a–b are close to the ones obtained in a Kelvin cell for which $L/\sqrt[3]{V_{ce}} \approx 0.45$ (with $V_{ce} = D_b^3/2$) and $A_k/\sqrt[3]{V_{ce}^2} \approx 0.38$ (with $A_k = (6 \times L^2 + 8 \times 3\sqrt{3}/2L^2)/14$). In addition, as shown in Fig. III.3c, the main proportion of 5-sided faces in all samples is consistent with the averaged number of edges of the cellular model $(4 \times 6 + 8 \times 6)/14 \approx 5.14$ (the average being taken over all the faces of the Kelvin cell).

The membrane content is evaluated by measuring the closure rate of windows separating the pores, using the following procedure. Over several hundred windows observed on both the top and bottom sample surfaces, the proportion of fully closed windows x_c is measured. Therefore, the proportion of open windows, denoted by x_o , is $x_o = 1 - x_c$. For each window,

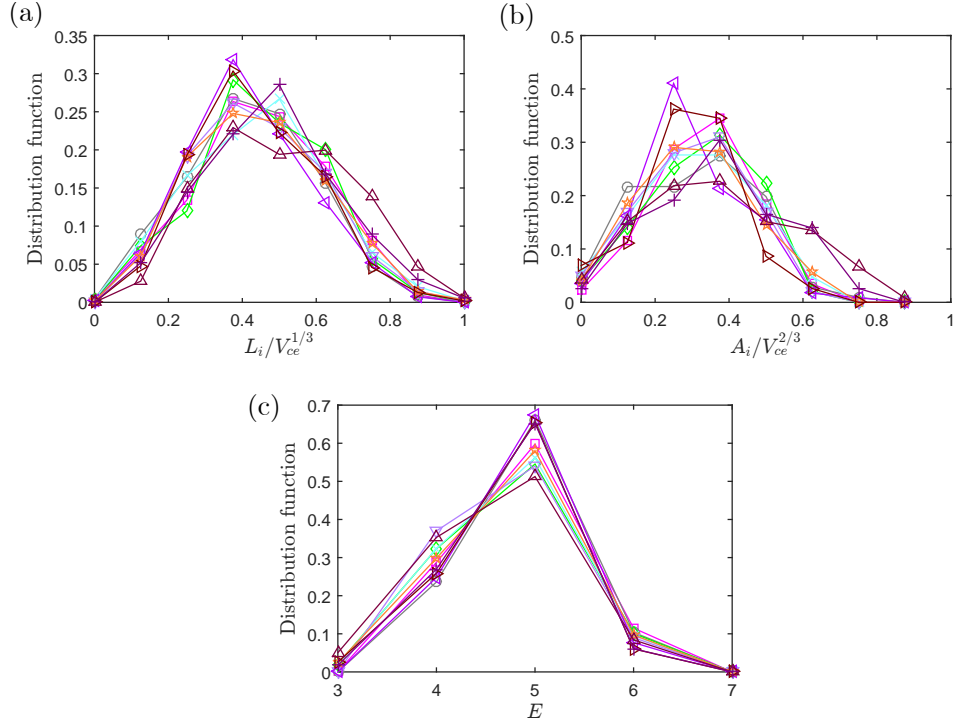


Figure III.3: Morphological properties measured on foam samples for S1(\square), S2(\circ), S3(\diamond), S4(\times), S5(∇), S6(\triangleleft), S7(\star), S8(\triangleright), S9(\triangle), and S10($+$). The results are shown for the normalized edge length distributions (a), the normalized face area distributions (b), and the distributions of faces with E edges (c).

the closure rate of membrane r_c is also measured: $r_c = 1 - \sqrt{A_{el}/A_{po}}$, where A_{po} is the window area (the area of the corresponding polygonal face) and A_{el} is the aperture area (the area of the fitting ellipse with the aperture, see Fig. III.2c). The average of the closure rate $\langle r_c \rangle$ is then calculated. In the following, a distinction will be made between the mean closure rate $\langle r_{c,c} \rangle$ of closed windows (equal to one) and the mean for open windows, denoted by $\langle r_{c,o} \rangle$. The three mean closure rates of open windows are related by the following equation: $\langle r_c \rangle = x_c + x_o \times \langle r_{c,o} \rangle$. Note that in order to get all the structural information required for the PUC modeling, this treatment is refined by separating the “square-like” windows having 4 or less edges (referred to as ‘ sq' ’), from the “hexagon-like” windows having more than 4 edges (referred to as ‘ he' ’).

The structural characterization is completed by a measurement of the membrane thickness through SEM images (Fig. III.2d). From ten micrographs, the average thickness was measured to be equal to $1.5 \pm 0.25 \mu\text{m}$, which is close to thicknesses measured for similar polymer foams^[75,167,171].

Fig. III.4 shows the cumulative distribution function of window closure rate for each sample, and Table III.1 gives the corresponding mean value $\langle r_{c,o} \rangle$ and proportion of closed

Table III.1: Microstructural characteristics of foam samples.

Sample	S1	S2	S3	S4	S5	S6	S7	S8	S9	S10
C_{gel} (%)	12	13	16	16	16	17	18	18	18	18
x_c (%)	7.1	16.7	21.0	30.7	40.4	46.3	50.8	68.8	77.9	86.2
$\langle r_c \rangle$	0.33	0.44	0.47	0.60	0.65	0.73	0.74	0.83	0.91	0.94
$\langle r_{c,o} \rangle$	0.28	0.32	0.33	0.38	0.41	0.50	0.47	0.45	0.58	0.55
x_o^{sq} (%)	20.8	18.4	15	12.7	10.4	8.2	6.6	6.1	6.3	3.4
x_c^{sq} (%)	4.2	8.1	12.4	16.1	19.8	23.6	22.1	17.9	18.2	24.9
x_o^{he} (%)	72.1	64.9	64	56.6	49.2	45.5	42.6	26.1	15.8	11.2
x_c^{he} (%)	2.9	8.6	8.6	14.6	20.6	22.7	28.7	50.9	59.7	61.3

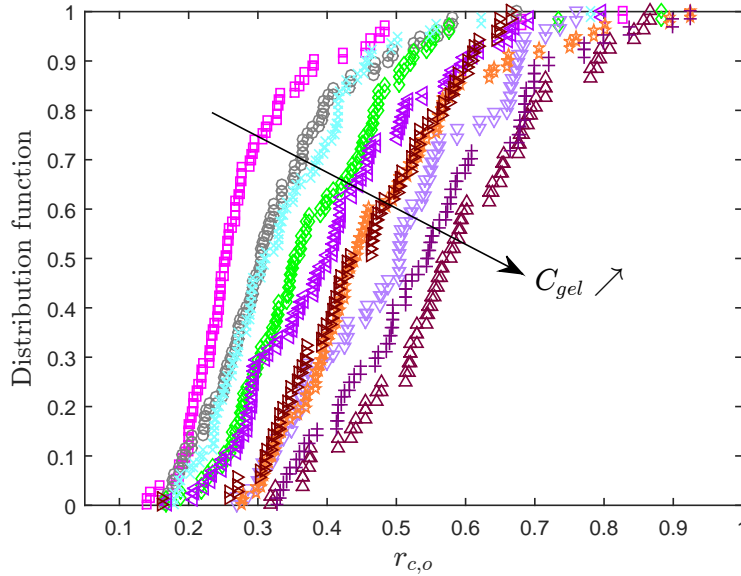


Figure III.4: Distribution function of the window closure rate measured on foam samples. The results are shown for: S1(\square), S2(\circ), S3(\diamond), S4(\times), S5(∇), S6(\triangleleft), S7(\star), S8(\triangleright), S9(\triangle), and S10($+$).

windows x_c . The gelatin concentration C_{gel} (varying from 12% to 18%) in the foaming solution appears as a control parameter to tune the membrane content of foam windows. It appears that samples prepared with the same gelatin concentration may result in different mean closure rates after drying. The mapping between the elaboration parameters and the cellular morphology parameters is given through a design of experiments.

It is worth to be mentioned that the closure rate of membranes for the larger windows tends to be slightly smaller than the one for the smaller windows, for all foam samples: $r_c^{he} \leq r_c^{sq}$. One may however simplify this feature by considering, in average, that all the open windows of the PUC have the same closure rate, given by $\langle r_{c,o} \rangle = (r_c^{sq} x_o^{sq} + r_c^{he} x_o^{he}) / (x_o^{sq} + x_o^{he})$.

As shown in Fig. III.1, such a statistical approach leads to a firm trend in which the level of closure rate $\langle r_{c,o} \rangle$ increases with increasing the proportions of fully closed windows x_c , which leads to an increase of membrane content $\langle r_c \rangle$ from foam S1 to foam S10.

III.2.3 Acoustic measurements

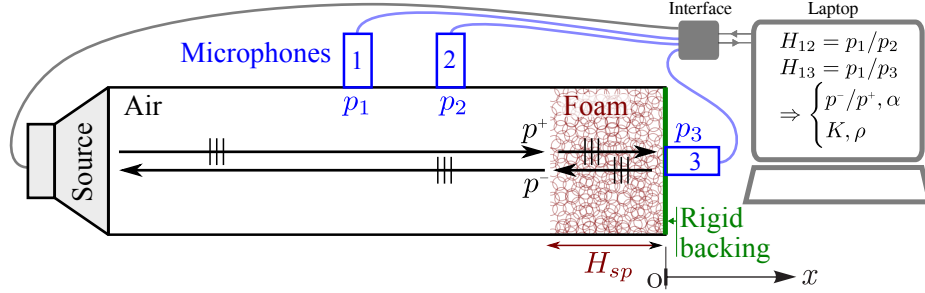


Figure III.5: Experimental setup of the three-microphone impedance tube method.

We determined the macroscopic parameters by acoustic measurements performed in a three-microphone impedance tube^[106,172] (length: 1 m, diameter: 40 mm). The test frequency ranges from 4 Hz to 4500 Hz with a step size of 4 Hz. Note that the three-microphone impedance tube method consists in measuring the pressure transfer functions, H_{12} and H_{13} , between the microphones (see Fig. III.5). The sound absorbing coefficient α is estimated as $\alpha = 1 - |p^-/p^+|^2$, in which, p^- and p^+ are respectively the pressure created by the outgoing and the ingoing waves at the surface of the sample. Also, based on these measured data, Panneton and Olny^[107,120] proposed an inverse characterization method to estimate the transport properties of porous materials. This characterization method requires the porosity and the static viscous permeability k_0 as input parameters following the approximate but robust JCAL semi-phenomenological model^[12,13,15]

Samples showing high permeability, i.e., $k_0 > 10^{-9}\text{m}^2$, were characterized by a direct measurement of the pressure drop ΔP_{sp} as a function of the volumetric air flow rate Q . This was achieved within steady state conditions in a Darcy flow regime ($\text{Re}_{D_b} = V_o D_b \rho / \eta < 1$), as specified in ISO standard ISO9053:1991. The Darcy permeability was then determined as follows:

$$k_0 = \eta Q H_{sp} / A \Delta P_{sp} , \quad (\text{III.1})$$

with the thickness of sample $H_{sp} \approx 20$ mm and the circular cross-sectional area $A \approx 12.57$ cm². More precisely, the permeability of each sample was measured for various static airflows ranging from 350 to 70 cm³/s (with incremental reductions) and determined by interpolation for a linear airflow velocity of 0.5 mm. The relative error of this measure is lower than 10%. The static viscous permeability value k_0 can also be determined as the imaginary part of the low frequency behavior of the effective density ρ ^[120]: $k_0 = -\eta / \lim_{\omega \rightarrow 0} [\Im(\omega \rho)]$.

Using this method, the air permeability is determined asymptotically based on the frequency range [80 – 800] Hz. For foams having an important fraction of closed windows, the inverse method used to characterize the transport parameters fails to determine the parameters governing the thermal effects, i.e., the thermal characteristic length Λ' [13] and the static thermal permeability k'_0 [15].

III.2.4 Experimental results and discussions

Fig. III.6 illustrates the evolution of the sound absorption coefficient in normal incidence as a function of the membrane content $\langle r_c \rangle$. As the membrane content increases, the sound

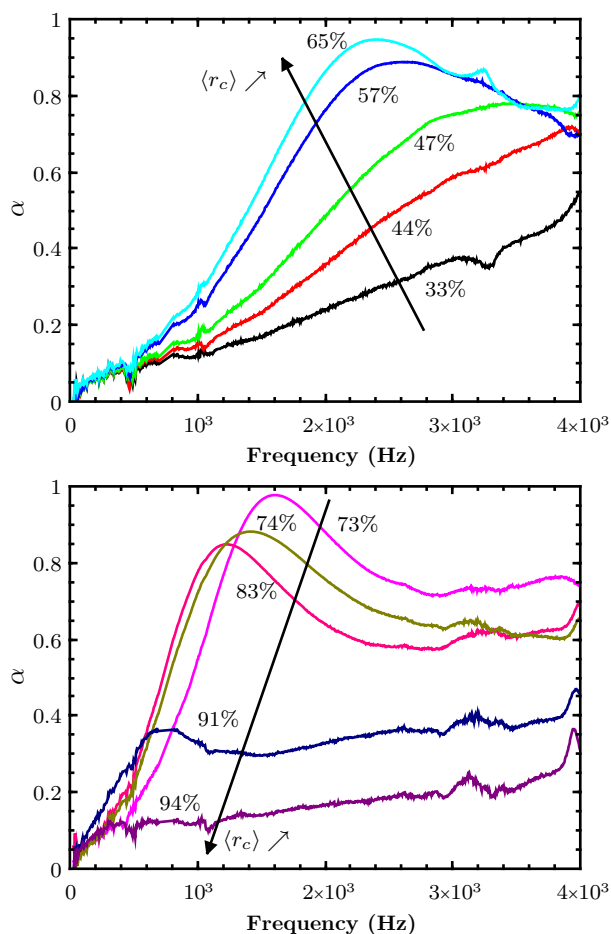


Figure III.6: Effect of the mean closure rate on the sound absorption coefficient at normal incidence with a sample thickness of 20 mm and a rigid backing.

absorption coefficients display a transition from the most opened pores (S1, $\langle r_c \rangle = 0.33$) to the least opened ones (S10, $\langle r_c \rangle = 0.94$). This analysis shows that the highest sound absorbing values (at constant thickness, 20 mm) arise for intermediate situations (S6, $\langle r_c \rangle = 0.73$). For $\langle r_c \rangle = 0.73$, visco-thermal losses are produced such that a $\sim 100\%$ absorption peak can be

obtained at ~ 1600 Hz. The sound absorption increases monotonically when r_c increases for $\langle r_c \rangle < 0.73$ and then decreases monotonically when $\langle r_c \rangle$ continues to increase above the critical value $\langle r_c \rangle = 0.73$. At low membrane contents, most of the pores are fully open: consequently, the sound waves can propagate through the foam without strong losses, and be reflected on the rigid backing. On the other hand, at high membrane contents, the sound waves can hardly penetrate into the cellular foam and most of their energy is reflected instead of being transmitted and absorbed by the porous structure.

Table III.2: Transport parameters of the elaborated foam samples.

Sample	S1	S2	S3	S4	S5	S6	S7	S8	S9	S10
Mean closure rate, $\langle r_c \rangle$	0.33	0.44	0.47	0.60	0.65	0.73	0.74	0.83	0.91	0.94
σ (kNsm $^{-4}$) direct meas.	1.7	3.0	4.0	7.0	10.6	out of range				
σ (kNsm $^{-4}$) acoustic meas.	1.7	4.6	5.1	10.5	8.7	22.8	37.3	41.4	185	1360
$\alpha_\infty(-)$	1.06	1.4	1.69	2.4	2.4	3.78	4.5	5.9	-	-
Λ (μm)	224	165	179	103	95	51	44	67	-	-
k'_0 ($\times 10^{10}\text{m}^2$)	170	190	170	-	130	-	-	-	-	-
Λ' (μm)	490	665	420	-	400	-	-	-	-	-

The following remarks can be made regarding the transport parameters (see Table III.2 and Fig. III.12).

- Because membranes obstruct some windows, increasing $\langle r_c \rangle$ reduces the mean aperture size and thus, increases the static airflow resistivity σ . As well as affecting the flow resistivity, the membrane closure rate has an important effect on tortuosity. Membrane closure rate, in turn, increases the fluid path length and therefore, the tortuosity α_∞ . The increase in tortuosity with closure rate accounts for the lowering of the frequency of the quarter wavelength resonance shown in Fig. III.6.
- Similarly, closing some windows or reducing the aperture size of open windows, reduces the values of the viscous characteristic length Λ , since Λ is defined as a pore-volume-to-surface-ratio in which a weighting procedure [Eq. (III.6)] substantially favors the smaller apertures. Note that the values of Λ/D_b are close to the mean aperture radius $\langle R_o \rangle$, calculated by including the closed windows for which $R_o = 0$ (Fig. III.12a).
- The ratio Λ'/Λ is close to 2 for small values of $\langle r_c \rangle$ (as observed in fibrous materials^[43]), however, it turns out that Λ'/Λ should increase significantly as $\langle r_c \rangle \rightarrow 1$, since, in the meantime $\Lambda \rightarrow 0$ [and $\Lambda' \rightarrow \Lambda'_{fc}$, see Eq. (III.17)].
- Furthermore, we note that the formal inequality $k'_0 \geq k_0$ ^[173] is verified experimentally, and that k'_0/k_0 also diverges when $\langle r_c \rangle \rightarrow 1$ as $k_0 \rightarrow 0$. At constant of pore size D_b , k'_0 decreases slowly with increasing membrane content (fluid-structure interface) whereas k_0 decreases strongly with membrane content (fluid obstruction).

III.3 Distinction between aperture size and fraction of closed windows: Numerical simulations

III.3.1 Unit cell modeling approach

The space-filling arrangement of Kelvin’s cell is a good representative structure for real cellular foams with equal-sized bubbles or cells of equal volume^[25,128]. The idealized Kelvin’s tetrakaidecahedron is widely used for modeling foams having high porosity^[174]. The cell is a 14-sided polyhedron with 6 squared and 8 hexagonal faces. In order to use this cell to study cellular materials, the cross sections of the struts of this framework might be modeled using different shapes such as the circular, the triangular or the concave triangular ones. Interestingly, the ligament shape has relatively limited influence on the macroscopic acoustic properties^[27,164], so that the strut can be treated using simple shapes (e.g., triangular tubes with a constant cross section). Thus, the cell skeleton is made of idealized ligaments having a length L , and an equilateral triangular cross-section of edge side r (see the Appendix A). Fig. III.7a shows the periodic unit cell used to represent the local structure of the foam samples. The corresponding finite element mesh is shown in Fig. III.7b.

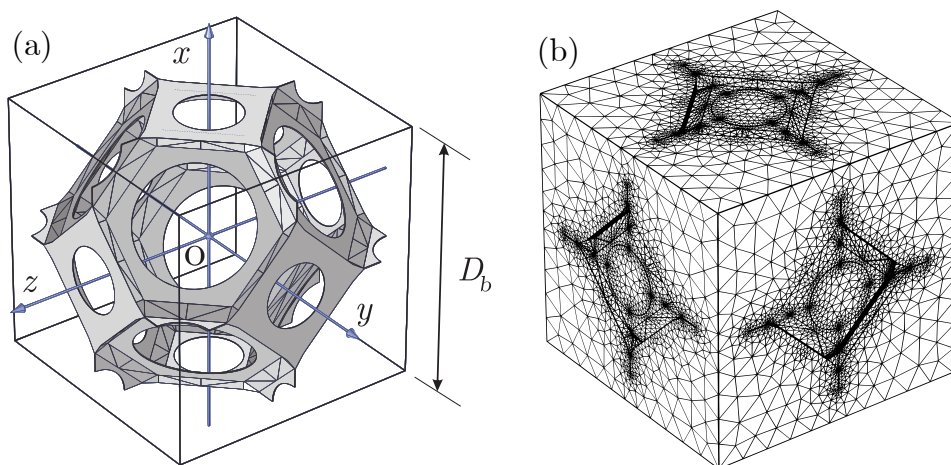


Figure III.7: PUC: skeleton geometry (a) and pore-space mesh (b).

In this work, the boundary value problems (BVPs) governing visco-thermal losses mechanisms are solved by using the finite element method (at convergence, the mesh contains 207 361 tetrahedral elements, see Fig. III.7b)^[175]. As we are interested in membrane induced-effects, we partially or totally close the windows by adding membranes. In the case of an open window, the hole in membrane is circular. As we attempt to make a numerical reconstruction of real foams, the number of closed windows and the size of window aperture in the PUC are based on the microstructural characterization of the real samples. The global closure rate of the cell can be tuned by varying the number of partially closed windows. Therefore, the number of closed hexagons and the ones of closed squares are determined by the following

equations: $N_o^{sq} = \lfloor 6 \times x_o^{sq} / (x_o^{sq} + x_c^{sq}) \rfloor$ and $N_o^{he} = \lfloor 8 \times x_o^{he} / (x_o^{he} + x_c^{he}) \rfloor$ where $\lfloor \cdot \rfloor$ denotes the nearest integer (round) function. The number of fully closed windows is then equal to $N_c^{sq} = 6 - N_o^{sq}$ and $N_c^{he} = 8 - N_o^{he}$. The aperture radius of windows is chosen in accordance with the characterized closure rate $R_o = (A_{po}/\pi)^{0.5} \times (1 - r_{c,o})$, with $A_{po} = 3\sqrt{3}D_b^2/16$ for hexagonal windows and $D_b^2/8$ for squared windows.

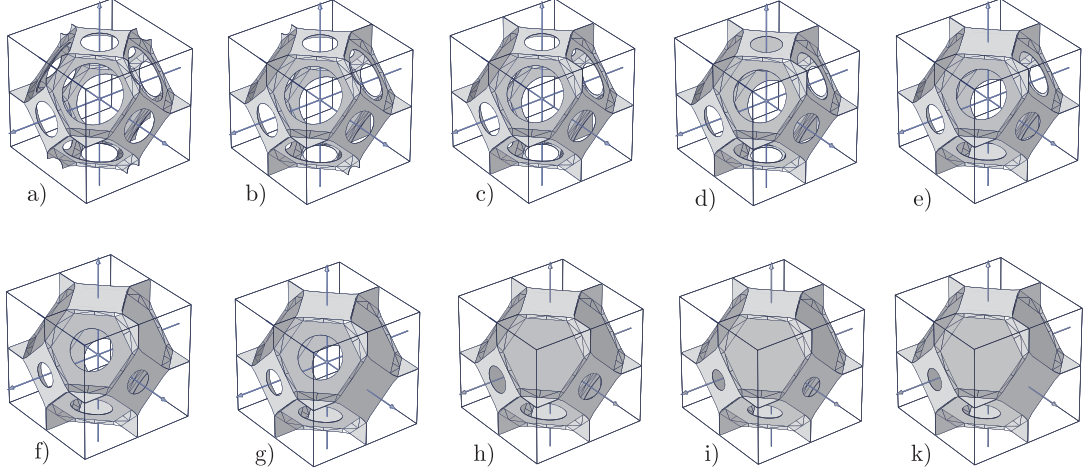


Figure III.8: Illustration of some typical reconstructed PUC corresponding to microstructural characteristics of foam samples S1 to S10. Graphs of the periodic unit cell (a)–(k) corresponding to PUC1–10. Note that, for each PUC, only a configuration among many others is depicted.

Thus, a reconstructed PUC involves N_c^{sq} fully closed squares and N_c^{he} fully closed hexagons. However, different spatial distributions of fully closed windows are possible (except in the most simple case, e.g., fully open cell). The total number of possible configurations \mathcal{N}_t is given by the product of two binomial coefficients (see Fig. III.8 for a configuration of each PUC):

$$\mathcal{N}_t = \binom{6}{N_c^{sq}} \times \binom{8}{N_c^{he}}. \quad (\text{III.2})$$

A 2D representation of the Kelvin cell is useful to localize the position the closed windows (Fig. III.9): the window numbered from 1 to 3 are associated to squares shared between two cells and located at the face of the cube enclosing the PUC, the windows numbered from 4 to 6 are associated to squares located within the cube, and the ones from 7 to 14 are associated to hexagons located within the cube. For each configuration, it is possible to define an array for which each cell is associated to a window in the PUC, and contains “1” if the window is closed or “0” otherwise. Hence, as soon as the number of closed hexagonal windows and the one of closed squared windows are defined, all possible configurations of PUC can be found by calculating all permutations of 0 and 1 in the array. We show in Fig. III.9b an

example of different configurations associated to the simple case, $N_c^{sq} = 1$ and $N_c^{he} = 0$. These configurations are also depicted in Fig. III.11a(I) in a tabular form, where each line of the table corresponds to a geometrical configuration.

Among all the possible configurations associated with the same number of closed windows, part of them have, with respect to the physical problem considered, a similar behavior. A trivial example is obtained by rotating a given configuration around the axis corresponding to the direction of sound propagation (x -axis), for instance. Other transformations (rotations, translations) exploiting the symmetries of the Kelvin cell also preserve the behavior of the cell. We define a set of 13 transformations as shown in Fig. III.10. For each transformation, by comparing the original configurations [Fig. III.11a(I)] to the transformed configurations [Fig. III.11a(II)], we can find the equivalent configurations and associate them together [Fig. III.11a(III)]. Then, by considering the results obtained on all transformations, a global calculation of equivalent configurations is performed [Fig. III.11a(IV)]; as we show in Appendix B.

Note that when the number of closed windows is important, i.e., $N_c^{sq} \geq 2$ and $N_c^{he} \geq 4$, several configurations lead to closed interconnected pores for which no flow through the PUC is possible. The number of such closed configurations, $\mathcal{N}_{t,c}$, is given in Table III.4. The ratio $\mathcal{N}_{t,c}/N_t$ provides an estimate of the open porosity ratio R_{op} corresponding to such a unit cell modeling approach: $R_{op} = \text{open porosity, } \phi_o/\text{total porosity, } \phi = 1 - (\mathcal{N}_{t,c}/N_t)$.

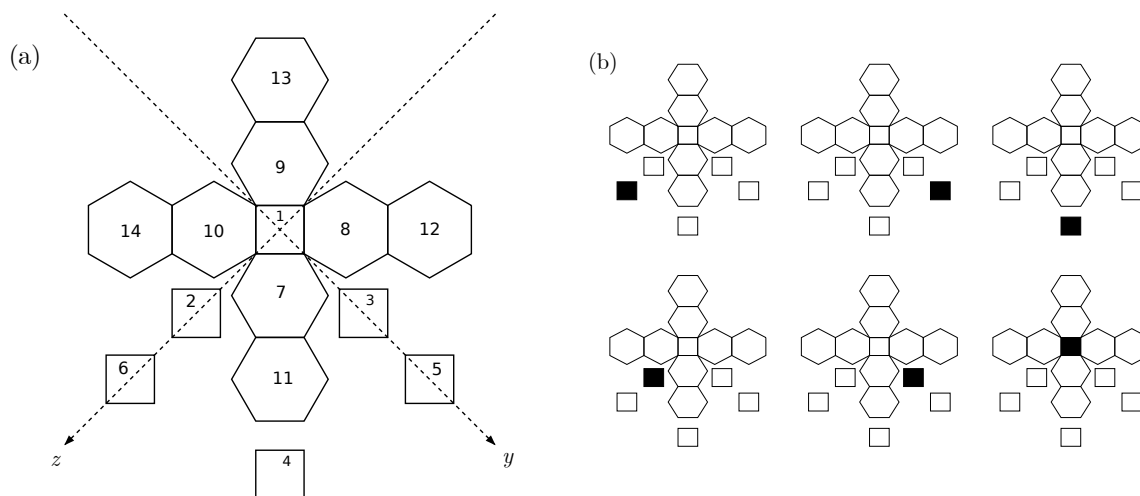


Figure III.9: (a) Reconstruction of a tetrakaidecahedron cell with a 2-dimensional pattern, direction of x axis is perpendicular with faces 1 and 4; (b) the possible configurations associated to PUC1 ($N_c^{sq} = 1$ and $N_c^{he} = 0$).

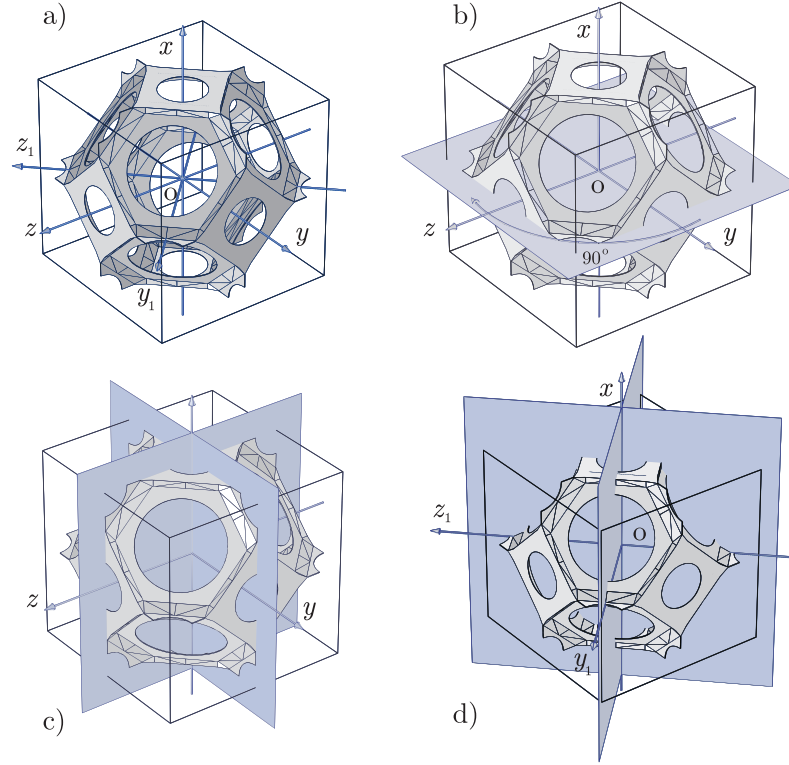


Figure III.10: The symmetry property of the periodic unit cell.

Table III.3: Equivalent configurations in various symmetry conditions.

Symmetry	Shown in	Equivalent configuration
Periodicity/Translation	Fig. III.9a	[4 5 6 1 2 3 11 12 13 14 7 8 9 10]
Origin point O	Fig. III.10a	[1 2 3 4 5 6 13 14 11 12 9 10 7 8]
Axis Ox	Fig. III.10a	[1 2 3 4 5 6 9 10 7 8 13 14 11 12]
Axis Oy	Fig. III.10a	[1 2 3 4 5 6 14 13 12 11 10 9 8 7]
Axis Oz	Fig. III.10a	[1 2 3 4 5 6 12 11 14 13 7 8 10 9]
Axis Oy ₁	Fig. III.10a	[1 3 2 4 6 5 13 12 11 14 9 8 7 10]
Axis Oz ₁	Fig. III.10a	[1 3 2 4 6 5 11 14 13 12 7 10 9 8]
Rotation 90° around Ox	Fig. III.10b	[1 3 2 4 6 5 8 9 10 7 12 13 14 11]
Plane Oyz	Fig. III.10b	[1 2 3 4 5 6 11 12 13 14 7 8 9 10]
Plane Ox ₁ y	Fig. III.10c	[1 2 3 4 5 6 10 9 8 7 14 13 12 11]
Plane Oxz	Fig. III.10c	[1 2 3 4 5 6 8 7 10 9 12 11 14 13]
Plane Ox ₁ y ₁	Fig. III.10d	[1 3 2 4 6 5 9 8 7 10 13 12 11 14]
Plane Oxz ₁	Fig. III.10d	[1 3 2 4 6 5 7 10 9 8 11 14 13 12]

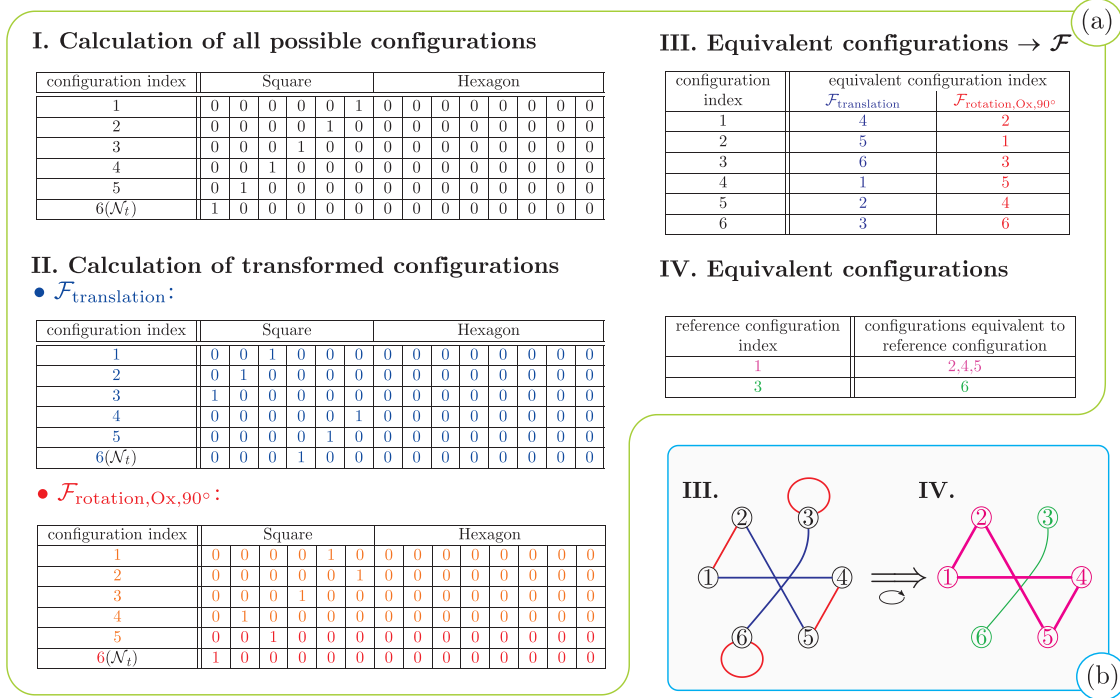


Figure III.11: Major steps of equivalent configuration calculation (a) and graphs associated to steps III. and IV. (b). This figure depicts the simple case where $N_c^{sq} = 1$ and $N_c^{he} = 0$.

III.3.2 Calculations of visco-thermal parameters

III.3.2.1 Definition of non-acoustic parameters

In this section, we briefly introduce the BVPs that are used for computing the macroscopic properties of the JCAL semi-phenomenological model with 6 input parameters. This semi-phenomenological model relies on two purely geometrical parameters (ϕ , Λ') defined directly from the local geometry of the representative unit cell as $\phi = \int_{\Omega_f} dV / \int_{\Omega} dV$, and $\Lambda' = 2 \int_{\Omega} dV / \int_{\partial\Omega} dS$. The 4 remaining transport properties are computed from the solution fields corresponding to three group of PDEs over the unit cell.

Viscous flow: The low Reynolds number flow of an incompressible Newtonian fluid is governed by the usual Stokes equations in the fluid phase^[146]:

$$\eta \Delta \mathbf{v} - \nabla \mathbf{p} = -\mathbf{G} \text{ with } \nabla \cdot \mathbf{v} = 0 \text{ in } \Omega_f, \quad (\text{III.3a})$$

$$\mathbf{v} = 0 \text{ on } \partial\Omega, \quad (\text{III.3b})$$

$$\mathbf{v} \text{ and } \mathbf{p} \text{ are } \Omega - \text{periodic}, \quad (\text{III.3c})$$

where $\mathbf{G} = \nabla \mathbf{p}^m$ is a macroscopic pressure gradient. Symbols \mathbf{v} and \mathbf{p} are the velocity and pressure of the fluid, respectively. It can be shown that the local fields of the static viscous

Table III.4: PUC characteristics corresponding to foam sample S1-S10. In particular, it illustrates the huge discrepancy between the total number of possible configurations \mathcal{N}_t and the reduced number of reference configurations \mathcal{N}_r .

Sample	S1	S2	S3	S4	S5	S6	S7	S8	S9	S10
Unit cell	PUC1	PUC2	PUC3	PUC4	PUC5	PUC6	PUC7	PUC8	PUC9	PUC10
N_c^{sq}	1	2	3	3	4	4	5	4	4	5
N_c^{he}	0	1	1	2	2	3	3	5	6	7
\mathcal{N}_t	6	120	160	560	420	840	336	840	420	48
\mathcal{N}_r	2	6	6	38	36	36	12	36	36	2
$\mathcal{N}_{t,c}$	0	0	0	0	0	0	0	94	135	32

permeability are obtained from the local velocity fields as $\mathbf{v} = -(\mathbf{k}_0/\eta)\mathbf{G}$. Thus, the static viscous permeability k_{0xx} is calculated as

$$k_{0xx} = \phi \langle \mathbf{k}_{0xx} \rangle. \quad (\text{III.4})$$

Inertial flow: In the high frequency limit, the viscous boundary layer becomes negligible and the fluid tends to behave as a perfect one, having no viscosity except in the vicinity of the boundary layer. Consequently, the perfect incompressible fluid formally behaves according to the electrical conduction problem^[12,143,176]:

$$\nabla \cdot \mathbf{E} = 0 \quad \text{with} \quad \mathbf{E} = -\nabla \varphi + \mathbf{e}, \quad \text{in } \Omega_f, \quad (\text{III.5a})$$

$$\mathbf{E} \cdot \mathbf{n} = 0, \quad \text{on } \partial\Omega, \quad (\text{III.5b})$$

$$\varphi \text{ is } \Omega - \text{periodic}, \quad (\text{III.5c})$$

where \mathbf{e} is a given macroscopic electric field, \mathbf{E} is the solution of the boundary problem having $-\nabla \varphi$ as a fluctuating part, and \mathbf{n} is the unit normal to the boundary of the pore region. The viscous characteristic length Λ and the high frequency tortuosity α_∞ are then calculated through

$$\Lambda = \frac{2 \int_{\Omega_f} |\mathbf{E}|^2 dV}{\int_{\partial\Omega} |\mathbf{E}|^2 dS}, \quad \alpha_\infty = \frac{\langle |\mathbf{E}|^2 \rangle}{\langle |\mathbf{E}| \rangle^2}. \quad (\text{III.6})$$

Thermal effect: The thermal terminology is used here but the following developments are also valid for diffusion of Brownian particles whose sizes are small with respect to a typical pore size of the medium. Heat diffusion at low frequency and Brownian motion in porous media is governed by a Poisson equation,

$$\nabla^2 u = -1, \quad (\text{III.7})$$

where u is the local field. When the frame has a sufficient thermal capacity, the excess temperature u can be considered to vanish at the pore walls, and the boundary conditions are $u = 0$ on $\partial\Omega$. The excess temperature field u is periodic. The mean value of the excess temperature field in the pore space is directly related to the definition of the (scalar) thermal permeability:

$$k'_0 = \langle u \rangle. \quad (\text{III.8})$$

III.3.2.2 Calculation of the average of non-acoustic parameters

In terms of numerical results of non-acoustic properties, the configuration of each unit cell is considered based on the spatial distribution of the fully closed faces. Of course, this distribution has no influence on the geometric parameters (i.e., the thermal characteristic length Λ' and the porosity ϕ , for PUCs without a closed pore-space).

In order to compute the effective macroscopic transport parameters, for each unit cell of foam sample, let us first introduce two averaging operators:

$$\langle \cdot \rangle_V = \frac{1}{V_f} \int_{\Omega_f} \cdot dV, \quad (\text{III.9a})$$

$$\langle g_j \rangle_{\mathcal{N}} = \frac{1}{\mathcal{N}_t} \sum_{j=1}^{\mathcal{N}_r} g_j = \frac{1}{\mathcal{N}_t} \sum_{k=1}^{\mathcal{N}_r} \mathcal{N}_k g_k, \quad (\text{III.9b})$$

in which \mathcal{N}_k is the number of equivalent configurations having the same value g_k . Hence only one representative configuration of \mathcal{N}_k is selected to perform the numerical computation. In the total number of possible configurations \mathcal{N}_t for each unit cell in Eq. (III.2), this involves typically \mathcal{N}_r reference configurations (see Section III.3.1). The values of \mathcal{N}_t and \mathcal{N}_r are summarized in Table III.4.

Then, the effective static viscous and thermal permeabilities of each foam sample were deduced from the averages of the local permeability fields k_{0xxj} and u_j of each configuration, it follows

$$k_0 = \left\langle \left\langle k_{0xxj} \right\rangle_V \right\rangle_{\mathcal{N}_t}, \quad k'_0 = \left\langle \left\langle u_j \right\rangle_V \right\rangle_{\mathcal{N}_t}. \quad (\text{III.10})$$

Similarly, the effective viscous characteristic length and high frequency tortuosity are obtained from the the solution field \mathbf{E}_j solved from the electrical conduction problems,

$$\Lambda = \frac{2 \left\langle \int_{\Omega_f} |\mathbf{E}|_j^2 dV \right\rangle_{\mathcal{N}_{t,o}}}{\left\langle \int_{\partial\Omega} |\mathbf{E}|_j^2 dS \right\rangle_{\mathcal{N}_{t,o}}}, \quad \alpha_\infty = \frac{\left\langle \left\langle |\mathbf{E}|_j^2 \right\rangle_V \right\rangle_{\mathcal{N}_{t,o}}}{\left(\left\langle \left\langle |\mathbf{E}|_j \right\rangle_V \right\rangle_{\mathcal{N}_{t,o}} \right)^2}. \quad (\text{III.11})$$

In which, Ω_f is the fluid-filled domain in the open-pore space and $\partial\Omega$ is the fluid-solid interface in a representative unit cell Ω . $\langle g_j \rangle_{\mathcal{N}_{t,o}}$ is a configuration average performed over the open configurations. Details in the above solved local fields are presented in the previous section,

note that because the number of windows is limited in the Kelvin unit-cell, for PUCs with a relatively high number of closed faces (i.e., S8 to S10), some configurations correspond to disconnected fluid flow. This leads us consider that all the corresponding solution fields are equal to zero.

III.3.3 Calculations of sound absorbing properties JCAL

From the macroscopic perspective, the equivalent-fluid approach is applied where a rigid porous medium is substituted by an effective fluid. This fluid is characterized by an effective density $\tilde{\rho}(\omega)$ ^[12] and an effective bulk modulus $\tilde{K}(\omega)$ ^[13,15] as follows^[9]:

$$\tilde{\rho}(\omega) = \rho_0 \left[\alpha_\infty - j \frac{\phi\sigma}{\omega\rho_0} \sqrt{1 + j\omega \frac{\rho_0}{\eta} \left(\frac{2\eta\alpha_\infty}{\sigma\phi\Lambda} \right)^2} \right], \quad (\text{III.12})$$

and

$$\tilde{K}(\omega) = \gamma P_0 \left[\gamma - (\gamma - 1) \left\{ 1 - j \frac{\phi\eta}{k'_0\rho_0 N_{pr}\omega} \sqrt{1 + j \frac{4k'_0{}^2 N_{pr}\rho_0\omega}{\eta\Lambda'^2\phi^2}} \right\}^{-1} \right]^{-1}. \quad (\text{III.13})$$

In these equations, ρ_0 and η are the density and dynamic viscosity of the ambient fluid at rest (i.e., air), P_0 the atmospheric pressure, $\gamma = C_p/C_v$ the ratio of heat capacities at constant pressure and volume, N_{pr} the Prantdl number, j the imaginary unit, $\omega = 2\pi f$ the angular frequency.

The wave number $\tilde{k}_c(\omega)$ and the characteristic impedance $\tilde{Z}_c(\omega)$ at normal incidence of a layer of equivalent-fluid backed by imprevious rigid wall are given by^[9],

$$\tilde{k}_c(\omega) = \omega \sqrt{\tilde{\rho}(\omega)/\tilde{K}(\omega)}, \quad \tilde{Z}_c(\omega) = \sqrt{\tilde{\rho}(\omega)\tilde{K}(\omega)}. \quad (\text{III.14})$$

The absorption coefficient of this porous layer is related to the impedance $\tilde{Z}_s(\omega)$ at the surface $x = x(-H_{sp})$ of the sample,

$$\alpha = 1 - \left| \frac{\tilde{Z}_s(\omega) - Z_0}{\tilde{Z}_s(\omega) + Z_0} \right|^2, \quad (\text{III.15})$$

with Z_0 is the impedance of the air, and $\tilde{Z}_s(\omega) = -j \frac{\tilde{Z}_c(\omega)}{\phi} \cot[\tilde{k}_c(\omega)H_{sp}]$.

III.3.4 Results and discussion

At first, we consider the prediction performance of our “two-parameters” microstructural model (at constant pore size). Fig. III.12 shows that the computed transport parameters compare well to the characterized ones. However, the computed values of tortuosity are lower than the characterized ones. These differences could be due to the limited size of our

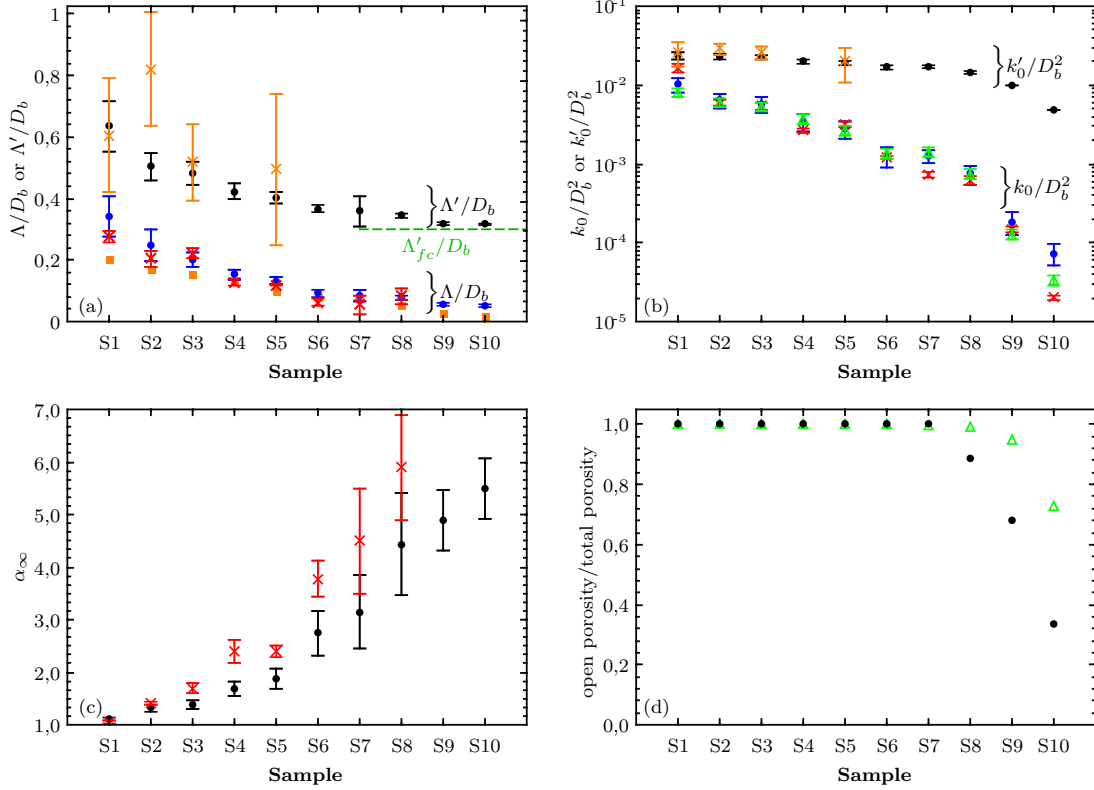


Figure III.12: Dimensionless transport properties for: real foam samples (×) and 2-parameter models: PUC computation (○), EM model (△). The mean aperture radius $\langle R_o \rangle$, calculated by including the closed windows ($R_o = 0$), is added (□) and allows for a comparison with Λ/D_b . Note that the samples S1 to S10 are ordered by increasing mean closure rates. The error bars on computed values of macroscopic parameters are calculated by considering an error on the characterization of $\langle r_{c,o} \rangle$ equal to ± 0.05 .

numerical samples. It is known that in percolating materials^[177], the number of cells required for calculations when the fraction of open windows, x_o , is close to the percolation threshold ($1.5/N_v \approx 0.11$, where $N_v = 14$ is the pore neighbor number of the Kelvin structure), should be superior to a few thousands. The fraction of open windows for sample S10, equal to $1 - 0.86 = 0.14$, is very close to the percolation threshold. We can illustrate the limitation of our unit cell modeling by comparing their predicted fraction of open porosity obtained by pore-network calculations performed on large samples in Ref.^[177]. As expected, Fig.III.12c shows that a modeling approach based on a simple PUC do not accurately predict the open porosity of the real cellular foam samples containing a high fraction of closed windows. We also note that another explanation is possible due to an experimental bias: the microstructural characterization of foam sample was done on the cut extremity of samples, and not on the foam sample used to perform the acoustic measurements. As the sample drying occurs by water transfer trough the borders of samples, the proportion of open windows in the border

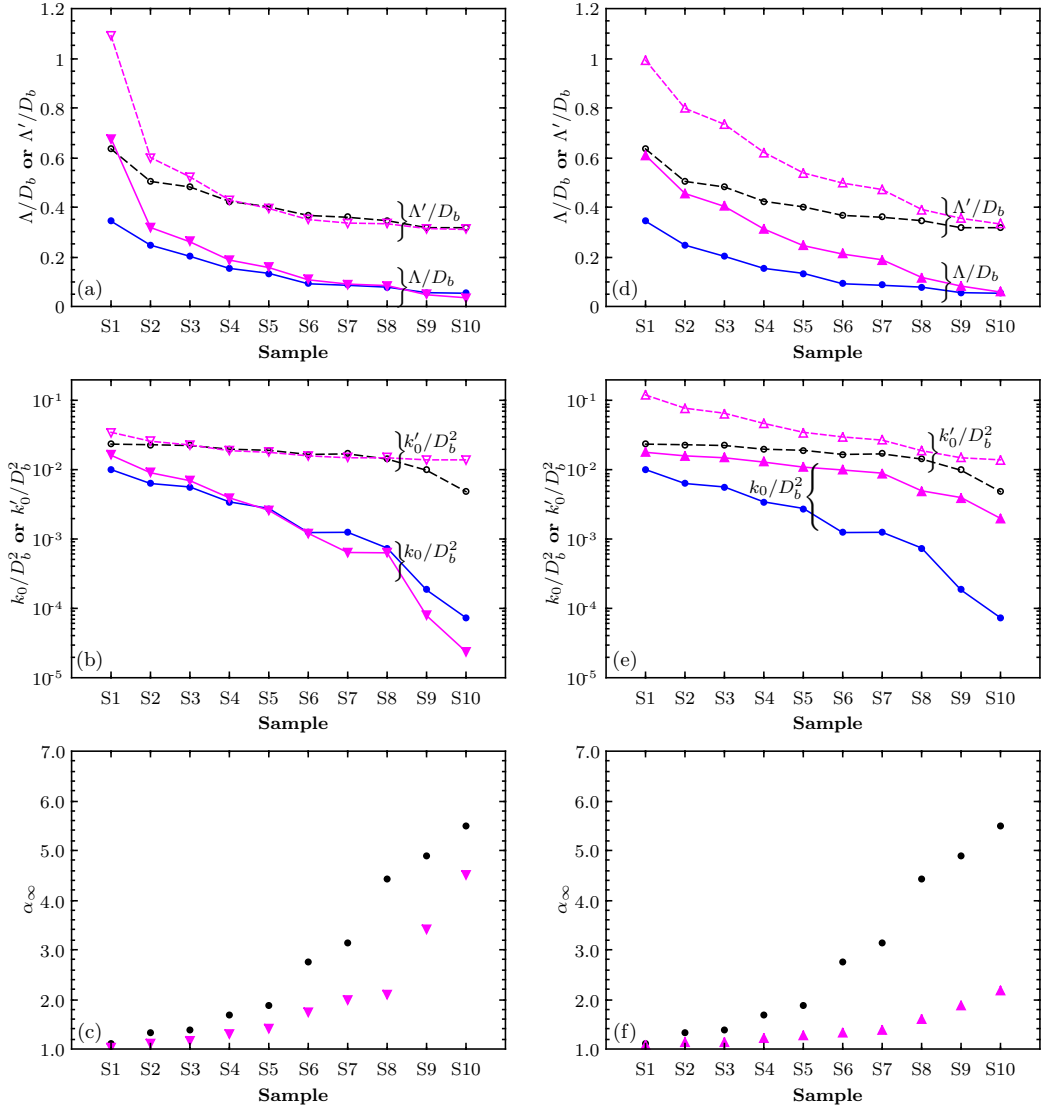


Figure III.13: Comparison of the dimensionless transports predictions obtained for PUC computations and: the HP method (a, b and c), or the DAD method (d, e and f). The results are shown for: PUC computation values (\circ), HP values (∇), and DAD values (\triangle). Note that the samples S1 to S10 are ordered by increasing mean closure rate, $\langle r_c \rangle$.

could be slightly higher in the extremity than in the bulk of the foam samples.

Thus, it appears clearly that these models taking into account both the amount of closed window and the closure rate give quite good estimates of macroscopic parameters. What about the simplest models taking into account one microstructural descriptor among two of them? Two “1-parameter” models are considered in the following: (i) the Hoang and Perrot’s model (HP) built by considering fully open foam with an uniform membrane closure rate tuned in such manner that the computed permeability is equal to the characterized one^[166,167] (it could include closed windows, i.e., squared ones), (ii) the semi-empirical model

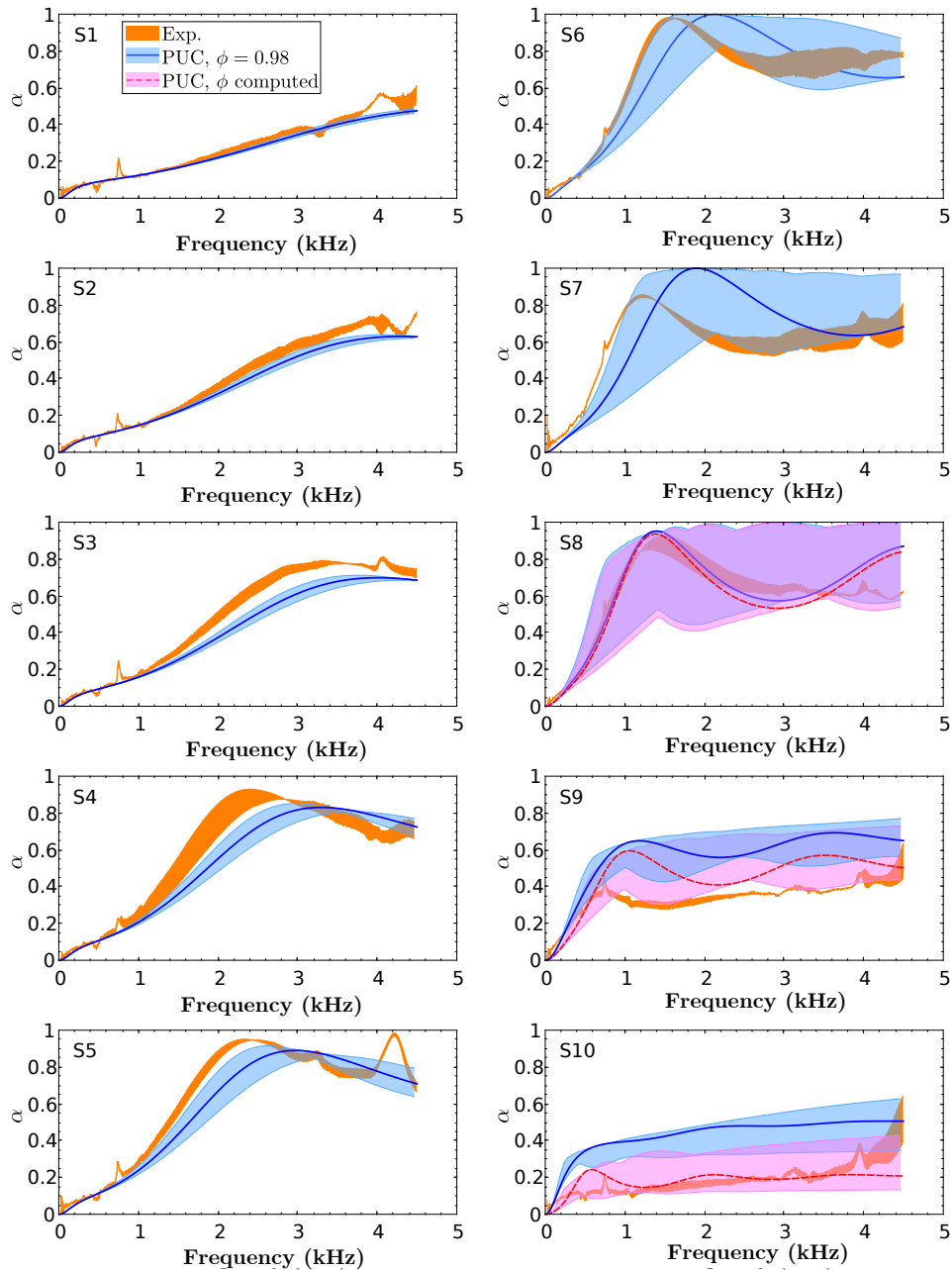


Figure III.14: Sound absorption coefficients of samples: experiments (orange filled zone), PUC computations with $\phi = 0.98$ (blue filled zone with full line), PUC computations with $\phi = \phi_{o,computed}$ (red filled zone with dashed line). The results are shown from top to bottom as: foams S1 to S5 (left panels), and foams S6 to S10 (right panels). The curves are calculated by using the computed macroscopic parameters shown in Fig. III.12, and their uncertainty are related to the estimation of errors on macroscopic parameters calculated by considering an error on the characterization of $\langle r_{c,o} \rangle$ equal to ± 0.05 .

of Doutres et al. which considers the fraction of closed windows without taking into account the closure rate of open windows^[27,79]. Fig.III.13 allows the predictions of these “1- parameter” models at constant pore size to be compared with those of the model presented in this paper. Apart from k_0 which is an input parameter taken from experiments, the macroscopic parameters values calculated with the HP model are globally close to our “2-parameter” PUC model. However, the viscous and thermal length, Λ and Λ' , for foams having a low fraction of closed windows (e.g., S1) are not well estimated. For a relatively low mean closure rate, $\langle r_c \rangle$ (i.e., S1, $\langle r_c \rangle = 0.33$), ignoring the presence of closed windows and considering that the system can be described by membranes at the periphery of open windows instead, could lead to an overestimation of the viscous and thermal characteristic lengths by a factor of two. The DAD model was developed on the standpoint of a cellular morphology which differ significantly from the one studied here, Fig. 13 (right pannel). Therefore, it can not be used to predict the transport parameters of a cellular structure exhibiting both partially open and closed windows in a given proportion. Concerning the SAC predictions of our computational method, Fig. III.14 shows that the global trend of experiments is well reproduced by our calculation method. However, a systematic difference between experiments and PUC computations is observed: it is as if the PUC computed curve was associated to materials having a closure rate slightly lower than that of the corresponding real foam. The discrepancy could be due to both a systematic error in the PUC calculation (as expected for the porosity, but also for the tortuosity) and a bias in the microstructural characterization as described before.

Thus, it appears necessary to take into account both the fraction of open windows and the window aperture rate to get an accurate estimation of macroscopic parameters and sound absorption coefficient. This result is in agreement with the fact that for at least two parameters, the thermal characteristic length Λ' and the static viscous permeability k_0 , their physical modelings require to consider both the fraction of open windows and the window aperture size. Indeed, by considering the idealized geometry of the considered foam skeleton, the thermal length, Λ' , can be fully calculated. The detail of the calculation is given in Appendix A for our idealized Kelvin cell. By neglecting a term due to the thickness of the ligaments (which is very low when $\phi \approx 1$), the thermal characteristic length is given by:

$$\frac{1}{\Lambda'} \approx \frac{1}{\Lambda'_{fo}} \frac{\phi_{fo}}{\phi_o} + \frac{7}{8\phi_o} \frac{2x_{fc}^{sq} + 3\sqrt{3}x_{fc}^{he} + (2x_p^{sq} + 3\sqrt{3}x_p^{he})(2r_{c,o} - r_{c,o}^2)}{D_b}, \quad (\text{III.16})$$

where Λ'_{fo} and ϕ_{fo} are respectively the thermal characteristic length and the porosity of the fully open foam (without membrane), and ϕ_o the open porosity. The previous expression shows clearly that the thermal length depends on both the fraction of open windows and the window aperture rate. Alternatively, in the framework of the characterization of partially reticulated foam samples, Λ' can be related to the thermal length, Λ'_{fc} , associated to a fully closed foam, as follows:

$$\frac{1}{\Lambda'} = \frac{1}{\Lambda'_{fc}} \frac{\phi_{fc}}{\phi_o} - \frac{2\langle A_o \rangle N_v}{\phi_o D_b^3}, \quad (\text{III.17})$$

where ϕ_o corresponds to the open porosity, and $\langle A_o \rangle$ is the mean window aperture area.

The mean window aperture area depends on the aperture window size distribution which can be evaluated from the closure rate distribution. The value of the thermal length of a fully closed foam, Λ'_{fc} appears as the lower bound of the thermal characteristic length. For a real foam, the ratio volume/surface is close to $D_b/(5.3\sqrt[3]{2})$, leading to $\Lambda'_{fc}/D_b \approx 0.3/\phi$.

We consider now the other parameter for which a “2-parameter” modeling is required. A model of effective medium for foam permeability, recently established^[177], predicts that the foam permeability, k_0 , depends on both the amount of closed windows and the membrane aperture size. This foam permeability can be estimated by the following equations:

$$k_0 = R_{op}\sigma_w k', \quad (\text{III.18a})$$

$$\frac{2}{N_v k'} = \sum_i \frac{x'_i}{k_i + \left(\frac{N_v}{2} - 1\right) k'}, \quad (\text{III.18b})$$

where σ_w is a coefficient ranging between 3 and 4, $k_i = r_{0,i}^3/3D_b$ is a local permeability associated with an open window having an aperture radius equal to $r_{0,i}$, and x'_i is the fraction of windows inside the open pore space calculated by including closed windows. Note that the closed windows have a local permeability equal to 0 and a proportion given by $1 - \sum_{i,k_i \neq 0} x'_i$. Eq. (III.18b) is solved iteratively. Approximated formula allowing us to estimate the fraction of open porosity R_{op} , the open window fraction within the open pore-space x'_i by measuring the open window fraction and the average number of neighbor pores are given in Ref.^[177]. The size of aperture d_i is calculated from the characterized closure rates $r_{c,i}$ and the mean size of bubbles D_b : $d_i = (1 - r_{c,i}) \langle t_w/D_b \rangle D_b$. The ratio $\langle t_w/D_b \rangle$ is assumed to be given by Kelvin cell structure: $(\frac{8}{14}\sqrt{3}L + \frac{6}{14}L)/2\sqrt{2}L \approx 0.54$. Moreover, closure rate distributions shown in Fig. III.4 allow to calculate the fraction x_i of walls having an aperture size equal to d_i . Fig. III.12 shows that the EM model predictions are in good agreement with experimental measurements and PUC computed values.

III.4 Conclusion

This paper investigates, both numerically and experimentally, the capability of millifluidic techniques to obtain light-weight cellular foams with tailored acoustical properties. The simple and yet versatile elaboration route proposed in this study consists in modifying the mass concentration of the polymeric solution, and it was shown that this approach allows bio-based solid cellular foams with controlled pore size and tuned membrane level to be obtained. The foam samples thus produced exhibit monodisperse pores with an assembly of closed and open windows, characterized by an appropriate aperture ratio. The dependence of the transport and sound absorbing properties on the membrane content was demonstrated. In particular,

samples with increased sound absorption properties (visco-thermal losses) were successfully manufactured. These experimental evidences are further supported by computational results, in which the transport properties are predicted by combining multiscale simulations with an averaging procedure. The latter involves all independent configurations of the membrane content, identified using the experimental distribution. These results confirm the relevance of the elaboration strategy to produce raw materials with optimal sound proofing capabilities.

Acknowledgments

This work was part of a project supported by ANRT (Grants No. ANR-13-RMNP-0003-01 and No. ANR-13-RMNP-0003-03). The work of V. H. Trinh was supported by a fellowship awarded by the Government of Vietnam (Project 911).

Appendix

III.A. Reconstruction of periodic unit cell

In this appendix, we reconstruct a periodic unit cell based on the Kelvin pattern. A part of the $1/96$ periodic unit cell is approximated as $1/4$ triangular tube and $1/8$ octahedron placed at their junction of node (see Fig. III.15). The coordinates of 7 vertices of this skeleton can be expressed as follows: $A(0, r/2\tan\beta, 0)$, $B(r/2, 0, 0)$, $C(0, -r/2\tan\beta, 0)$; $F(r/2, 0, -r/2)$, $J(r/2+L_l\sqrt{2}/4, -L_l\sqrt{2}/4, 0)$, $K(L_l\sqrt{2}/4, -L_s\sqrt{2}/4, 0)$ and $M(r/2+L_l\sqrt{2}/4, -L_l\sqrt{2}/4, -r/2)$; in which, $\tan\alpha = \sqrt{3}/(\sqrt{3} - \sqrt{2})$, $\beta = 3\pi/4 - \alpha$, $L_l = (D_b/4 - r/2)\sqrt{2}$, and $L_s = [D_b/4 - r/2(\sqrt{6} - 1)]\sqrt{2}$.

The total solid volume over the overall unit cell is the volume of 12 nodes and 24 ligaments (12 edges on hexagonal faces and 24 edges shared with the neighboring cells), given by

$$V_s = 96 \times (V_{ABFJKM} + V_{ABCF}) = 6\sqrt{3}Lr^2 + (4\tan\beta - 6 - \sqrt{6})r^3. \quad (\text{III.A.1})$$

The porosity of the open cell structure can be defined as,

$$\phi = 1 - \frac{3\sqrt{6}}{16} \left(\frac{r}{L}\right)^2 - \frac{4\tan\beta - 6 - \sqrt{6}}{16\sqrt{2}} \left(\frac{r}{L}\right)^3. \quad (\text{III.A.2})$$

Solving Eq. (III.A.2), the ligament size r/L as a function of porosity ϕ is then given by,

$$\frac{r}{L} = \frac{P_2}{3P_3} \left[1 - \cos \frac{\arccos(\chi) - 2\pi}{3} \right], \quad (\text{III.A.3})$$

where $\chi = (P_2^3 - 27P_3P_0)/(2\sqrt{P_2^3})$ with

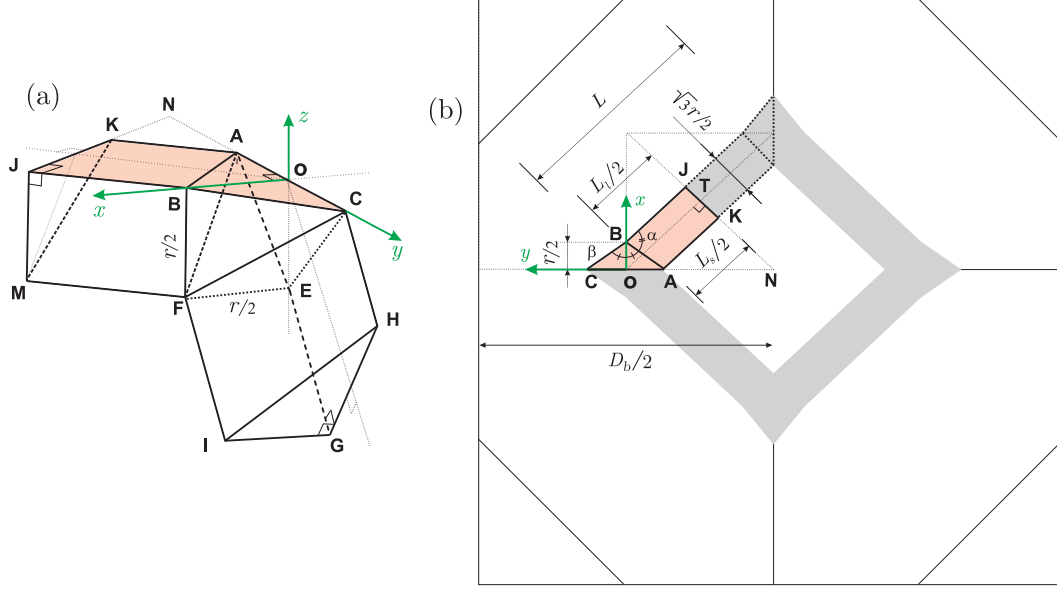


Figure III.15: (a) Detail of the coordinates of the basic vertex in the 1/48th open unit cell having ligaments of equilateral triangular cross-section of edge size r and length of L . (b) Diagram as a top view of the skeleton showing the relations between the angular and length parameters at the node and several ligaments.

$$P_0 = 1 - \phi, \quad P_2 = \frac{3\sqrt{6}}{16}, \quad P_3 = \frac{4\tan\beta - 6 - \sqrt{6}}{16\sqrt{2}}.$$

Finally, we obtain an approximate expression for Eq. (III.A.3) which reads

$$C_r := r/D_b = 0.5833(1 - \phi)^{0.521}. \quad (\text{III.A.4})$$

In the case of a fully open unit cell, the thermal characteristic length can be estimated as $\Lambda'_{fo} = 2\phi/S_p$, in which the specific surface area S_p is defined as the total solid surface area per unit volume,

$$S_p = \frac{96 \times (S_{BFMJ} + S_{AFMK} + S_{BCF})}{D_b^3}. \quad (\text{III.A.5})$$

Therefore, one gets

$$\frac{\Lambda'_{fo}}{D_b} = \frac{\phi}{3 \left[(2/\cos\beta - 4\sqrt{3} - 2\sqrt{2})C_r^2 + 3\sqrt{2}C_r \right]}. \quad (\text{III.A.6})$$

By neglecting the volume of membranes where thicknesses are in the order of $1 \mu\text{m}$, the thermal characteristic length Λ' of a unit cell containing membranes can be obtained by considering the specific surface of membranes S_m ,

$$\Lambda' = \frac{2\phi}{S_p + S_m} = \frac{1}{1/\Lambda'_{fo} + (S_m^{sq} + S_m^{he})/2\phi}, \quad (\text{III.A.7})$$

where

$$S_m^{sq} = \frac{\sum_{i=1}^6 [2r_{ci} - r_{ci}^2 - 4\sqrt{6}C_r + 4(7 - 2\sqrt{6})C_r^2]}{4D_b}, \quad (\text{III.A.8a})$$

$$S_m^{he} = \frac{3\sqrt{3}\sum_{i=1}^8 [2r_{ci} - r_{ci}^2 - 4C_r + 4C_r^2]}{8D_b}. \quad (\text{III.A.8b})$$

Noted that, for the fully closed faces, their closing rates are close to 1, and considering all partially closed faces have an identical rate r_c , the above factor S_m is estimated as following,

$$S_m = \frac{\frac{2N_{fc}^{sq} + 3\sqrt{3}N_{fc}^{he}}{8} + \frac{2N_p^{sq} + 3\sqrt{3}N_p^{he}}{8}(2r_c - r_c^2) - 6(\sqrt{6} - 1 + 2\sqrt{2})C_r + [42 - 12\sqrt{3}(\sqrt{2} - 1)]C_r^2}{D_b}. \quad (\text{III.A.9})$$

III.B. Global calculation of equivalent configurations

We consider the response of a system defined in Sec. 3.1. Specifically, we wish to show that, for the particular case at hand in which the reconstruction of real foams is addressed by means of both the number of closed windows and the size of window aperture, a drastic reduction of the number of calculations to be considered can be obtained. This calculation is carried out in an iterative way and consists of browsing the graph of linked configurations with the aim to define a set of equivalent configuration, Fig. III.11b. At the beginning of the iterative process, the first line of the table found at the end of the step III is used as a starting equivalent configurations list. All configurations associated to the configurations from the starting list are added to it to build a new list of equivalent configurations. This list becomes the starting list in the iterative process. As previously, this list is used to build a new list, etc. The process is repeated until the starting list and the recalculated list are equal. At the end of the iterative process, the branch of configurations equivalent to the first one is identified. Then, the calculation is repeated with a line which has still not been visited. When all configurations have been visited, the calculation is finished. The major steps of equivalent configurations calculation is summarized in Fig. III.11. Thanks to this calculation of equivalent configurations, the number of reference configurations, \mathcal{N}_r , we have to compute is drastically reduced compared to the total number of configurations, \mathcal{N}_t (Table III.4).

Chapter IV

Permeability of solid foam: Effect of pore connections

Preface

- **Authors and establishments:**

- **Vincent LANGLOIS**, Ph.D. doctor, Université Paris-Est, Laboratoire Géomatériaux et Environnement, LGE EA 4508, 77454 Marne-La-Vallée, France.
- **Van Hai TRINH**, Ph.D. student, Université Paris-Est, Laboratoire Modélisation et Simulation Multi Echelle, MSME UMR 8208 CNRS, 77454 Marne-La-Vallée, France.
- **Christelle LUSSO**, Ph.D. doctor, Université Paris-Est, Laboratoire Navier, NAVIER UMR 8205 CNRS, 77454 Marne-La-Vallée, France.
- **Camille PERROT**, Associate professor, Université Paris-Est, Laboratoire Modélisation et Simulation Multi Echelle, MSME UMR 8208 CNRS, 77454 Marne-La-Vallée, France.
- **Xavier CHATEAU**, Ph.D. doctor, Université Paris-Est, Laboratoire Navier, NAVIER UMR 8205 CNRS, 77454 Marne-La-Vallée, France.
- **Yacine KHIDAS**, Ph.D. doctor, Université Paris-Est, Laboratoire Navier, NAVIER UMR 8205 CNRS, 77454 Marne-La-Vallée, France.
- **Olivier PITOIS**, Ph.D. doctor, Université Paris-Est, Laboratoire Navier, NAVIER UMR 8205 CNRS, 77454 Marne-La-Vallée, France.

- **State of publication:**

- Journal: Physical Review E **97**(5), 053111.

– Submitted date: 21 December 2017. Published date: 31 May 2018.

- **Contribution of the paper:**

Permeability is one of the most physical macroscopic material properties of interest used to understand the behavior of porous media. The present paper proposes a systematic approach to characterize the permeability of membrane foam-based materials. In one stage, a series of highly porous material is elaborated with a range of membrane levels in wall cell shaping. In the second stage, based on the observed morphological property, several numerical simulations at both local and global scale are performed for material permeability characterization. Comparisons between computational results in different method show a good agreement and indicate that the proposed method is effective and robust.

- **V. H. Trinh's contributions:** V. H. T. performed the numerical work at the pore scale and participated in writing the manuscript.

Permeability of solid foam: Effect of pore connections

V. Langlois^{1,†}, V. H. Trinh^{2,3,‡}, C. Lusso^{4,§}, C. Perrot^{2,¶},
X. Chateau^{4,†}, Y. Khidas^{4,‡}, and O. Pitois^{4,§}

¹⁾ Université Paris-Est, Laboratoire Géomatériaux et Environnement, LGE EA 4508, 77454 Marne-la-Vallée, France, [†]vincent.langlois@u-pem.fr.

²⁾ Université Paris-Est, Laboratoire Modélisation et Simulation Multi Echelle, MSME UMR 8208 CNRS, 77454 Marne-la-Vallée, France, [‡]van-hai.trinh,[¶]camille.perrot}@u-pem.fr.

³⁾ Le Quy Don Technical University, Hanoi, Vietnam.

⁴⁾ Université Paris-Est, Laboratoire Navier, NAVIER UMR 8205 CNRS, 77454 Marne-la-Vallée, France, [§]christelle.lusso@onera.fr, [†]xavier.chateau,[‡]yacine.khidas}@u-pem.fr, [§]olivier.pitois@ifsttar.fr.

Abstract

In this paper, we study how the permeability of solid foams is modified by the presence of membranes that close partially or totally the cell windows connecting neighboring pores. The finite element method (FEM) simulations computing the Stokes problem are performed at both pore and macroscopic scales. For foam with fully interconnected pores, we obtain a robust power-law relationship between permeability and aperture size. This result is due to the local pressure drop mechanism through the aperture as described by Sampson for fluid flow through a circular orifice in a thin plate. Based on this local law, pore-network simulation of simple flow is used and is shown to reproduce FEM results. Then, this low computational cost method is used to study in detail the effect of an open window fraction on the percolation properties of the foam pore space. The results clarify the effect of membranes on foam permeability. Finally, Kirkpatrick's model is adapted to provide analytical expressions that allow for our simulation results to be successfully reproduced.

DOI: [10.1103/PhysRevE.97.053111](https://doi.org/10.1103/PhysRevE.97.053111)

IV.1 Introduction

Foam is dispersion of gas in liquid or solid matrix. Its structure is made of membranes (also called films or liquid foams), ligaments or Plateau's borders, (junction of three membranes) and vertices or nodes (junction of four ligaments). Whereas closed membranes are necessary to ensure the mechanical stability of liquid foam^[31], membranes can be open or totally absent in solid foams, allowing for the foam cells (pores) to be connected through windows. It is remarkable that such a small volume contained in the window areas can have such drastic effects for several properties of foams. This is the case for fluid permeability of solid foam, where open windows contribute to transport the fluid through the material, whereas closed windows stop it. Therefore, the fraction of closed windows is crucial for several applications, such as filtering. As viscous dissipation is the most dissipative mechanism in sound propagation through porous materials, permeability (or flow resistivity) is a key parameter in this issue^[9,12], making acoustical properties of foams very sensitive to both the open window fraction and the aperture of windows. Different works have focused on the effects of foams geometry on permeability: fraction of closed windows^[27], aperture of windows^[130], and solid volume fraction and ligament shapes^[178,179]. Authors have proposed empirical relations between permeability and several structural parameters of foam (solid volume fraction, window aperture rate, etc.), but a global physical model would be suitable in order to design foams with the required permeability. Note also that, beyond a critical value of open window fraction (called the percolation threshold), the percolation phenomenon is expected to arise in foams, i.e., the size of the largest cluster of inter-connected cells is equal to the sample height, H_{sp} , leading to an open pore space^[180]. This phenomenon has not been studied so far in the case of foams, although it has been proved to have a great influence on permeability of porous media. For example, the classical Kozeny-Carman equation has to be modified by considering the difference between the porosity and the critical porosity leading to percolation^[181]. Tackling the percolation issue for the permeability of porous media requires numerical simulations to use large samples involving a few thousand pores^[182]. For the flow simulation at the pore scale or at the scale of a few pores, the finite element, finite volume, boundary element, and lattice Boltzmann methods have been often applied^[9,183–185]. However, as the size of samples increases, the computational costs for those methods become prohibitive, so that multi-scale approaches are preferable^[186–191]. Such methods involve determining the flow behavior at the local scale (i.e., a throat between two linked pores) by numerical simulations or analytical solutions (e.g. Hagen-Poiseuille equation); then, pore-network simulations are performed to determine the permeability at the macroscopic scale^[192].

In this paper, we use a multi-scale approach to study the permeability of solid foam with various windows configurations. The effect of aperture size on local permeability of fully open-cell foam (i.e., containing no closed window) is studied by using FEM simulations on

periodic unit cells (PUCs) with the Kelvin partition of space. The effect of closed windows is studied through FEM simulations on larger samples (containing 256 pores). Then, mesoscopic effects induced by the structure of the pore network are studied by pore-network simulations on large (containing at least 43900 pores) networks of interconnected pores interacting via local permeabilities. Finally, a model of effective permeability, based on a calculation of the mean local permeability as in Kirkpatrick^[186], is used to provide a physical description of the membrane-induced percolation effect in foam and the effect of combining several local permeabilities.

IV.2 Numerical simulations of foam permeability

IV.2.1 FEM simulations of fluid flow

At the pore scale:

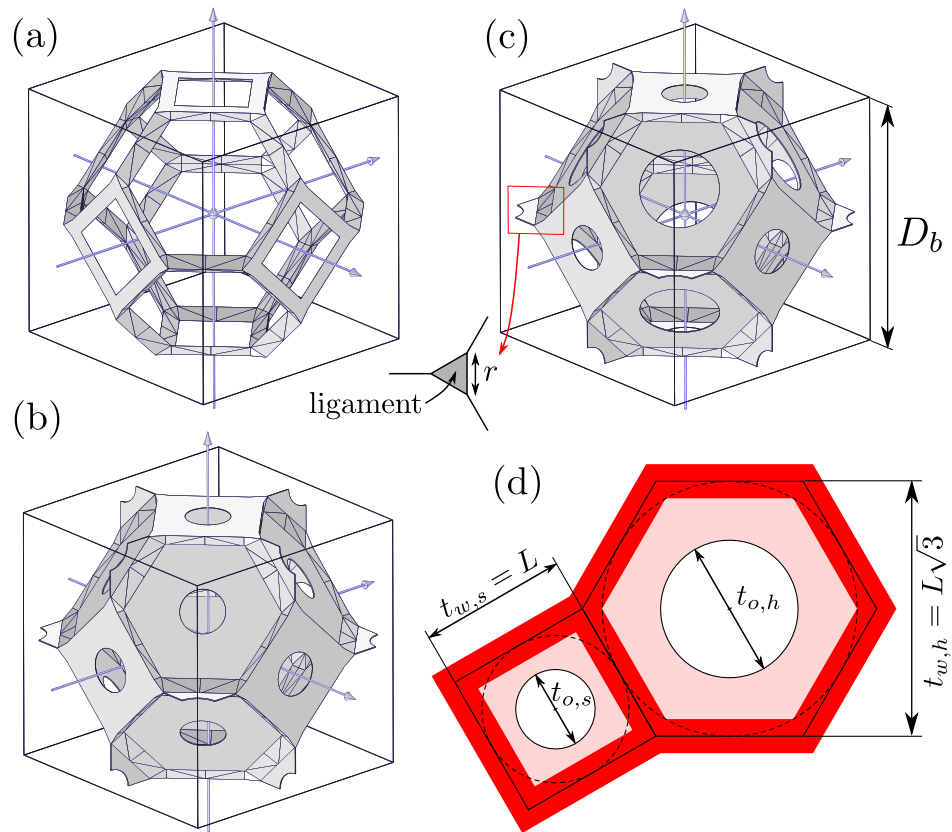


Figure IV.1: PUC with fully open windows (a), with partially closed windows by the same aperture size (b), identical aperture rate (c), definitions of the aperture size t_o and the window size t_w (d).

As shown on Figure IV.1, a periodic unit cell of size D_b is used to represent the pore

structure in foam samples^[25]. The number of pores, N_p , contained within the unit cell is equal to 2. The cell is based on the Kelvin paving and is a 14-sided polyhedron (eight hexagons and six squares) corresponding to windows shared with the $N_v = 14$ neighbors. The cell skeleton is made of idealized ligaments having length $L = D_b/(2\sqrt{2})$ and an equilateral triangular cross section of edge side $r = 0.58D_b(1 - \phi)^{0.521}$, where ϕ is the gas volume fraction^[31]. As we are interested in the effect of partial closure of the cell walls, we partially close the windows by adding holed membranes characterized with distinct circular aperture sizes. Two kinds of simulations have been performed: (1) identical aperture size on all windows [Figure IV.1(b)] and (2) identical rate of aperture $\delta_{ow} = t_o/t_w$ [Figure IV.1(c)] where t_w and t_o are, respectively, the full window size and the size of the aperture as defined in Figure IV.1(d). Note that, in the reference configuration [Figure IV.1(a)], the 14 cell windows are fully open (i.e., contain no membrane). The static viscous permeability K is computed from the solution of the Stokes problem^[180] for different porosities. The boundary value problem is solved by using the finite element method and the commercial software COMSOL Multiphysics. The permeability calculation error, determined by convergence tests, is inferior to 6%. To achieve this accuracy, the meshes contain at least 250 000 tetrahedral elements.

At the macroscopic scale:

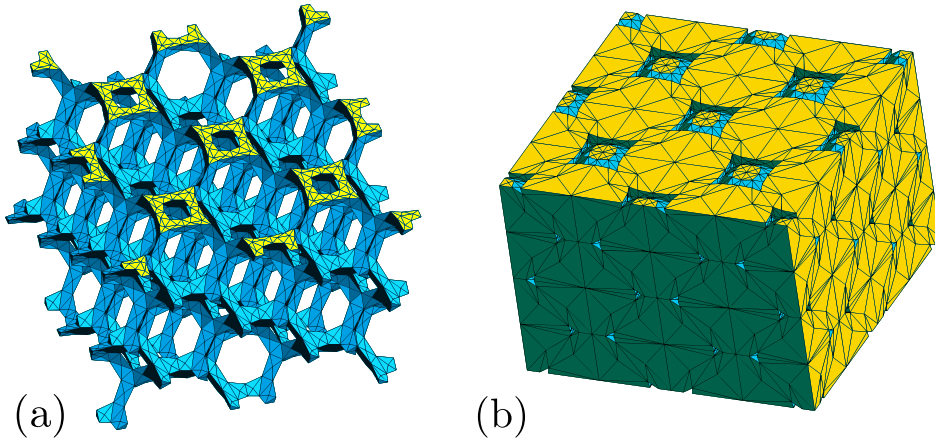


Figure IV.2: FEM macro-scale samples: skeleton mesh (a) and porosity mesh (b). For sake of visibility, a mesh of size $2\sqrt{2} \times 2\sqrt{2} \times 2$ (D_b units) is depicted.

In order to study the flow properties on a larger scale, we have performed numerical simulation for the flow of a Newtonian fluid through a periodic network of Kelvins cells having a size $L \times L \times H_{sp} = 4\sqrt{2} \times 4\sqrt{2} \times 4$ in D_b units (i.e., $N_p = 256$ pores), and a porosity ϕ equal to 0.9. Figure IV.2 shows an open cell foam sample made of 32 pores (i.e., all the windows between adjacent cells are open). The macroscopic intrinsic permeability is computed from the averaging of the solution of the Stokes problem set on the foam sample. In this study, the cell windows are either closed or open with random spatial distribution over the foam

sample. The fraction of open windows is $x_{ow} = N_{ow}/(N_p \times N_v/2)$, where N_{ow} is the number of open windows. For each value x_{ow} , the macroscopic intrinsic permeability is the average of numerical simulations for six different samples obtained from six draws of closed window positions. The resolution of the boundary value problem is achieved through the Finite Element Method using FreeFem++ software^[193]. The typical discrete problem contains 1 400 000 tetrahedra and 8 000 000 degrees of freedom and is solved using a Message Passing Interface on four processors. We compared the permeability computed with the finest mesh (1 400 000 tetrahedra) to the permeability computed using a coarser one (700 000 tetrahedra). As the difference is less than 3%, which is small compared to the window closure included permeability variations, we concluded that the meshes we use are fine enough for accurate results.

IV.2.2 Pore-network simulations

Effects of pore network features on permeability are studied on several lattices having different numbers of neighbor pores N_v (Figure IV.3). Concerning foams, the cases $N_v = 14$ and $N_v = 8$ are of specific interest: $N_v = 14$ corresponds to Kelvin's structure, which is very similar to real foam's structure^[31], and $N_v = 8$ corresponds BCC structure, or to Kelvin's structure with smallest windows (square windows) being closed as expected for a small fraction of gas ϕ . For $N_v = 14$ and $N_v = 8$, the samples have a size $L^2 \times H_{sp} = 28^3$ (D_b units) and contain 43904 pores. For $N_v = 6$ and $N_v = 20$, the the samples contain at least 46000 pores. Boundary effects are avoided by resorting to periodic conditions imposed in the directions perpendicular to the macroscopic flow. In this simple model, we consider, for each pore, a unique value of pressure without calculating the functions of pressure and fluid velocity inside the pore. At the local scale, the flow rate $q_{j \rightarrow i}$ from pore j to pore i is governed by the differential pressure between the pores $\Delta P_{ij} = P_j - P_i$, $q_{j \rightarrow i} = \frac{D_b}{\mu} k_{ij} \Delta P_{ij}$, where the coefficient k_{ij} is the local permeability between the pores i and j , and μ is the fluid dynamic viscosity.

At steady state and by considering incompressible fluid, the volume of fluid inside pore i is constant and the sum of flow rates coming from neighbor bubbles is equal to zero, leading to: $\sum_{j=1}^{N_v} k_{ij}(P_j - P_i) = 0$. To generate a flow through the sample, a pressure difference is imposed between top and bottom faces of the sample ($P_{top} = \Delta P_{sp}$, $P_{bot} = 0$). By considering these boundary conditions, this previous equation can take a matrix form:

$$\bar{K}[P_i] = [S_i], \quad (\text{IV.1})$$

where $[P_i]$ is a vector containing the pressure of inner pores (pores located on the top and bottom faces are excluded); \bar{K} is the matrix defined from local permeabilities ($-\sum k_{ij}$ along the diagonal and k_{ij} elsewhere); and $[S_i]$ is a vector containing zeros except for inner pores having top pores as neighbors where $S_i = -\sum_{j_{top}} k_{ij_{top}} \Delta P_{sp}$.

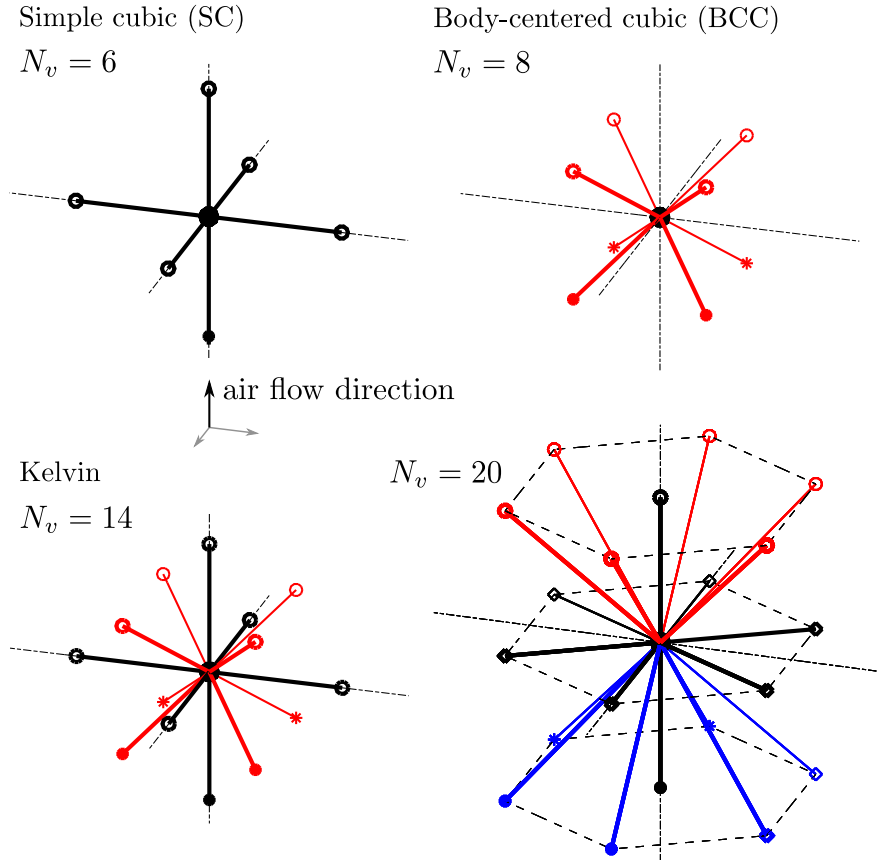


Figure IV.3: Network structures used in pore-network simulations.

As soon as the pore network links top to bottom and by considering only the interconnected pores \bar{K} can be inverted and the fluid pressure in each pore can be calculated from Eq. (IV.1). Alternatively, in the case of memory limitations during computer calculations, fluid pressure can be calculated in an iterative way as in Ref^[186]. In any way, the macroscopic flow Q and the macro permeability K can be calculated as

$$Q = \sum_{i_{bot}} \sum_{j_v} q_{j_v \rightarrow i_{bot}} = \frac{D_b}{\mu} \sum_{i_{bot}, j_{vi}} k_{i_{bot}, j_{vi}} \Delta P_{i_{bot}, j_{vi}} \quad (\text{IV.2a})$$

$$K = \mu Q H_{sp} / L^2 \Delta P_{sp} \quad (\text{IV.2b})$$

Different materials having different kinds of local permeability distribution have been studied: two local permeabilities (binary mixture), a local permeability mixed with zero permeability (i.e., closed window), and two local permeabilities mixed with closed windows. For each kind of local permeability distribution, calculations are repeated 100 times on different random draws in order to calculate an average. For each random draw, local permeabilities are randomly distributed over the network.

To reduce errors induced by size effects in the calculation of percolation threshold and

open porosity (defined as the volume fraction of pores occupied by percolating fluid)^[182], additional numerical simulations were performed on large samples such as $N_p \sim 10^6$ pores.

IV.3 Results and discussion

IV.3.1 Effect of the aperture size

FEM simulations on PUCs at the pore scale for various aperture sizes reveal a power-law relationship between permeability and aperture size [Figure IV.4(a)]. Similarly the numerical results for the dimensionless permeability of porous materials with same aperture rate are well fitted by a power law when plotted in a $(\delta_{ow}, K/D_b^2)$ diagram [Figure IV.4(b)]. Note that, for high aperture rates, the aperture shape is no longer circular due to the fact that the apertures should overlap the ligaments, which is not allowed in our calculations. The condition of identical aperture rate is not observed. This artifact leads to an artificial permeability plateau corresponding to the “without membrane” permeability. Apart from this artifact, FEM results show that relationship between permeability and mean wall aperture is almost unaffected by the porosity (i.e., the width of ligaments).

This power-law relationship is in agreement with a local interpretation based on the pressure drop of the fluid passing through the wall aperture. Indeed, Sampson^[194] solves analytically the problem of the pressure drop ΔP occurring for an incompressible fluid flow passing through a circular hole of diameter d_o in a thin plate:

$$\frac{q}{\Delta P} = \frac{d_o^3}{24\mu}, \quad (\text{IV.3})$$

where q is the volume fluid flow rate passing through the hole.

This relation arises from the fact that, at low Reynolds number, the coefficient of fluid resistance $\zeta = 2\Delta P/(\rho V_o^2)$ is, in general, proportional to the inverse of Reynolds number $\text{Re} = V_o d_o \rho / \mu$ ^[195], where V_o is the mean stream velocity in the narrowest section of the orifice ($V_o = 4q/\pi d_o^2$).

After Ref.^[196], the pressure drop through a hole of circular shape is very close to the one obtained with a hole of squared shape having the same area. We can deduce that the Sampson formula can be extended to squared and hexagonal shape of aperture by taken into account an equivalent diameter $t_{o,eq}$ defined from the surface area of the aperture S_o : $t_{o,eq} = 2(S_o/\pi)^{0.5}$. By using such a definition for the aperture size and calculating a window average of the aperture size, we can plot all FEM results on a same graph. Figure IV.4(c) shows that all results, including the ones obtained without a membrane, follow the same trend. Therefore, due to the peculiar pore geometry of foams, the pressure drop inside such porous materials is governed by a local mechanism which is not described by the usual Hagen-Poiseuille equation as it is done in classical porous media^[187,189,191,192].

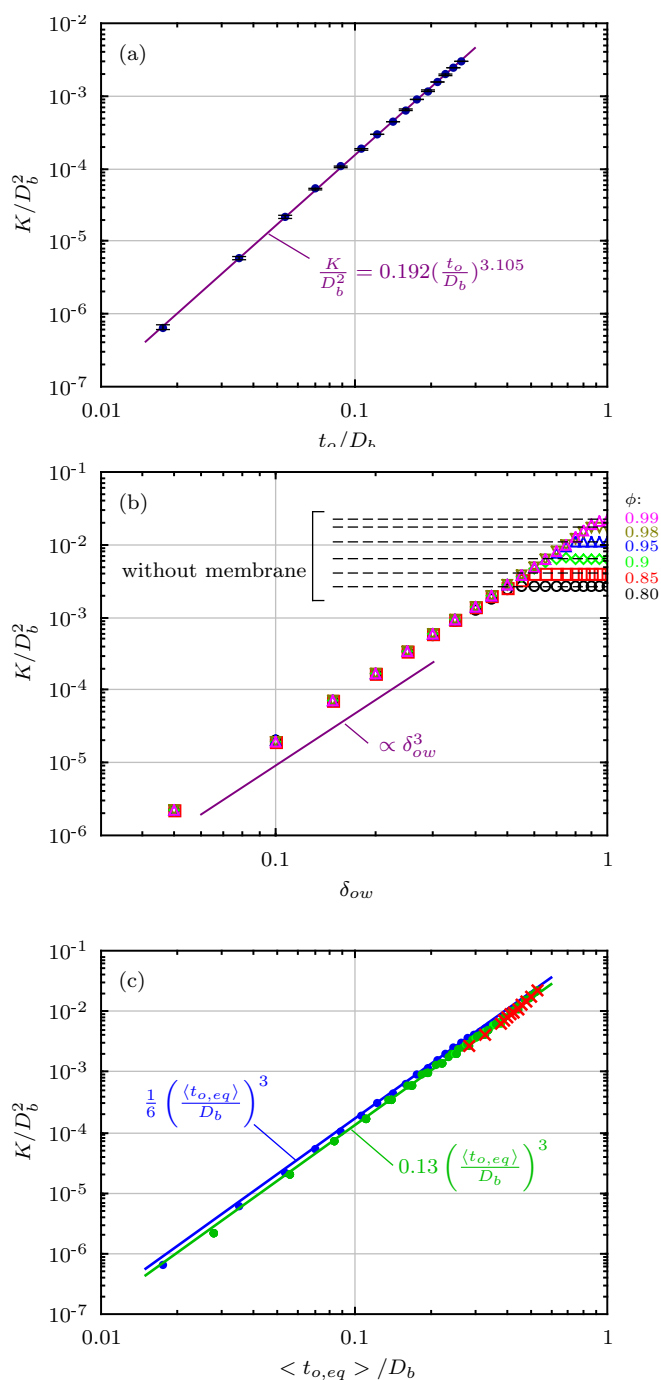


Figure IV.4: (a) FEM predictions at identical aperture size with $\phi = 0.98$, (b) FEM predictions at identical aperture rate for various ϕ , (c) permeability as a function of the mean wall apertures: FEM results (blue dot for identical aperture, green dot for identical rate, red cross for “no wall” foam with ϕ varying from 0.8 to 0.99), pore-network simulations with Sampson local permeabilities and $N_v = 14$ (blue line for identical aperture, green line for identical rate). Note that the mean wall aperture is calculated without including the four square windows, which are parallel to the macroscopic flow direction $\langle t_{o,eq} \rangle / D_b = (2t_{o,sq} + 8t_{o,hex}) / 10D_b$.

To check the ability of a pore-network model to predict the permeability, network calculations have been performed using local permeabilities given by a Sampson equation:

$$k = t_o^3/24D_b. \quad (\text{IV.4})$$

Note that in such simple simulated configurations (i.e., identical aperture size t_o or identical aperture rate δ_{ow}), the network problem shown in the previous section can be solved analytically. Therefore, macroscopic permeability is given by $K = 2k_{sq} + 2k_{hex}$, leading to $\frac{K}{D_b^2} = \frac{1}{6} \left(\frac{t_o}{D_b}\right)^3$ for identical aperture rate and $\frac{K}{D_b^2} = \frac{1+3^{1.5}}{12} \left(\frac{5}{1+48^{0.5}} \frac{\langle t_{o,eq} \rangle}{D_b}\right)^3 \approx 0.13 \left(\frac{\langle t_{o,eq} \rangle}{D_b}\right)^3$ for identical aperture rate. Figure IV.4(c) shows that network simulation results compare very well to FEM results. This good agreement supports both the interpretation of the permeability by using local permeabilities and the relevance of network simulations.

IV.3.2 Effect of closed windows: The bond percolation problem in foam

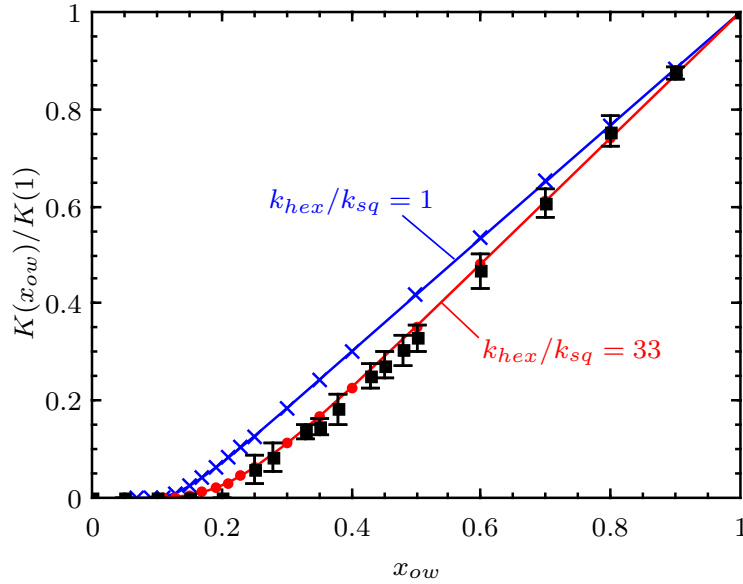


Figure IV.5: Dimensionless permeability $K(x_{ow})/K(1)$ as a function of the open window fraction x_{ow} for FEM simulation (black square) and pore-network simulations (blue cross and red dot) on samples mixing two local permeabilities with various ratios k_{hex}/k_{sq} and having a Kelvin structure ($N_v = 14$). Error bars are calculated using $(\text{maximal value} - \text{minimal value})/2$.

Figure IV.5 shows the permeabilities calculated by FEM simulations on large samples having random positions of closed windows and various open window fractions x_{ow} . For $x_{ow} > 0.3$, permeability exhibits a quasi-affine dependence on the open walls fraction x_{ow} . Below a critical concentration $x_{ow} < 0.2$, the fluid flow vanishes.

To check their capacity to reproduce the FEM results, pore-network simulations were performed by considering two local permeabilities, k_{hex} and k_{sq} , given by the Sampson equation and associated to squared and hexagonal windows as in Kelvin's structure ($N_v = 14$). For $\phi = 0.9$, the hexagonal-to-square aperture ratio in FEM simulations is close to 3.2. The ratio between local permeabilities is therefore close to $k_{hex}/k_{sq} = 33 (\approx 3.2^3)$. As shown in Figure IV.5 and considering the margin of error, network simulations and FEM simulations lead to the same results. Moreover, pore-network simulations reveal that the slope of the affine part of the function $K(x_{ow})$ depends on the ratio between local permeabilities.

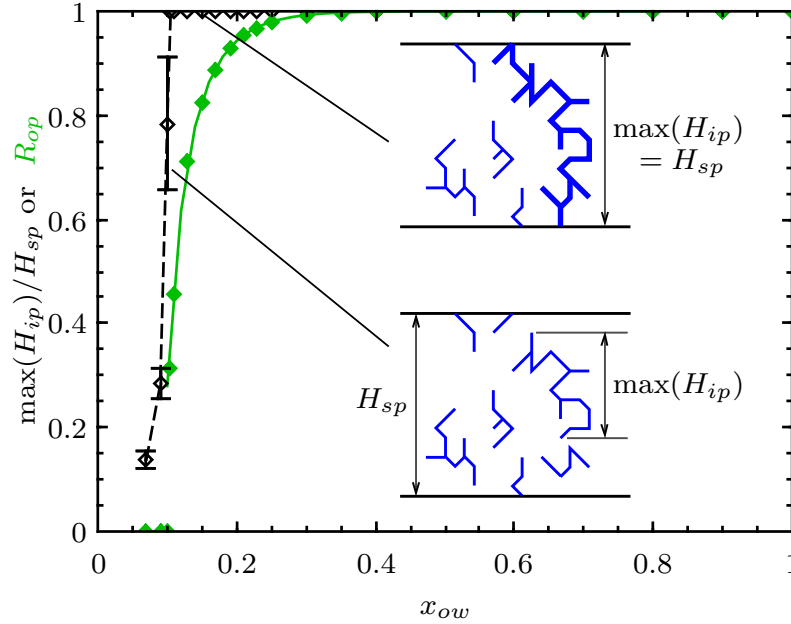


Figure IV.6: Pore-network simulations: Highest of the largest cluster of the interconnected pores (black diamond) and fraction of open porosity (green diamond) as a function of the open window fraction x_{ow} for $N_v = 14$ and large samples $N_p \sim 10^6$. Green line corresponds to fraction of open porosity calculated by using Eq. (IV.6a).

In reference to percolation theory^[186], solid foams are subjected to bond percolation for which bonds correspond to open windows. In such a percolation, pore-network simulations are helpful to calculate the maximal size of interconnected pores, the fraction of percolating porosity R_{op} (= number of pores within open pore space N'_p /total number of pores, N_p), and permeability^[186,197]. In the case $N_v = 14$, the maximal vertical extent (the mean direction of fluid flow is vertical) of interconnected pores, H_{ip} , is equal in average to the sample thickness H_{sp} for $x_{ow} > 0.1$, and percolation occurs (Figure IV.6). This fraction corresponds to the percolation threshold x_p , and it is close to $1.5/N_v$ for all lattices studied as in Ref.^[186]. Therefore, as the average number of open windows per pore is equal to $x_{ow}N_v$, at least 1.5 open windows per pore are required to allow fluid flow through porous foamy materials. With respect to the permeability (Figure IV.7), simulations performed with homogeneous

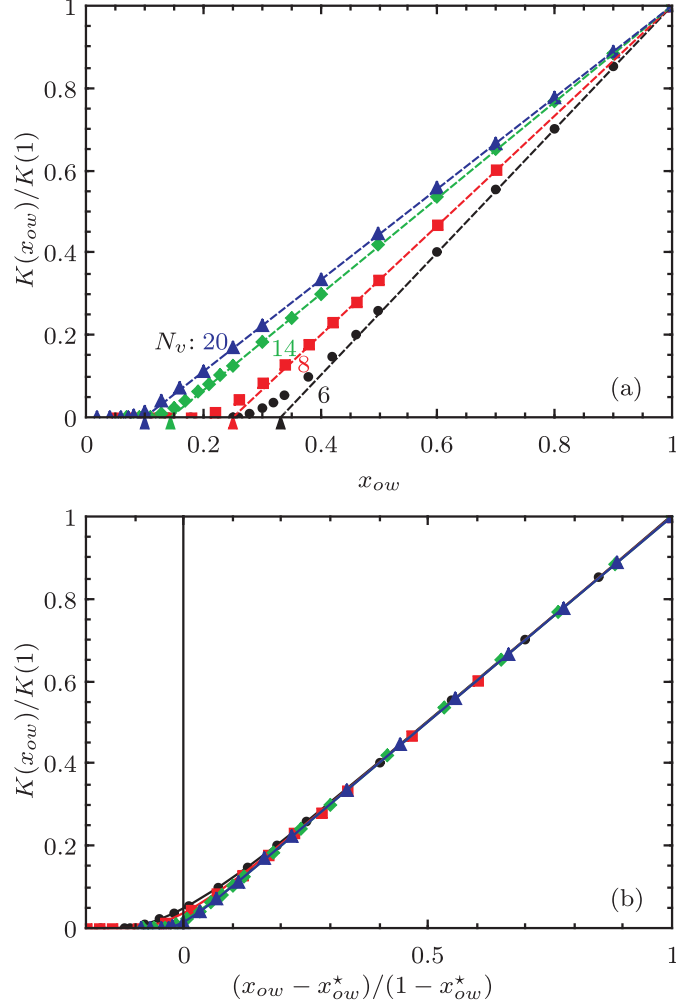


Figure IV.7: Pore-network simulations: (a) dimensionless permeability $K(x_{ow})/K(1)$ as a function of the open window fraction x_{ow} for various neighbor pore number N_v (arrows point to the abscissa $x_{ow} = x_{ow}^* = 2/N_v$); (b) the same data with another abscissa $(x_{ow} - x_{ow}^*)/(1 - x_{ow}^*)$.

local permeabilities show that the slope of the affine part of $K(x_{ow})$ depends on the number of neighbor pores N_v . The affine part of $K(x_{ow})$ intercepts the abscissa to a critical concentration given by $x_{ow}^* = 2/N_v$. Figure IV.7(b) shows that the ratio $K(x_{ow})/K(1)$ in porous material having homogeneous local permeability is linearly dependent on a single parameter $(x_{ow} - x_{ow}^*)/(1 - x_{ow}^*)$ except for open window fractions close to the percolation threshold.

A deeper analysis of our results makes it possible to study in detail the structure of the open-pore space and the one of fluid passing through it. Figure IV.8(b) shows that the fraction of open windows within open pore space, x'_{ow} is larger than global value x_{ow} . This additional amount of open window within open-pore space can explain the behavior of

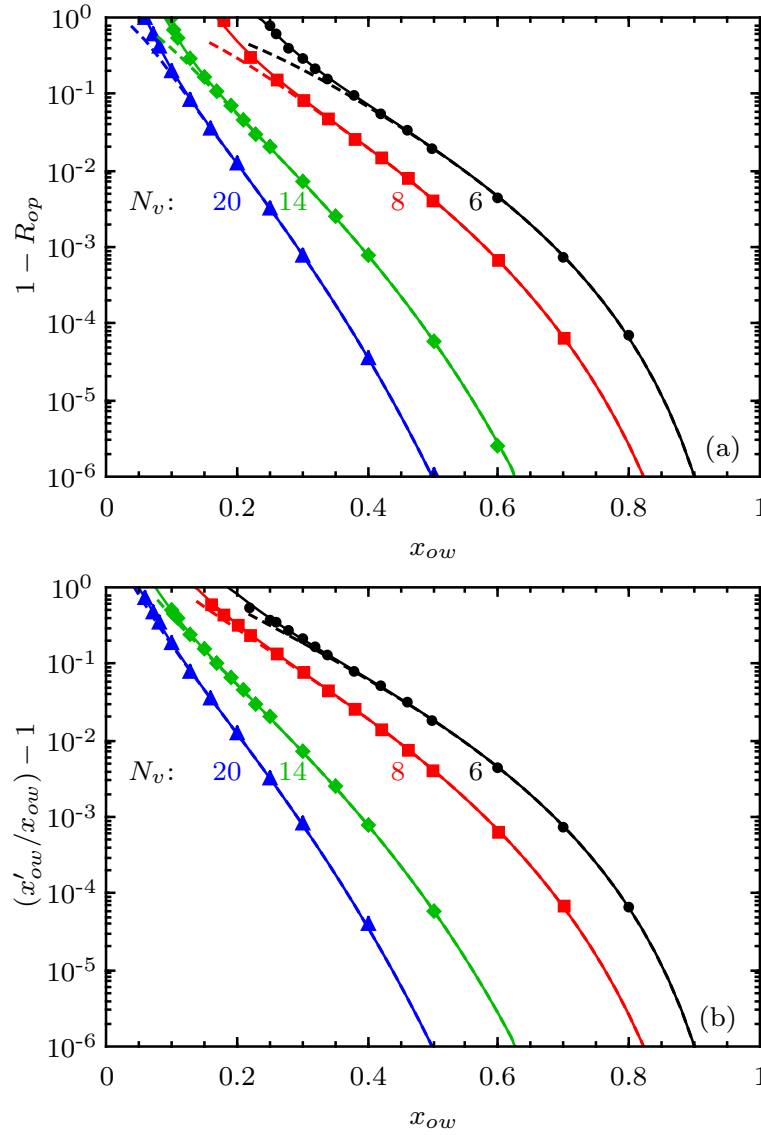


Figure IV.8: Fraction of closed porosity, $1 - R_{op}$ (a) and excess fraction of open windows within the open pore space (b) as a function of the reduced fraction of open windows for various neighbor pore numbers N_v , and large sample ($N_p \sim 10^6$). Dashed lines correspond to theoretical curves calculated in considering the first simplest closed clusters i.e., Eqs. (IV.5a) and (IV.5b). Full line corresponds to curves calculated by using approximate formulas [Eqs. (IV.6a) and (IV.6b)].

permeability close to percolation threshold. Indeed, by plotting the reduced fraction of open windows within the open pore space, $(x'_{ow} - x_{ow}^*)/(1 - x_{ow}^*)$, as a function of the open window fraction x_{ow} [Figure IV.9(a)], we find curves which are very similar to the ones obtained for permeability as a function of x_{ow} . Moreover, from pore-network simulations, we can calculate the fraction of pores in which the fluid flow occurs, $R_{op,flow}$ (= number of pores in which

flow occurs/total number of pores). It appears that fluid flow occurs only in a part of the open pore space, the other part the open pore space is made of dead ends where no fluid flow occurs [Figure IV.9(b)].

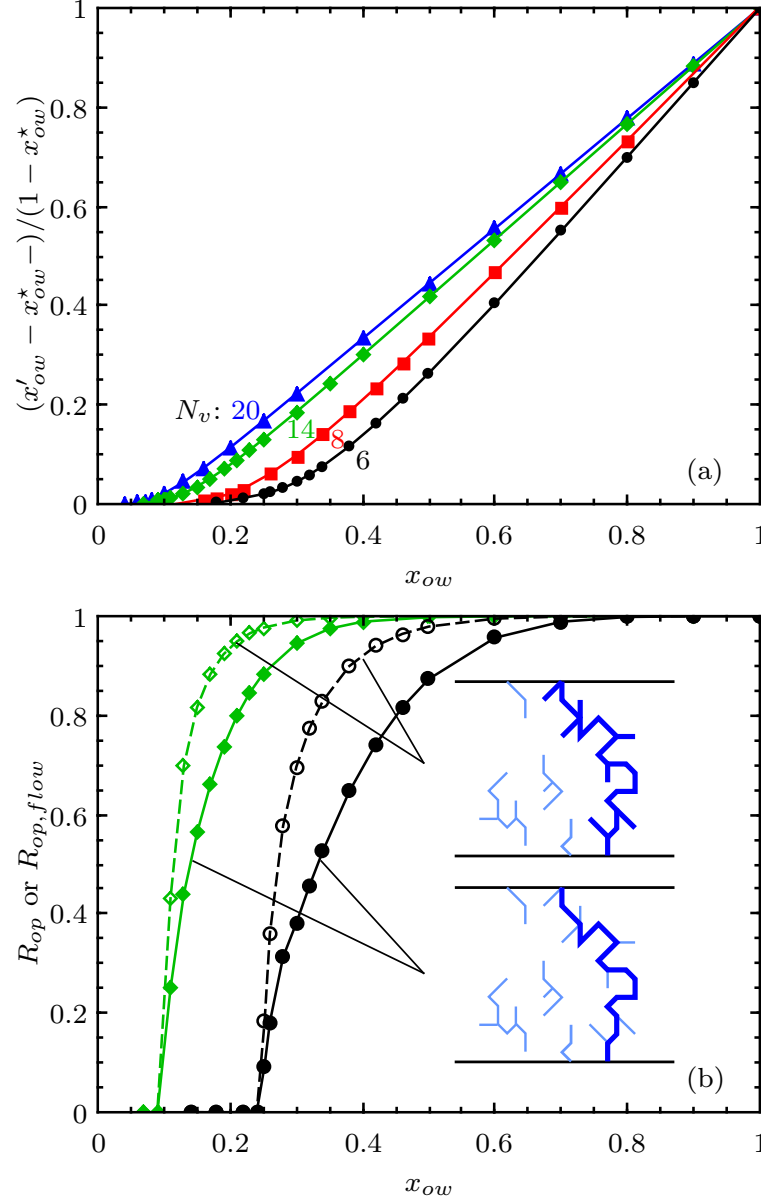


Figure IV.9: Pore-network simulations: (a) $(x'_{ow} - x^*_{ow}) / (1 - x^*_{ow})$ as a function of open window fraction x_{ow} for various neighbor pores number N_v , (b) Open porosity fraction (dashed line) and open porosity fraction without dead ends (full line) as a function of the open window fraction x_{ow} for $N_v = 6$ (black) and $N_v = 14$ (green).

From a practical point of view, accurate formulas allowing to estimate the fraction of open porosity R_{op} , the open window fraction within open pore space x'_{ow} and the percolation

threshold x_p by measuring the open window fraction and the average number of pores could be useful. First, the percolation threshold x_p can be estimated by a formula given in Ref. [198]. Then, by considering the structure of closed clusters, it seems possible to calculate the fraction of open porosity and the open window fraction within the open pore space. To begin, we calculate the fraction of pores P_k being within the first simplest closed clusters (Table IV.1). For value of x_{ow} close to 1, those simplest clusters represent the main part of the closed pore space (i.e., pore space located outside open pore space). Therefore, the fraction of open porosity $R_{op} = \frac{N'_p}{N_p}$ and the ratio $x'_{ow}/x_{ow} = \left(\frac{N'_{ow}}{N'_p}\right) / \left(\frac{N_{ow}}{N_p}\right)$ are given by

$$R_{op} = 1 - \sum_{k=0}^3 P_k \quad (\text{IV.5a})$$

$$\frac{x'_{ow}}{x_{ow}} \approx \frac{1}{1 - \sum_{k=0}^3 P_k} \left(1 - \frac{2}{x_{ow} N_v} \sum_{k=1}^3 \frac{k}{k+1} P_k \right) \quad (\text{IV.5b})$$

Table IV.1: Structures of simplest closed clusters having k open windows and $k+1$ pores, and fraction of pores P_k contained within such cluster (= total number of pores being in a closed cluster having k open windows and $k+1$ pores/total number of pores, N_p). In the ‘‘Closed cluster’’ drawing, open windows having a probability x_{ow} , and closed windows (thin gray lines) have a probability $(1 - x_{ow})$ to black lines.

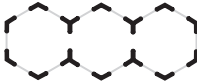
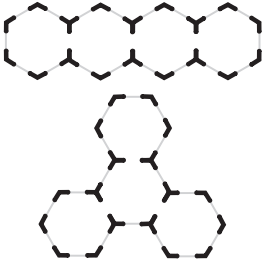
k	Closed cluster	P_k
0		$(1 - x_{ow})^{N_v}$
1		$N_v x_{ow} (1 - x_{ow})^{2N_v - 2}$
2		$\frac{3}{2} N_v (N_v - 1) x_{ow}^2 (1 - x_{ow})^{3N_v - 4}$
3		$\frac{1}{6} N_v (N_v - 1) (13N_v - 17) x_{ow}^3 (1 - x_{ow})^{4N_v - 6}$

Figure IV.8 shows that these approximated formulas are able to predict the fraction of open porosity and the ratio x'_{ow}/x_{ow} except for open window fractions close to percolation

threshold where the complexity of the closed clusters structures increases drastically. To bridge the remaining gaps between theoretical calculations and numerical simulations, x'_{ow} and R_{op} can be approximated by following equations, for $x_{ow} > x_p$:

$$R_{op} \approx 1 - \sum_{k=1}^3 P_k - \exp \left[-(3N_v + 12) (x_{ow} - 1.88N_v^{-1.2}) \right] \quad (\text{IV.6a})$$

$$\frac{x'_{ow}}{x_{ow}} \approx \frac{1}{1 - \sum_{k=0}^3 P_k} \left(1 - \frac{2}{x_{ow}N_v} \sum_{k=1}^3 \frac{k}{k+1} P_k \right) + \exp \left[-(2.9N_v + 8.2) (x_{ow} - 1.69N_v^{-1.35}) \right] \quad (\text{IV.6b})$$

with $x_p = 0.7514 \left[\frac{2}{3}(N_v - 1) \right]^{-0.9346}$ (from Ref.^[198]).

Figure IV.6 and IV.8 show that these formulas accurately predict x'_{ow} and R_{op} in the full range of x_{ow} : $[x_p, 1]$.

IV.3.3 Effective medium model for permeability

In this section, we present an effective medium model for permeability of pore-network built from the same theoretical framework as that of pore-network simulations. This model is based on a self-consistent calculation of the mean local permeability and a calculation of the macroscopic permeability. Details leading to Eqs. (IV.7) and (IV.8) are given in the Appendix.

Table IV.2: Coefficients σ_w for used lattices and weakly disordered foam. Note that for SC, BCC or Kelvin lattices, σ_w is isotropic.

Coefficients	SC	BCC	Kelvin	$N_v = 20$	random foam
N_v	6	8	14	20	$2(n+1)/2$
σ_w	1	2	4	$\frac{14}{\sqrt{3}}$	$\approx \frac{n}{2}$

The mean local permeability \bar{k} is calculated iteratively from^[180,186]:

$$\frac{1}{\bar{k} + n\bar{k}} = \sum_i \frac{x_i}{k_i + n\bar{k}}, \quad (\text{IV.7})$$

with x_i the fraction of local permeability k_i and $n = N_v/2 - 1$.

The macroscopic effective permeability is then deduced from the mean local permeability \bar{k} ,

$$K = \sigma_w \bar{k}, \quad (\text{IV.8})$$

where the coefficient σ_w depends on the structure of the porous medium (Table IV.2).

In a few simple cases, Eqs. (IV.7) and (IV.8) possess analytical solutions. This is the case for fully open-cell foam ($x_{ow} = 1$) described by a binary mixture of local permeability

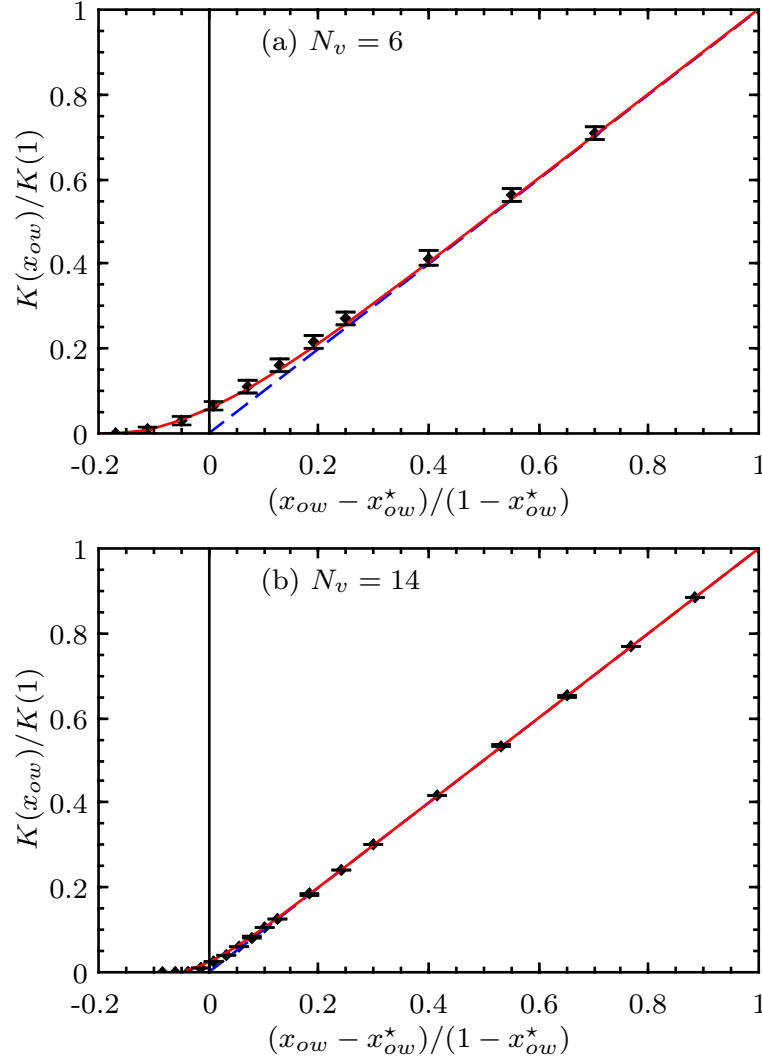


Figure IV.10: Comparison between EM model with network simulations (black diamond) for various neighbor pore numbers. “EM0” (dashed blue line) is based on the global open window fraction [Eq. (IV.9)], and “EM1” (red line) is based on the open window fraction within pore space [Eq. (IV.10)].

(see the Appendix). EM model is known to accurately predict the permeability of such a binary mixture of local permeabilities, but also to fail in its prediction for porous media having an open window fraction close to the percolation threshold [180,186]. To illustrate this point, consider the case of a porous medium having a mixture of closed windows and open windows characterized by a unique aperture parameter. The local permeability associated to the closed windows is equal to zero, and Eqs. (IV.7) and (IV.8) have an analytical solution:

$$\frac{K}{K_1} = \frac{x_1 - x_{ow}^*}{1 - x_{ow}^*}, \quad (\text{IV.9})$$

with $K_1 = \sigma_w k_1$.

As shown in Figure IV.10, this solution “EM0” reproduce correctly the linear relationship between the permeability and the parameter $(x_{ow} - x_{ow}^*)/(1 - x_{ow}^*)$ expect for an open window fraction close to the percolation threshold. In the case of foamy material where the number of neighbor pores is usually to on the order of 14 (except for low porosity $\phi \approx 0.6$), the previous equation gives a very good approximation on a large range of open window fraction (i.e., $x_{ow} > 0.2$). However, EM predictions can be improved if the open pore space is explicitly considered. Indeed, as the mean local permeability in framework of the effective medium model is calculated by considering that the mean fluid flow passes through the mean pore, the calculation of permeability should be performed on a half pore contained within the open pore space. Therefore, as shown in Figure IV.10, by considering the structure of the open pore space in calculation of permeability, via the percolating fraction of porosity R_{op} and the fraction of the open windows within open pore space x'_{ow} instead of the global open window fraction, the EM model predictions are significantly improved for the open window fraction close to the percolation threshold. In the modified EM model “EM1”, permeability is given by

$$\frac{K}{K_1} = \frac{x'_1 - x_{ow}^*}{1 - x_{ow}^*} R_{op} \quad (\text{IV.10})$$

The fraction of open porosity R_{op} and the fraction of open windows within open pore space can be estimated from the global open window fraction by using Eq. (IV.6a) and (IV.6b).

For generalization purposes, one can write:

$$\frac{1}{\bar{k}' + n\bar{k}'} = \sum_i \frac{x'_i}{k_i + n\bar{k}'}, \quad (\text{IV.11a})$$

$$K = R_{op} \sigma_w \bar{k}', \quad (\text{IV.11b})$$

where x'_i is the fraction of windows inside the percolating porosity having a local permeability equal to k_i . Note that the fraction of closed windows (for which $k_0 = 0$) within the open pore space, x'_0 , is equal to $1 - \sum_{i \neq 0} x'_i$.

After Eq. (IV.10), the physical meaning of the critical concentration $x_{ow}^* = 2/N_v$ is now more explicit: at least two open windows per pore located in the open pore space are required to start a sufficient interconnection of pores.

Other improvements of effective medium approximations based on real-space renormalization have been proposed in the literature^[180,199]. However, as the renormalization scheme depends on the lattice structure, a specific study for each lattice should to be done.

IV.4 Conclusion

In order to study the effects of both the fraction of open windows and their aperture sizes on solid foam permeability, we performed different numerical simulations at different scales:

FEM simulations computing the Stokes problem both the pore scale and at the macro-scale, and pore-network simulations of simplified flow performed on large lattices of interconnected pores. The FEM simulations at pore scale were useful to identify the pressure drop mechanism for fluid flow through solid foam and to define the local permeability associated with it. Thus, we show that the pressure drop inside fully open-cell foam can be explained by a mechanism acting at the scale of the membrane aperture and well described by Sampson's law [Eq. (IV.4)]. The FEM simulations at macro-scale with various fractions of open windows showed the ability of pore-network simulations to predict the permeability of percolating foamy medium. By using large samples, pore-network simulations results exhibit that percolation occurs when the fraction of open windows is close to $x_p = 1.5/N_v$ (≈ 0.11 for foam having $N_v = 14$), and reveal that the fraction of open windows within the open pore space is a key parameter to interpret the particular behavior of permeability for fraction of open windows close to the percolation threshold x_p .

Finally, we develop a model of effective foam permeability allowing for foam permeability to be estimated by an analytical calculation [Eqs. (IV.4), (IV.6), and (IV.11)]. In an alternative way to Sahimi et al.^[199] our model modifies Kirkpatrick's model to take into account explicitly the structure of the open pore space via the fraction of open porosity R_{op} and the fraction of open windows within the open pore space (x'_{ow}). However, Kirkpatrick's model with local permeabilities derived from the Sampson equation [i.e., Eqs. (IV.4) and (IV.9)] provides an excellent approximation for estimating permeability of foamy material having an open window fraction greater than 0.2.

By using an appropriate local permeability estimate, our approach to derive the effective permeability of porous materials could be extended to more complex microstructures such as topologically disordered foams or materials exhibiting a hierarchical porosity.

Acknowledgments

This work was part of a project supported by ANR under Grant No. ANR-13-RMNP-0003-01 and No. ANR-13-RMNP-0003-03.

Appendix

IV.A. Effective medium theory

Here, we detail the calculation of the mean local permeability. We consider a cross-section of foam [Figure IV.A.1(a)] and calculate the mean local permeability \bar{k} of a foam containing different local permeabilities $\{k_i\}$. To represent a pore inside the cross-section, we consider a half pore connected to $N_v/2$ effective pores such as $n = N_v/2 - 1$ windows have a local

permeability equal to the mean local permeability \bar{k} , and the last one located at the p th position has a permeability equal to k_i [Figure IV.A.1(b)]. Due to the heterogeneity induced by the local permeability k_i , the pressure inside the central pore $P_{i,p}$ is different from the mean pressure \bar{P} . Pressure inside neighbor effective pores are supposed equal to the effective pressure expected for each peculiar of the neighbor pore: $\bar{P} + \alpha_r \Delta \bar{P}$ with $\alpha_r = z_r / D_b$. The total flow rate passing through the central half pore is equal to $q_{i,p} = \frac{D_b}{\mu} \sum_{r=1}^{n+1} q_r = \frac{D_b}{\mu} \sum_{r=1}^{n+1} k_r (\bar{P} + \alpha_r \Delta \bar{P})$, where $k_r = \bar{k}$ for $r \neq p$, and k_i for $r = p$.

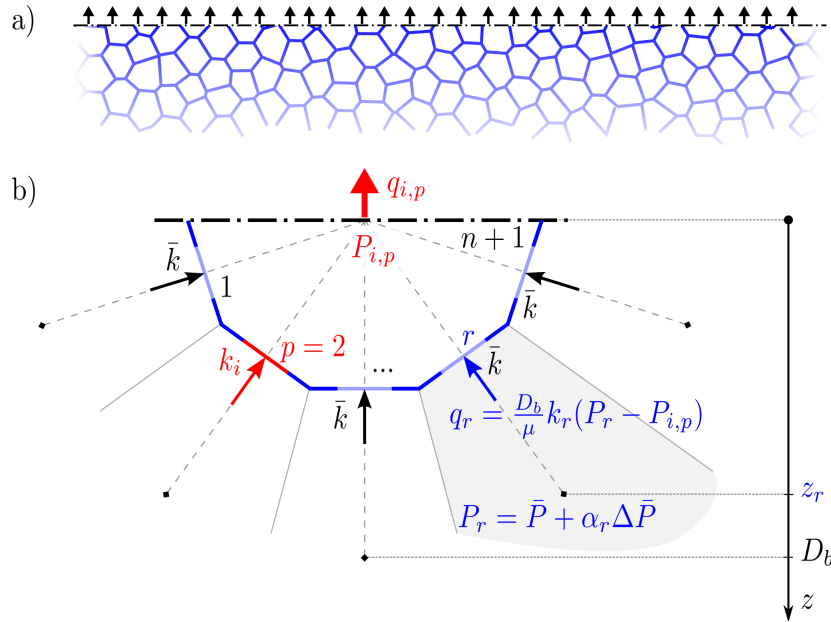


Figure IV.A.1: (a) Cross-section of foam, (b) geometrical of a half pore representative of pores contained inside the foam cross section. Note that we have to consider $n + 1$ configurations for the position p of the window associated with the permeability k_i . Figure depicts the case $p = 2$.

The total flow rate can be written in a more useful way as

$$q_{i,p} = \frac{D_b}{\mu} \left[\sum_{r=1}^{n+1} \bar{k} (\bar{P} - P_{i,p} + \alpha_r \Delta \bar{P}) + (k_i - \bar{k}) (\bar{P} - P_{i,p} + \alpha_p \Delta \bar{P}) \right].$$

The effective flow rate \bar{q} passing the effective pore is obtained by considering $k_i = \bar{k}$ and $P_{i,p} = \bar{P}$ in the previous equation: $\bar{q} = \frac{D_b}{\mu} \sum_{r=1}^{n+1} \bar{k} \alpha_r \Delta \bar{P}$.

Therefore, the flow rate $q_{i,p}$ can be expression in function of \bar{q} :

$$q_{i,p} = \bar{q} + \frac{D_b}{\mu} [(n+1)\bar{k} (\bar{P} - P_{i,p}) + (k_i - \bar{k}) (\bar{P} - P_{i,p} + \alpha_p \Delta \bar{P})].$$

Thereafter, we suppose that the total flow rate passing the central half pores $q_{i,p}$ is equal to effective flow \bar{q} leading to $0 = \frac{D_b}{\mu} [(n+1)\bar{k} (\bar{P} - P_{i,p}) + (k_i - \bar{k}) (\bar{P} - P_{i,p} + \alpha_p \Delta \bar{P})]$.

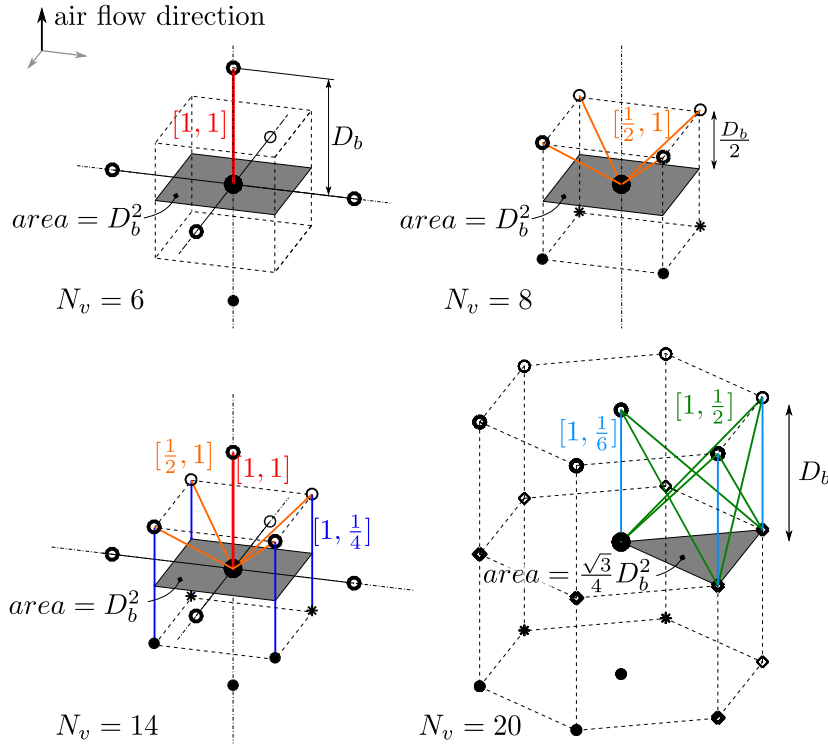


Figure IV.A.2: For each lattice, bonds per unit cross section (gray area) considered for the calculation of σ_w . A couple $(\alpha_p, \text{fraction of bonds } p_b \text{ included within cross section})$ are associated to each bond. σ_w is calculated by $\sigma_w = \sum \alpha_p p_b D_b^2 / \text{area}$.

The hypothesis leads to the pressure inside the central pore:

$$P_{i,p} = \bar{P} + \frac{k_i - \bar{k}}{n\bar{k} + k_i} \alpha_p \Delta \bar{P}.$$

Now, we may impose the self-consistency condition, requiring that the average $\langle P_{i,p} \rangle_{p,i} = \langle \langle P_{i,p} \rangle_p \rangle_i$ is equal to effective pressure \bar{P} leading to

$$\left\langle \frac{k_i - \bar{k}}{n\bar{k} + k_i} \right\rangle_i \langle \alpha_p \rangle_p \Delta \bar{P} = 0.$$

The previous equation can be written in an alternative form:

$$\left\langle \frac{1}{n\bar{k} + k_i} \right\rangle_i = \frac{1}{(n+1)\bar{k}}$$

To determine the macroscopic effective permeability, we calculate the macroscopic flow rate Q passing through the whole cross section A containing N_w window having a local permeability equal to \bar{k} . Moreover, we suppose that the gradient of pressure around cross-section $\Delta \bar{P} / D_b$ is equal to mean pressure gradient $\Delta P_{sp} / H$. Then, the macroscopic flow rate is given by

$$Q = \frac{D_b}{\mu} \left[\sum_{w=1}^{N_w} \alpha_w \right] \bar{k} \frac{\Delta P_{sp}}{H} D_b,$$

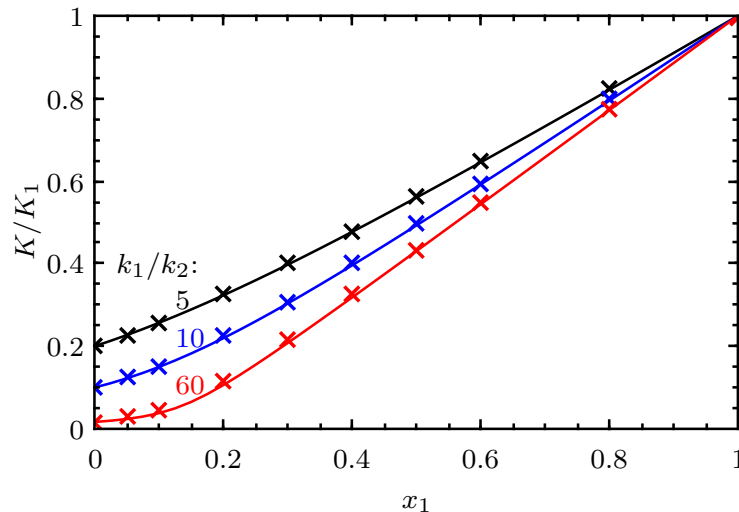


Figure IV.A.3: Comparison of EM model predictions (full line) to network simulations (cross) with $N_v = 14$.

leading to macroscopic effective permeability:

$$K = \sigma_w \bar{k},$$

where $\sigma_w = \left[\sum_{w=1}^{N_w} \alpha_p \right] \frac{D_b^2}{A}$.

For each lattice, the calculation of σ_w can be straightforward in considering the inclination of the cross section shown in Figure IV.A.2. However, for SC, BCC, or Kelvin lattice, numerical calculations performed in various inclination shown that σ_w is isotropic. In a case of weakly disordered foam (i.e., lowly polydisperse foam) we can use $\sigma_w = N_w \langle \alpha \rangle_p D_b^2 / A$ and consider the continuous limit for calculation of $\langle \alpha \rangle_p$ leading to: $\langle \alpha \rangle_p = \frac{1}{2\pi} \int_0^{2\pi} \int_0^{\pi/2} \sin\theta \cos\theta d\theta d\varphi = 1/2$. By considering the surface wall density N_w/A of a Kelvin structure which is approximately equal to n/D_b^2 , we find $\sigma_w \approx n/2$.

In the case of a binary mixture of local permeabilities (e.g. fully open foam), the mean local permeability \bar{k} is given by the following equation:

$$\frac{\bar{k}}{k_\infty} = \frac{1}{2} \left[\alpha + \sqrt{\alpha^2 + 4(1-\alpha) \frac{k_0}{k_\infty}} \right],$$

with $\alpha = 1 - \frac{k_1 k_2}{n k_0 k_\infty}$, $k_\infty = k_{V oigt} = x_1 k_1 + x_2 k_2$, $k_0 = k_{Reuss} = (x_1/k_1 + x_2/k_2)^{-1}$.

k_∞ and k_0 correspond respectively to the permeability of an infinitely interconnected network ($N_v \rightarrow \infty$) and this one of a poorly interconnected network ($N_v = 2$).

In such simple porous media, EM model accurately predicts the permeability calculated by pore-network simulations (Figure IV.A.3).

Chapter V

To go beyond PUC modeling

V.1 Representative elementary volume of disordered structures

It is true that the arrangement of idealized cells sometimes does not completely capture the random geometry of real structures (i.e., the Kelvin model is not supported by the numerical results^[129] as well as experimental data^[78]). Thus, the requirement for a more realistic structure with real foams could be raised. Below, a random representation of foaming structures based on the Voronoi tessellation is demonstrated.

In a Voronoi pattern, the partitioning is based on a set of seed points distributed in a model space where each cell is defined by all points that are closer to one particular seed point than to any others. Mathematically, given a set S of N points in a \mathbb{R}^d dimensional space, the process of associating all the locations of the \mathbb{R}^d space into polyhedral regions with the closest point of S is called Voronoi partitioning process. The polyhedral regions are called cells. The union of all the cells is then referred to as a Voronoi diagram. Theoretically, a Voronoi diagram may be constructed in any dimensional space. A cellular foam model based on Voronoi partitions of 3D space is built as follows^[200]. First, a set of N nuclei (seed points) is given in a three-dimensional finite space \mathbb{R}^3 . For each nucleus, let cell V_i be the region consisting of all locations in the space which are closer to P_i than any other nucleus $P_j (j \neq i)$, a cell V_L corresponding to seed point P_i is defined as

$$V_L(\mathbf{x}_i) = \{\mathbf{x} \in \mathbb{R}^3 \mid \|\mathbf{x} - \mathbf{x}_i\| \leq \|\mathbf{x} - \mathbf{x}_j\|, i \neq j\}, \quad (\text{V.1})$$

where \mathbf{x}_i and \mathbf{x}_j are respectively the coordinates of seed points P_i and P_j . Each seed point is surrounded by a cell that contains all points in space that are closer to this particular seed point than to any other. Consequently, cell walls will appear centrally aligned on, and perpendicular to, lines that fictively connect two neighbor seed points. Cell edges appear wherever cell walls intersect and cell vertices appear where cell edges intersect. The result is

strictly convex cells with flat faces. An ordered set of seed points can be used for creating ordered and regular structures, for instance, structures made of Kelvin or Weaire-Phelan pattern. Distributing seed points randomly within the model space without any further constraints will result in a Voronoi partitioning with poor foam resemblance.

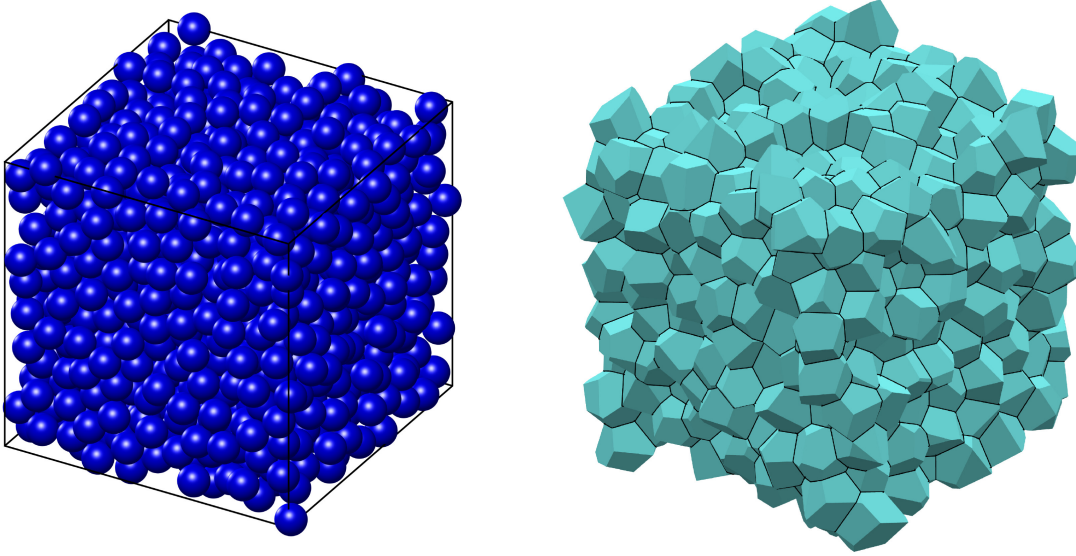


Figure V.1: (left) Close packed configuration at a density $\eta_p = 0.612$ for a random packing of 1024 mono-sized spheres, and (right) the corresponding random foam with a Voronoi partitioning.

Two main methods are often employed to generate packing of equal hard spheres where the sphere centers are used as seed points for a subsequent Voronoi pattern. In a simple way, random sequential adsorption (RSA) refers to a fairly simple process where particles are randomly added to a system if they do not overlap any previously placed particle. Without any constraints, one will finally reach a jamming limit within a lower volume fraction $\eta_p \leq 0.36$ [201], in which no more spheres can be adsorbed. Dynamically generated distributions of hard spheres also referred to as molecular dynamics simulations, can be used to drive sphere packing towards the random close packed (RCP) limit, i.e., $\eta_p \leq 0.64$. [202,203]. Jodrey and Tory provided an algorithm to construct a randomly close packed distribution of equal hard spheres [204,205]. The initial state is N randomly distributed points that represent sphere center points are generated in a basic cube with a size of L_c . Each point is surrounded by two spheres, one inner and one outer. The outer diameter $d_{out}^{(0)}$ is set initially to $2L_c \left(\frac{3}{4\pi N}\right)^{1/3}$ corresponding to a nominal packing fraction of $\eta_p = 1$. The inner diameter $d_{in}^{(k)}$ is set to the minimum center-to-center distance between any two spheres after iteration k ,

$$d_{in}^{(k)} = \min \| \mathbf{r}_{ij}^{(k)} := \mathbf{x}_i^{(k)} - \mathbf{x}_j^{(k)} \|, \quad i, j \in [1, N], \quad i \neq j. \quad (\text{V.2})$$

Initially, the inner diameter $d_{in}^{(0)}$ defines a true volume fraction which is very low, and

the outer spheres do overlap each other. The algorithm then eliminates overlaps and slowly reduces the outer diameter. The inner and the outer diameters approach each other and the algorithm is halted by an eventual coincidence of the true and nominal packing fractions. In each step, the worst overlap between spheres i and j is eliminated by moving them apart an equal distance along the line joining their centers,

$$\mathcal{D}^{(k)} = \frac{1}{2} \frac{d_{out}^{(k+1)} - \|\mathbf{r}_{ij}^{(k)}\|}{\|\mathbf{r}_{ij}^{(k)}\|}. \quad (\text{V.3})$$

Then, their new positions are defined according to the equation,

$$\begin{aligned} \mathbf{x}_i^{(k+1)} &= \mathbf{x}_i^{(k)} + \mathcal{D}^{(k)} \mathbf{r}_{ij}^{(k)}, \\ \mathbf{x}_j^{(k+1)} &= \mathbf{x}_j^{(k)} + \mathcal{D}^{(k)} \mathbf{r}_{ji}^{(k)}. \end{aligned} \quad (\text{V.4})$$

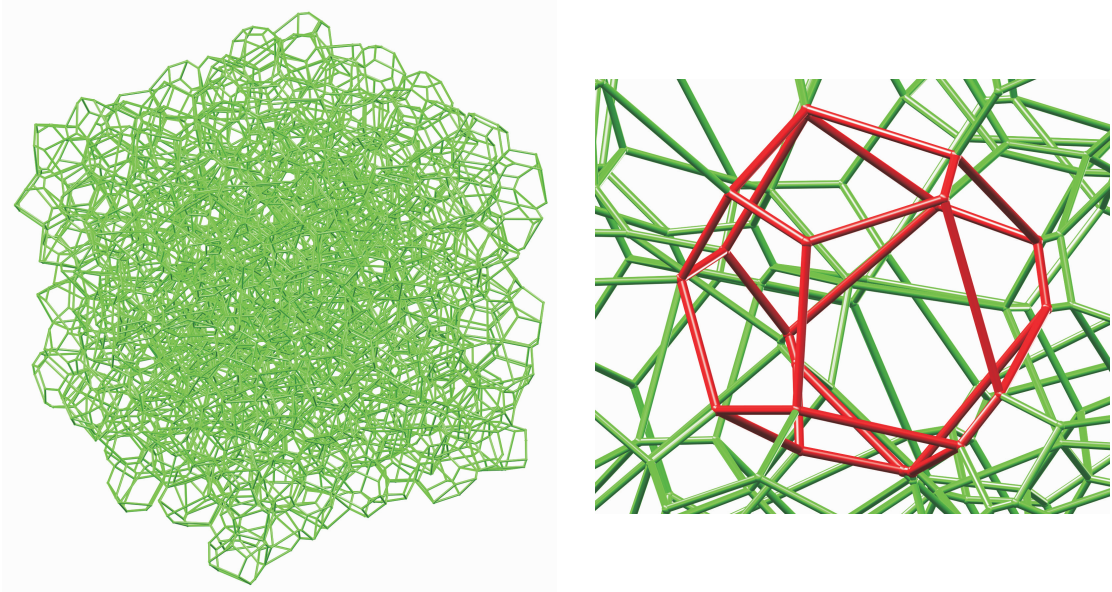


Figure V.2: Three-dimensional solid foam skeleton representing the interconnected polyhedrons from the Voronoi tessellation (left part) and detail of a typical polyhedron with a focusing on its vertex interconnection (right part).

If any overlaps remain, the outer diameter is reduced slightly as follows,

$$\lambda^{(k+1)} = \lambda^{(k)} - \frac{\kappa_i}{2^{\Gamma N}}, \quad (\text{V.5})$$

where $\lambda^{(k)} = d_{out}^{(k)} / d_{out}^{(0)}$, and $\Gamma = \lfloor -\log_{10} \Delta \eta_p^{(k)} \rfloor$. The parameter κ_i is the initial contraction rate which is independent of the size and number of spheres, and characterizes the initial rate of contraction of the ensemble. $\Delta \eta_p^{(k)}$ is the difference between the nominal and true packing fractions at the iteration k , and symbol $\lfloor \cdot \rfloor$ is the greatest integer function.

Table V.1: Algorithm for generating the close random packing of equal hard spheres.

	Input: Cubic size L_c , number of spheres N , and desired volume fraction η_{pf}
	Output: Desired positions of N spheres
1.	Create an initial random matrix of size $N \times 3$, $\mathbf{x}^{(0)}$, for N positions of spheres
2.	Compute $d_{in}^{(0)}$, $d_{out}^{(0)}$, and $\eta_p^{(0)} = \frac{\pi N}{12} \left(d_{in}^{(0)} \right)^3$
3.	while $\eta_p^{(k)} < \eta_{pf}$ do
4.	For each pair of spheres: Compute $d_{ij}^{(k)} = \ \mathbf{r}_{ij}^{(k)} \ $ with $i, j \in [1, N]$, $i \neq j$
5.	if $d_{ij}^{(k)} < d_{out}^{(k)}$ do
6.	Move two spheres apart using Eq. (V.4)
7.	endif
8.1.	Compute $d_{in}^{(k+1)}$ using Eq. (V.2), $d_{out}^{(k+1)}$ using Eq. (V.5)
8.2.	Update $\eta_p^{(k+1)} = \frac{\pi N}{12} \left(d_{in}^{(k+1)} \right)^3$
9.	endwhile
10.	Obtain the exact desired fraction η_{pf} by reducing the sphere diameter $d_{in}^{(k+1)}$.

The above algorithm is summarized in Table V.1. For illustration purposes, the left part of Figure V.1 shows an assembly of 1024 spheres with a volume fraction of 0.612. This was generated in less than 30 seconds on an Intel(R) core(TM) i7-4500U, 1.80 GHz, 2.40 GHz, 4 GB RAM. The 3D Voronoi diagram based on this random dense packing of spheres is shown in the right part of Figure V.1. The Voronoi algorithm generates around each seed a convex polyhedral unit cell made of vertices, joined by edges delimiting planar faces, which connect neighbor cells. Finally, a foam skeleton is completely established (see Figure V.2), and the corresponding finite mesh models of skeleton and pore domain are graphed in Figure V.3.

V.2 Applications and discussions

V.2.1 Foamy structures

As previously mentioned, three-dimensional packings of cells of equal volumes have been used successfully to represent real cellular foam structures, and these unit cells can be more realistic approximations to real foam topology than other simple types of idealized unit structures. Within their complex three-dimensional structures, it seems difficult to define purely analytical predictions of fundamental mechanical and transport properties. In this regard, an idealized cubic unit cell^[30,152,206,207] or simple two-dimensional patterns^[10,160] also may be employed to study morphological features of foam materials.

On the contrary, for some specific cases, the modified or like-Kelvin unit cell should

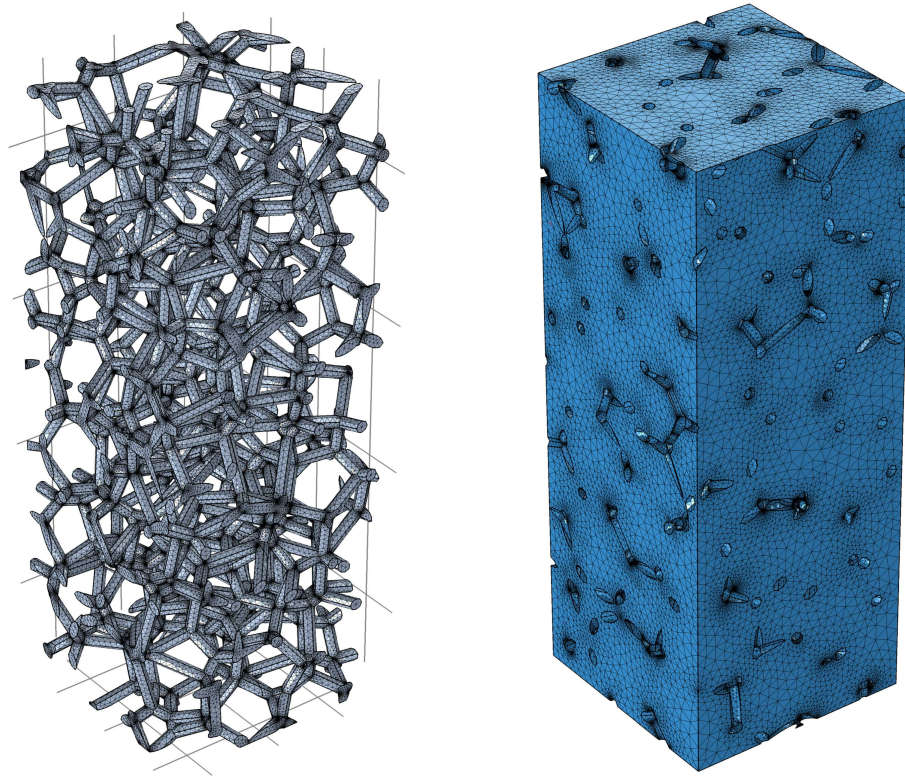


Figure V.3: Graphs of finite element model of skeleton frame (left part, i.e., 1 379 316 tetrahedral elements) and pore domain (right part, i.e., 1 660 493 tetrahedral elements). For the sake of visibility, these FE meshes are created from a quarter of the assembled foam presented in Figure V.2, and here they present an open cell foam structure having a porosity of 0.914.

be considered to characterize foamy structures with their advanced morphology features: membrane unit cell^[83,130,139], parallel unit cell^[75]. With high porosity foams for acoustical application, it is seen that the Kelvin arrangement can mimic the transport property as well as acoustical performance. However, from a work by Bufful et al.^[127], it can be stated that there are clear differences in effective elastic properties between the Kelvin and Weaire-Phelan structures, and the strut shape of these idealized cells also have a strong influence on the computed results of overall elastic properties.

Beginning with random foams having a mono-sized structure (monodisperse foams), using the previously described process in Section V.1, more generally, it can be stated that our numerical procedure can generate foam structures that are very consistent with both experimental characterization data^[78] and numerical results^[129,132] previously reported. Figure V.4 shows the distribution $\mathcal{P}(F)$ that a cell has F faces, and $\mathcal{P}(E)$ that a face has E edges. More detailed in morphology foam property, the cell volume V_{ce} and the strut length L_{li} were

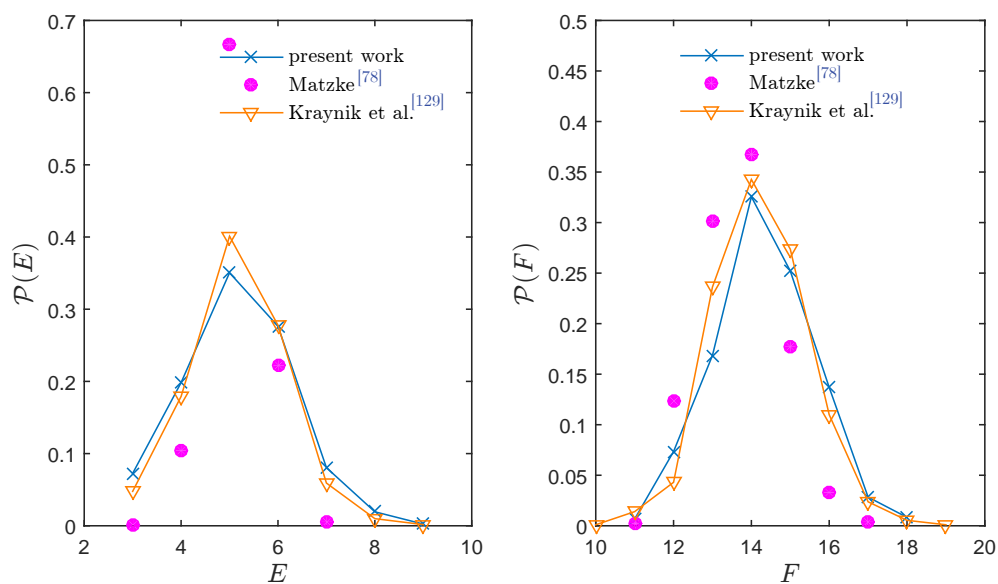


Figure V.4: Distribution of cells with F faces (left) and faces with E edges (right) in compared with Matzke's experimental data and numerical simulations provided by Kraynik and co-workers.

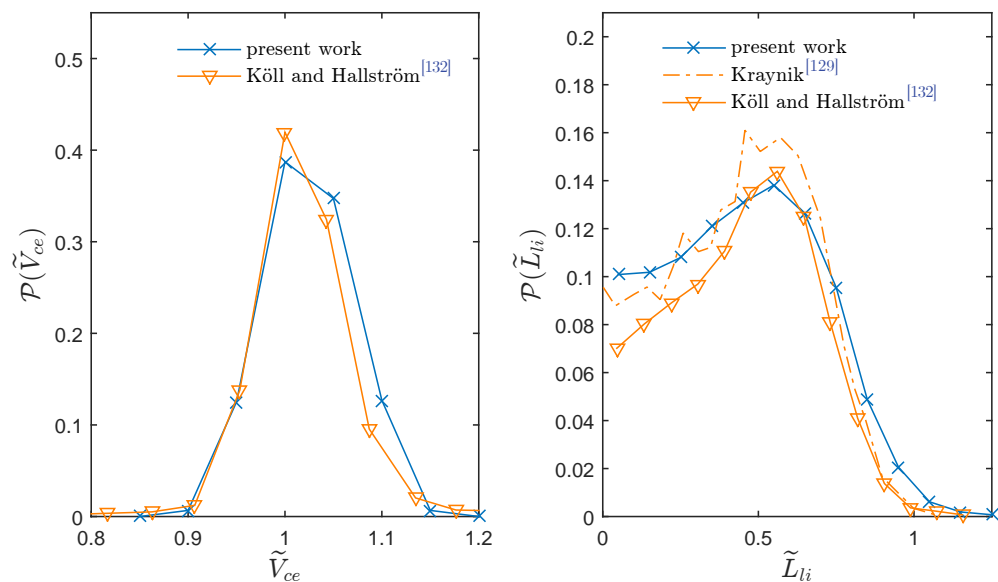


Figure V.5: Graphs of the normalized cell volume (left part) and the normalized edge length (right part) distributions of Voronoi random foam in compared with previous numerical works.

also normalized with respect to the average cell volume \bar{V}_{ce} and the strut length $\bar{L}_{li} := \bar{V}_{ce}^{1/3}$ as $\tilde{V}_{ce} = V_{ce}/\bar{V}_{ce}$ and $\tilde{L}_{li} = L_{li}/\bar{L}_{li}$, respectively. Two observed distributions $\tilde{V}_{ce} \mapsto \mathcal{P}(\tilde{V}_{ce})$ and $\tilde{L}_{li} \mapsto \mathcal{P}(\tilde{L}_{li})$ are graphed on Figure V.5. Regarding the structure that has narrow distributions [$\mathcal{P}(E)$ and $\mathcal{P}(\tilde{L}_{li})$] of morphological property, it could be required a relaxation step in Surface Evolver^[135] could be required to undertake^[129,132]. As a result, after this step, we obtain a relaxed structure foam in which the cell window in pentagon shape has a proportion more than 60% that is shown in Matzke’s experimental data (see left part of Figure V.5) and identical to the proportion in our work of morphological characterization [see, Figure III.3(c), Chapter III]. In our materials with monodisperse cell size, the results of the distribution of length strut measured in a set of 10 samples are in good agreement with numerical modeling^[129,132] and show clearly that there is no proportion of very short length struts and the struts, with their length around 0.45 times the cube root of the average cell volume, are more common being around a value of 30% [see, Figure III.3(a), Chapter III].

Let us go further in real random foamy materials such as polydisperse^[208] or graded^[209,210]

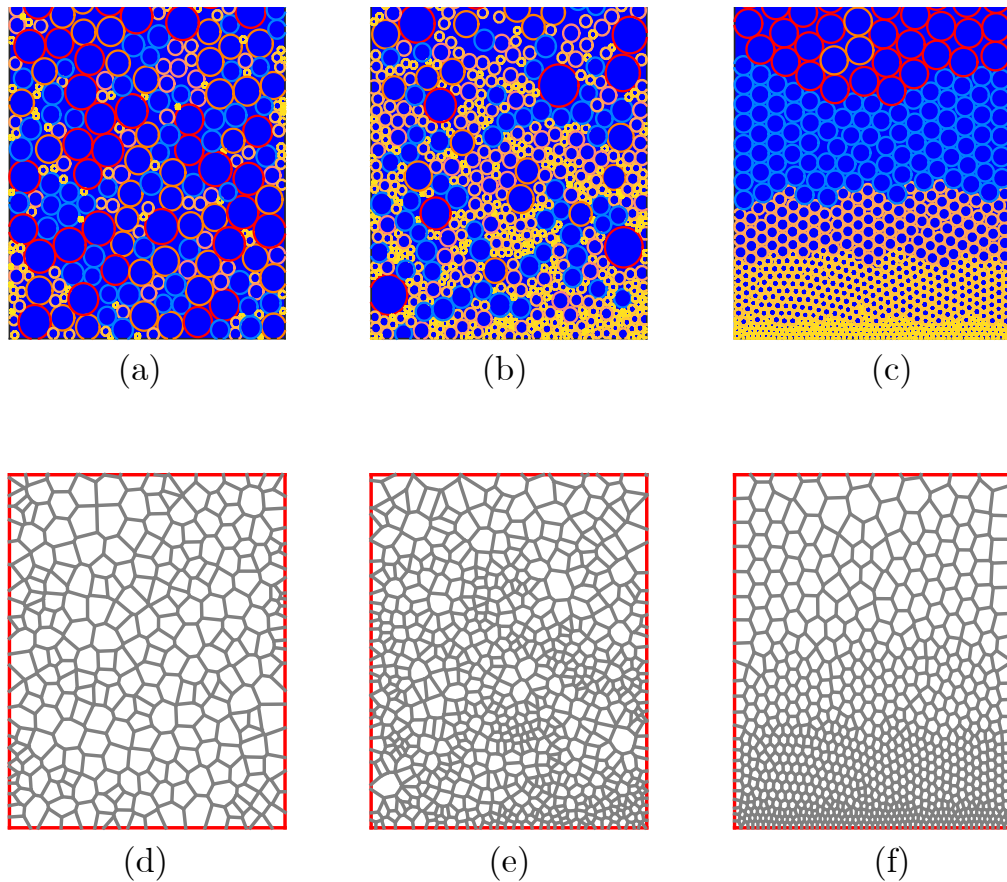


Figure V.6: Graphs of multi-sized disc packing with the Gaussian (a), Gama (b), and graded (c) distributions, and the corresponding Voronoi patterns of 2D foam structure (d,e,f), respectively.

foams. Recently, a growing community of engineers and scientists have showed their interest in these engineering materials because of their functional property. As previously described, when investigating the problem of generating the distribution of seed points, however, it may be a limitation of the RCP algorithm in generating powder-based structures of densely multi-sized spherical packing. For handling this problem, the Discrete Element Method^[211] (DEM) or Dropping or the Rolling Method^[212] (DRM) could be a more efficient tool.

To demonstrate both multi-sized structures and the numerically generating process, therein, we work here with two-dimensional structures. In the first place, a distribution of seed points is needed. Of course, the dense packing of hard discs in the place of spheres is required. Here the DEM approach is used to carry out this task (see e.g., Chapter 7 in Ref.^[213]).

For polydisperse foam structures, a hard disc packing with a size Gaussian distribution is initially generated. The ratio of the maximum to minimum element size is 10 [see Figure V.6(a)]. This ratio is equal to 17 in the case of a packing based on Gama distribution [Figure V.6(b)]. The area fractions of these dense disc packings are 0.80 and 0.82, respectively. The corresponding constructed foam structures are shown respectively in Figures V.6 (d) and V.6 (e). When generating a graded foam structure, we design 5 monodisperse packing layers, in which a disc size ratio between two neighborhood layers is set at 1.5 [see Figure V.6(c)]. From there, a two-dimensional graded foam sandwich structure corresponding to the close packed configuration with a graded variation of disc size and at a density of 0.82 is provided.

From the three multi-sized foam structures reconstructed above, it can be stated that the proposed procedure readily allows generating the complex morphology of functional cellular materials. This may be beneficial as a useful source of information for modeling and designing such materials.

V.2.2 Computational example

In this part, two numerical frameworks (mentioned in Subsection I.4.2) are used for modeling acoustical foams in order to compare their efficiency in implementations. The considered material is idealized with a periodic unit cell based on the Weaire-Phelan structure. The open- and closed-cell skeletons are illustrated in the bottom panels of Figure I.15, in which a strut framework is made of cylindrical ligaments and spherical nodes. For illustration purposes, a foam-based material with a high porosity of 98% is characterized with two type of morphology properties: open cell structure [see Figure I.15(c)], and closed-cell one with a membrane closure rate of 0.3 (an identical closing rate of membranes for all windows, see Figure I.15(d)). The size of the unit cell is equal to 1 mm. In this work, both BVPs and PDEs are solved by using the finite element method and the commercial software COMSOL Multiphysics. Figure V.7 presents the finite mesh models (a type of tetrahedral element) of two representative volume elements. As can be seen from the number of elements that: Using

the same fine mesh level (i.e., the same maximal element sizes and maximum element growth rate, etc.), the element number of membrane unit cell is 1.7 times greater than the number in open cell, because of a higher mesh concentration in the space around the boundary of the very thin membrane.

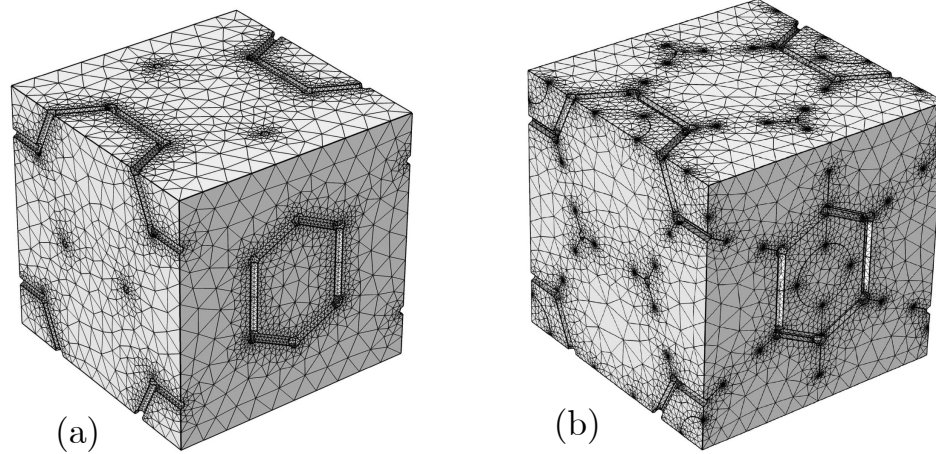


Figure V.7: Unit cell finite meshes: a model of 269 931 tetrahedra used to open-cell structure (a), and a model of 469 358 tetrahedra used for the closed-cell one (b).

The numerical micro-scale fields from both hybrid and direct methods are illustrated in Figure V.8 for the case of membrane foam. In there, the asymptotic fields for the representative element volume of low-frequency scaled velocity field, high frequency scaled velocity field, and low-frequency scaled temperature field from hybrid solution are shown in Figure V.8(a)–(c). For the direct method, Figures V.8(d)–(i) present the results of micro-scale dynamic viscous and thermal permeability distributions at three different frequency regimes [40, 2000, and 5000] Hz. It can be seen that at low-frequency, the viscous dissipation is concentrated in the center of membrane apertures [Figure V.8(d)], and thermal conduction occurs mainly in the center of cell pores [Figure V.8(g)]. However, at high frequency, the dense fluid acceleration and heat exchange phenomena seem to occur in the vicinity of membranes [Figure V.8(f)] and along the boundary of the pores [Figure V.8(i)]. It should be noticed that the both local dynamic viscous and permeability fields at low frequency [Figures V.8(d) and V.8(g)] are very consistent with their static distributions [Figures V.8(a) and V.8(c)], respectively.

Figure V.9 and Figure V.10 show respectively the results of the effective density and the effective bulk modulus numerically obtained from both approaches. As can be seen in the sub-plots, the frequency-dependent effective parameters show a good agreement. In terms of membrane effects, it is clear that the membranes have a strong influence on both real and imaginary parts of these effective parameters.

In addition, we compare the computational costs (in seconds) of the two numerical

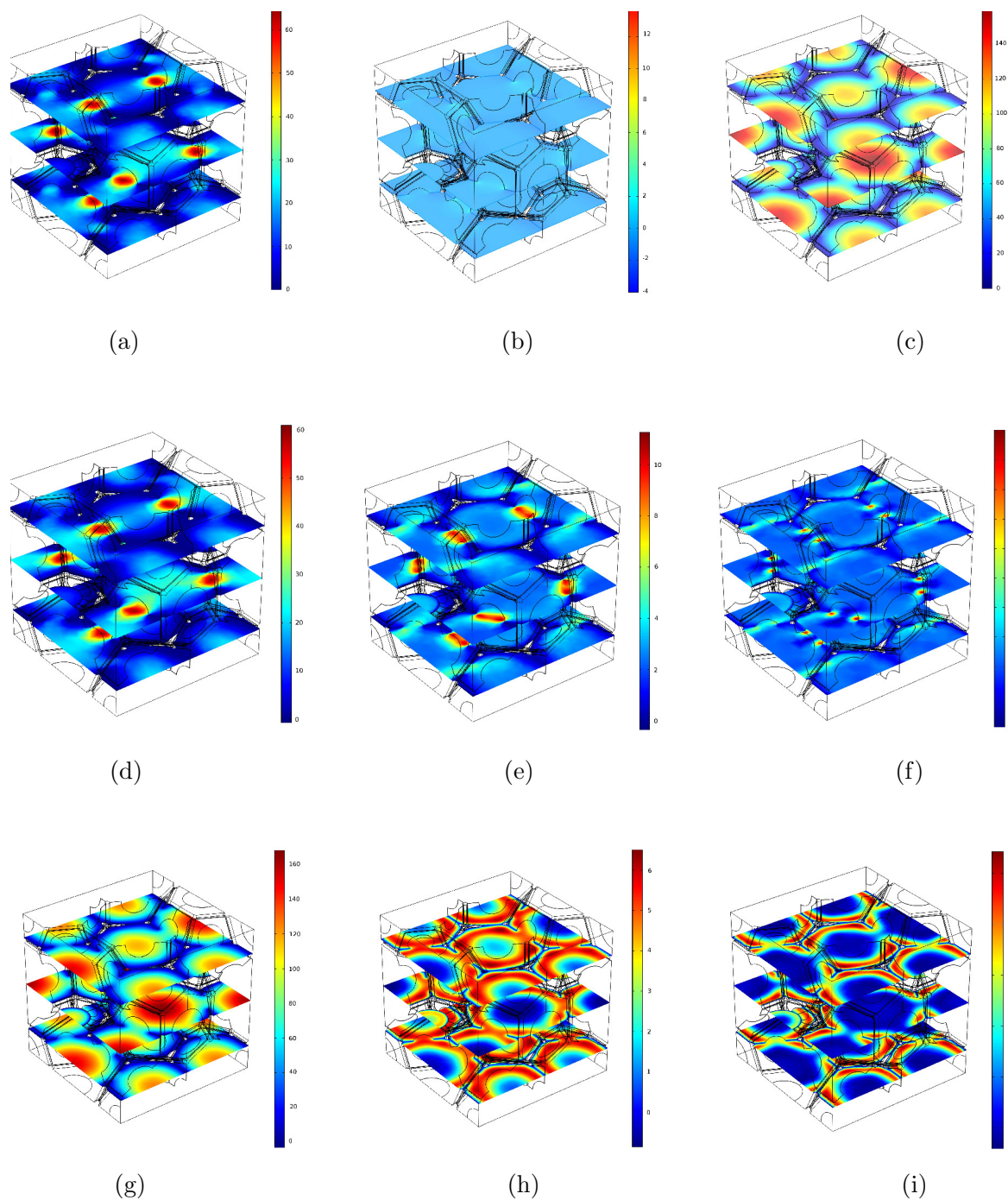


Figure V.8: Asymptotic fields for the representative element volume. **Hybrid method:** (a) low-frequency scaled velocity field \mathbf{k}_{0xx} [$\times 10^{10}$ m²], (b) high-frequency scaled velocity field $\mathbf{E}_x / \nabla \varphi$ [-] for an external unit field \mathbf{e}_x , and (c) low-frequency scaled temperature field \mathbf{k}'_0 [$\times 10^{10}$ m²]. **Direct method:** [(d,e,f)] and [(g,h,i)] are respectively shown for real parts of dynamic viscous and thermal permeability distributions \mathbf{k}_{xx} [$\times 10^{10}$ m²] and k' [$\times 10^{10}$ m²] at three frequencies 40 Hz, 2000 Hz, and 5000 Hz (from left to right).

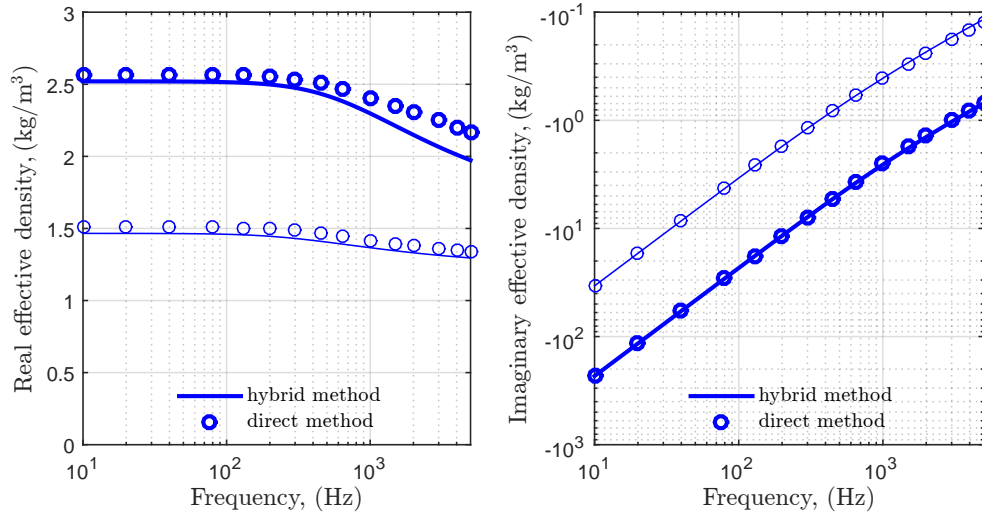


Figure V.9: Real (left) and imaginary (right) parts of the effective density. The results are shown for: hybrid numerical (continuous lines), direct numerical (circle symbols) methods, and open-cell foam (thin objects), and closed-cell foam (thick objects).

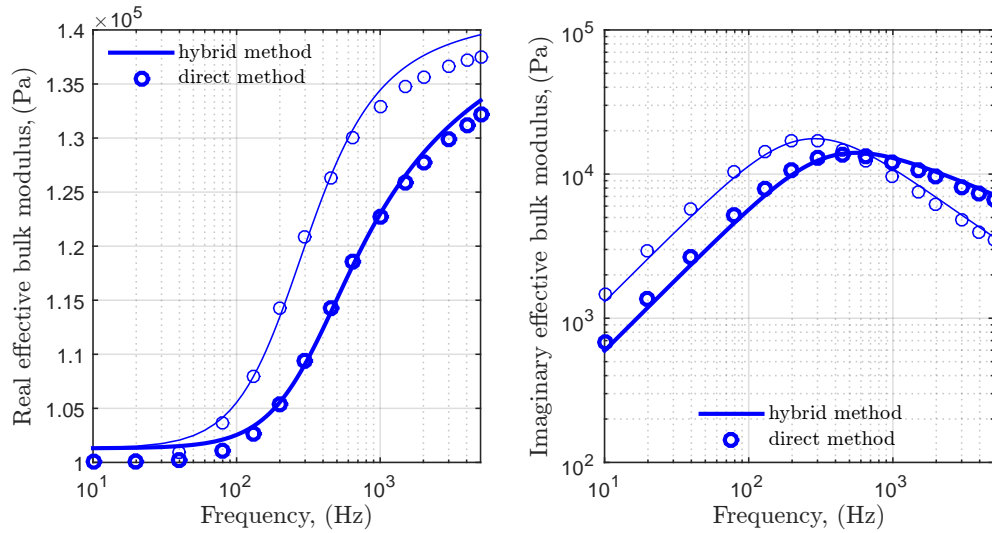


Figure V.10: Real (left) and imaginary (right) parts of the effective bulk modulus. The indicated legends are the same as illustrated in Figure V.9.

framework methods. It is to be noted that all computations were run on a desktop with Intel®; Xeon®; CPU X5690, @3.47 GHz, and 64 GB of RAM. As shown in Table V.2, for the case of open foam, the total time consumption on hybrid method is around 10 times smaller than that of the direct computation, and a larger ratio around 17 can be observed for the membrane case. Additionally, the membrane unit cell having a larger number of finite

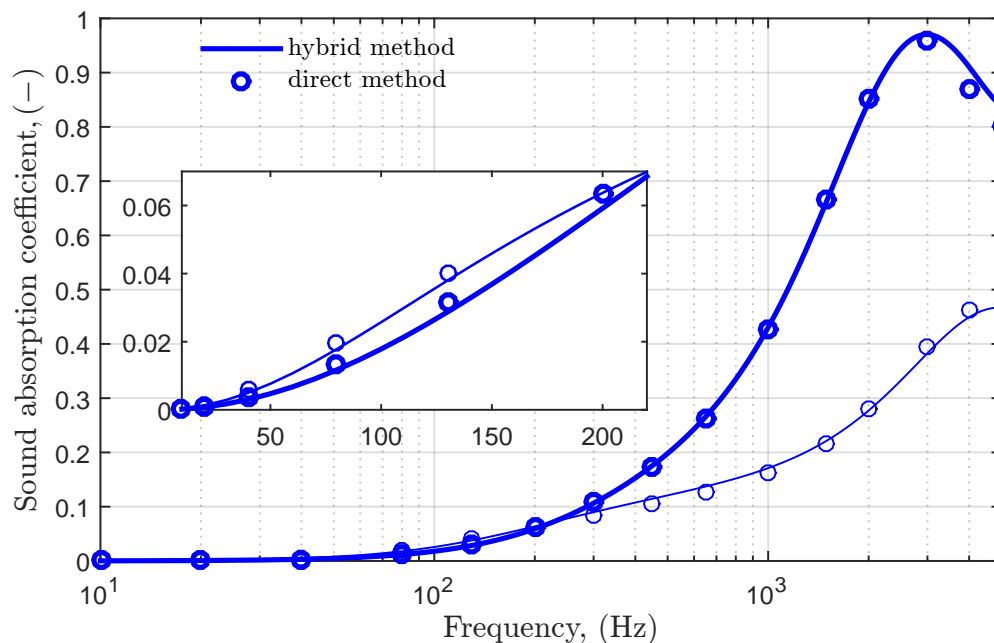


Figure V.11: The sound absorption coefficient at normal incidence of the foams obtained from hybrid (lines) and direct (circles) simulations. Thin and thick objects are for the foam without and with membranes, respectively. The sample thickness is equal to 25 mm.

Table V.2: The comparison of computational time between two numerical methods. The direct work is conducted with 15 different frequencies.

Method	Equations	Time consumption (s)	
		Open cell foam	Closed cell foam
Direct	Momentum equation	5427	13076
	Energy equation	288	1274
Hybrid	Stoke equation	518	755
	Laplace equation	25	48
	Thermal conduction equation	20	23

elements leads to a time computation more costly than that for the open unit cell in both computations. The cost of the computational time for the membrane structure was 2.5 and 1.5 times higher compared with that of the open structure, respectively, in the direct and hybrid computations. It can be seen that these values are approximately of the same order as the ratio of the element numbers previously analyzed.

Finally, we estimate the sound absorption coefficient at normal incidence in order to demonstrate the consistent results of two proposed methods and show how membrane frac-

tion affects on the acoustical property of these foams. As can be seen in Figure V.11, the membrane foam shows clearly a high acoustic absorption in comparison with the sample without membranes.

V.2.3 Summary of the numerical framework

The local geometrical generating and the numerical predicting of the macroscopic properties of foam-based materials were presented. The reconstructing process of REV's includes several foam structures having both ordered and disordered states. Two options of the idealized unit cell, a single cell (Kelvin cell) and a pair of two individual cell (Weaire-Phelan), are provided, detailing the ligament morphology. For the disordered foams, various levels of polydispersity are considered. For all cases of random foam models, the keystone of the proposed method rests on the reconstructions of corresponding ensemble of seed points. The Voronoi tessellation tool is then used to obtain the polycrystalline structures of certain materials. From the models of a large number of individual cells, it can be seen that this numerical geometrical modeling can mimic several morphology properties of real materials such as structural property (e.g., distribution of cell size, distributions of window area and ligament length, shape morphology of length and window, etc.), homogenized properties (e.g., fractional density). As a result, realistic geometry models may be used to simulate more accurately a number of functional properties at the macroscale such as mechanical, thermo-mechanical, and fluid dynamic properties.

As the main focus of this dissertation is on acoustic applications, a detailed description considering the numerical existing methods to characterize acoustical porous materials as an equivalent fluid is also provided. It is agreed that both direct and hybrid methods can predict the macro-properties of materials via a simple REV (a PUC based on the Weaire-Phelan structure as an example). The comparison of time cost indicates that the hybrid procedure is a cheaper option. As a result, our work will follow up on this framework in order to characterize acoustical materials. From the computations over the Weaire-Phelan structure (consisting of 8 cell pores), it can be seen that we have to face challenges of time as well as memory consumption. Especially in the case of membrane material, it requires a large number of elements in mesh models because the geometry involves very narrow spaces around membranes. We have to pay special attention to this point when considering a complex REV in numerical works for such materials. Alternatively, several existing methods can solve the problem of fluid flow in porous media without the finite element modeling (e.g., pore-network simulation, self-consistent model, see chapter IV, or lattice Boltzmann method, fast Fourier transfer, etc.). In addition, the fact of considering only a simple PUC having a large number of configurations should be still more efficient in terms of characterizing materials within membrane components (see chapter III).

Chapter VI

Conclusions and future work

VI.1 General conclusion

This thesis addresses the problem of characterizing sound absorbing materials. The objective of the project is to develop a method linking the local geometry of a low density cellular foam to its acoustic macro-behavior and to optimize its structural parameters in order to archive the desired acoustical performance. Regarding the research results it can be stated that this work leads to the following conclusions:

- ✓ For the design optimization of acoustic materials, we investigated the potential of surrogate models (polynomial chaos expansions) to accurately approximate mappings between key microstructural features and homogenized acoustical properties. The approach relies on Legendre orthogonal polynomials and enables appropriate convergence over the parameter space to be ensured. The results demonstrate that the framework allows the sound absorption coefficient to be predicted over an appropriate range of frequencies, so that the optimization of microstructures under various types of constraints can be envisioned at a reasonable computational cost to support the design for noise reducing materials and structures.
- ✓ The contribution of this work to material design and engineering relies on the fact that we produced successfully a series of cellular samples having the same high density around 0.98 and the same mono-sized cell structure at a scale of 0.8 mm but different values of the closure rate of the windows separating the foam pores. Here, a gelatin solution with a concentration varying from 12 to 18% was used in the foam making process. In these fabricated foamy samples, the variations of the proportion of closed cells and the size distribution of apertures for open-wall cells lead the interesting macroscopic transport and acoustic performance as desired.
- ✓ A set of techniques and processes has been used to experimentally measure structure

and properties of studied materials. In order to overcome the limitations of the previous methods for morphology characterization the SEM images of the complex microscopic structure of membrane foams, we extended existing methods by focusing not only on foam images of an area having a large number of cells but also on foam images of individual cell walls. This allowed to accurately estimate the level of the closed membrane (by fitting ellipse of aperture and fitting polygon of wall's vertices) as well as the statistical morphology of wall shape such as: number of sides, strut length, wall area. These morphological features of local geometry are important input information for multiscale modeling works, the observed numerical results are validated by experimental data from resistivity and standing tube impedance measurements. Beside acoustics, it is to be noticed that our proposed procedure for microstructural characterization can be widely applied for other purposes.

- ✓ In acoustic modeling of the studied material, it can be seen that numerical and empirical models based on a single unit cell are limited because of its complex membrane morphology as well as large varying properties. We dealt with this restriction through a numerical framework together considering a configuration number of the periodic unit cell. Based on the data of image characterization, for each foam sample, we reconstructed a periodic unit cell having some windows partly closed at a closure rate, and other windows fully closed by membranes. All combinations of partially and fully closed face's location in PUC are represented by a number of equivalent configurations because of the symmetry of Kelvin structure. From this, a systematic relationship between microstructural property and macroscopic performance of membrane foams is investigated. The obtained numerical results of transport and acoustic properties show a good agreement with experimental data. The more detailed the proposed method characterized the local geometrical properties, the more accurate the predictions of macroscopic properties were obtained. Comparing with the existing methods, our contributions may be considered in terms of modeling absorbing membrane foam-based materials.
- ✓ In terms of the permeability of membrane foamy materials, we study how membranes separating the foam pore connectivity affect on this physical parameter. We use numerical methods to carry out this objective. It is provided from results of finite element model that, for partly open cell foams, we obtain a robust power-law between permeability and the membrane aperture size that is very consistent with the local pressure drop mechanism originally suggested by Sampson. With this local law, pore-network simulations are conducted with a low computational cost, able to successfully reproduce the finite element results and handle the permeability and percolation problem with foam structure on various lattices. An effective medium model for foam permeability based on Kirkpatrick's model is then proposed, showing an ability to reproduce the results of network simulations. From the observed results, a complete validation of

computational models is obtained when considering a large number of configurations of multiscale model.

- ✓ This work presents a systematic numerical method for modeling cellular materials in acoustics: (i) the local geometrical properties of ordered foams is idealized a PUC based on the Kelvin partitioning; (ii) the hybrid numerical methods based on the technique of periodic asymptotic homogenization is used to characterize the acoustic absorption behavior of the absorbing materials, as an equivalent fluid with its effective parameters. In the rest of this work, we also mentioned the slightly and highly disordered foams (based on Voronoi partitioning) as well as a comparison between the employed numerical method with the direct method in order to show the consistent results between two approaches and confirm the advantages of the hybrid framework in terms of computational efficiency.

VI.2 Future work

Although the provided methodologies and results within this dissertation are quite good and constitute a set of powerful tools, it is necessary to mention its perspectives. Here, we briefly describe some interesting research topics that should be further investigated and addressed:

- Beginning with the proposed pore-network model, it could be interesting to extend this model to other transport properties such as the tortuosity α_∞ or the viscous characteristic length Λ . Additionally, application of the pore-network simulation could be extended to various porous foamy materials (i.e., topologically disordered foams or containing double porosity).
- It is also suggested to go further into generating numerically the complex foam structure in order to investigate their functional property in real industrial applications. Three-dimensional structures of graded foam or polydisperse foam with arbitrary distributions of cell size can provide useful input for further modeling. Going further in this way, a multilayer made of the cellular materials with other functional layers should be considered.
- In terms of multiscale surrogate models, a high-dimensional problem with more input parameters (e.g., considering that individual windows have a different closed rate, multilayer has variations of porosity, cell size) could be studied through developing the present method but with a sparse grid technique.
- Using the symmetry of Kelvin cell shape, the idea of the equivalent configuration should be extended to other purposes in mass and heat transfer phenomena that are associated with solid foam structures. Macro-scale behavior of materials could thus be achieved with a reduction of computational cost.

Appendix A

A systematic link between microstructure and acoustic properties of foams: A detailed study on the effect of membranes

Preface

- **Authors and establishments:**

- **Van Hai TRINH**, Ph.D. student, Université Paris-Est, Laboratoire Modélisation et Simulation Multi Echelle, MSME UMR 8208 CNRS, 77454 Marne-La-Vallée, France.
- **Minh Tan HOANG**, Ph.D. doctor, Faurecia Interior Systems, Acoustic Tech-Center, Z.I F. Sommer BP13, 08210 Mouzon, France.
- **Camille PERROT**, Associate professor, Université Paris-Est, Laboratoire Modélisation et Simulation Multi Echelle, MSME UMR 8208 CNRS, 77454 Marne-La-Vallée, France.
- **Vincent LANGLOIS**, Ph.D. doctor, Université Paris-Est, Laboratoire Géomatériaux et Environnement, LGE EA 4508, 77454 Marne-La-Vallée, France.
- **Yacine KHIDAS**, Ph.D. doctor, Université Paris-Est, Laboratoire Navier, NAVIER UMR 8205 CNRS, 77454 Marne-La-Vallée, France.
- **Olivier PITOIS**, Ph.D. doctor, Université Paris-Est, Laboratoire Navier, NAVIER UMR 8205 CNRS, 77454 Marne-La-Vallée, France.

- **State of publication:**

- Proceeding: V.H. Trinh, M.T. Hoang, C. Perrot, V. Langlois, Y. Khidas, O. Pitois, in the Proceeding of PoroMechanics IV, The sixth Biot Conference on PoroMechanics, edited by M. Vandamme, P. Dangla, J.-M. Pereira, S. Ghabezloo (ENPC, Paris, France, 2017), pp. 1405–1412. This is available online at: <https://hal-upec-upem.archives-ouvertes.fr/hal-01664267/>
- Published date: July 2017.

- **Contribution of the paper:**

The context of this paper focuses on the preliminary results of the membrane foam project. In this work, to overcome the limitations of existing methods, a new idea of the way to characterize foam morphology was established. By considering both proportion of fully closed walls and the level of membrane closing in partially closed walls, the numerical predictions of both transport and acoustic properties are in agreement with the experimental data. However, with the objective as a short introduction about our project, we just worked with 4 foam samples, and for each sample, one configuration of the periodic unit cell is selected to perform the multiscale computations.

- **V. H. Trinh’s contributions:** V. H. T. conducted the acoustical measurements and performed the data analysis. V. H. T. performed the numerical calculations, participated in writing the manuscript, and discussing the results.

Bibliography

- [1] G. Bugliarello, A. Alexandre, J. Barnes, C. Wakstein, et al. *The impact of noise pollution: A socio-technological introduction*. Pergamon, 1976.
- [2] EU Directive. Directive 2002/49/ec of the european parliament and the council of 25 june 2002 relating to the assessment and management of environmental noise. *Official Journal of the European Communities*, **189**(12):0012–0026, 2002.
- [3] M. Guarinoni, C. Ganzleben, E. Murphy, and K. Jurkiewicz. Towards a comprehensive noise strategy. *European Union, Brussels*, 2012.
- [4] R. Kim et al. Burden of disease from environmental noise. In *WHO International Workshop on “Combined Environmental Exposure: Noise, Air Pollutants and Chemicals” Ispra*, 2007.
- [5] W. Smeets, A. van Pull, H. Eerens, R. Sluyter, and G. de Hollander. Technical report on chemicals, particulate matter and human health, air quality and noise. *RIVM Rapport 481505015*, 2001.
- [6] O. Coussy. *Poromechanics*. John Wiley & Sons, 2004.
- [7] J. P. Arenas and M. J. Crocker. Recent trends in porous sound-absorbing materials. *Sound Vib.*, **44**(7):12–18, 2010.
- [8] F. J. Fahy. *Foundations of engineering acoustics*. Academic Press, 2000.
- [9] J. Allard and N. Atalla. *Propagation of sound in porous media: Modelling sound absorbing materials 2e*. John Wiley & Sons, 2009.
- [10] C. Perrot, F. Chevillotte, and R. Panneton. Bottom-up approach for microstructure optimization of sound absorbing materials. *J. Acoust. Soc. Am.*, **124**(2):940–948, 2008.
- [11] R. J. Brown. Connection between formation factor for electrical resistivity and fluid-solid coupling factor in Biot’s equations for acoustic waves in fluid-filled porous media. *Geophysics*, **45**(8):1269–1275, 1980.

- [12] D. L. Johnson, J. Koplik, and R. Dashen. Theory of dynamic permeability and tortuosity in fluid-saturated porous media. *J. Fluid Mech.*, **176**(1):379–402, 1987.
- [13] Y. Champoux and J. F. Allard. Dynamic tortuosity and bulk modulus in air-saturated porous media. *J. Appl. Phys.*, **70**(4):1975–1979, 1991.
- [14] J. F. Allard. Modelling sound absorbing materials: Propagation of sound in porous media. *Elsevier Applied Science Elsevier Science, New York*, 1993.
- [15] D. Lafarge, P. Lemarinier, J. F. Allard, and V. Tarnow. Dynamic compressibility of air in porous structures at audible frequencies. *J. Acoust. Soc. Am.*, **102**(4):1995–2006, 1997.
- [16] S. R. Pride, F. D. Morgan, and A. F. Gangi. Drag forces of porous-medium acoustics. *Phys. Rev. B*, **47**(9):4964, 1993.
- [17] A. Cummings and S. P. Beadle. Acoustic properties of reticulated plastic foams. *J. Sound Vib.*, **175**(1):115–133, 1994.
- [18] R. T. Muehleisen, C. W. Beamer IV, and B. D. Tinianov. Measurements and empirical model of the acoustic properties of reticulated vitreous carbon. *J. Acoust. Soc. Am.*, **117**(2):536–544, 2005.
- [19] A. Craggs and J. G. Hildebrandt. Effective densities and resistivities for acoustic propagation in narrow tubes. *J. Sound Vib.*, **92**(3):321–331, 1984.
- [20] M. Y. Zhou and P. Sheng. First-principles calculations of dynamic permeability in porous media. *Phys. Rev. B*, **39**(16):12027, 1989.
- [21] M. Firdaouss, J. L. Guermond, and D. Lafarge. Some remarks on the acoustic parameters of sharp-edged porous media. *Int. J. Eng. Sci.*, **36**(9):1035–1046, 1998.
- [22] X. Wang and T. J. Lu. Optimized acoustic properties of cellular solids. *J. Acoust. Soc. Am.*, **106**(2):756–765, 1999.
- [23] A. Cortis, D. M. J. Smeulders, J. L. Guermond, and D. Lafarge. Influence of pore roughness on high-frequency permeability. *Phys. Fluids*, **15**(6):1766–1775, 2003.
- [24] S. Gasser, F. Paun, and Y. Bréchet. Absorptive properties of rigid porous media: Application to face centered cubic sphere packing. *J. Acoust. Soc. Am.*, **117**(4):2090–2099, 2005.
- [25] C. Perrot, R. Panneton, and X. Olny. Periodic unit cell reconstruction of porous media: Application to open-cell aluminum foams. *J. Appl. Phys.*, **101**(11):113538, 2007.

- [26] C. Perrot, F. Chevillotte, M. T. Hoang, G. Bonnet, F. X. Bécot, L. Gautron, and A. Duval. Microstructure, transport, and acoustic properties of open-cell foam samples: Experiments and three-dimensional numerical simulations. *J. Appl. Phys.*, **111**(1):014911, 2012.
- [27] O. Doutres, N. Atalla, and K. Dong. A semi-phenomenological model to predict the acoustic behavior of fully and partially reticulated polyurethane foams. *J. Appl. Phys.*, **113**(5):054901, 2013.
- [28] J. H. Park, K. S. Minn, H. R. Lee, S. H. Yang, C. B. Yu, S. Y. Pak, C. S. Oh, Y. S. Song, Y. J. Kang, and J. R. Youn. Cell openness manipulation of low density polyurethane foam for efficient sound absorption. *J. Sound Vib.*, **406**(13):224–236, 2017.
- [29] K. Attenborough and I. L. Vér. Sound-absorbing materials and sound absorbers. *Noise and Vibration Control Engineering: Principles and Applications, Second Edition*, John Wiley & Sons, 2006.
- [30] F. Chevillotte and C. Perrot. Effect of the three-dimensional microstructure on the sound absorption of foams: A parametric study. *J. Acoust. Soc. Am.*, **142**(2):1130–1140, 2017.
- [31] I. Cantat, S. Cohen-Addad, F. Elias, F. Graner, R. Höhler, R. Flatman, O. Pitois, F. Rouyer, and A. Saint-Jalmes. *Foams: structure and dynamics*. Oxford University Press, 2013.
- [32] G Kirchhoff. On the influence of heat conduction in a gas on sound propagation. *Ann. Phys. Chem.*, **134**:177–193, 1868.
- [33] C. Zwikker and C. W. Kosten. *Sound absorbing materials*. Elsevier, 1949.
- [34] M. A. Biot. Theory of propagation of elastic waves in a fluid-saturated porous solid. I. low-frequency range. *J. Acoust. Soc. Am.*, **28**(2):168–178, 1956.
- [35] M. A. Biot. Theory of propagation of elastic waves in a fluid-saturated porous solid. II. higher frequency range. *J. Acoust. Soc. Am.*, **28**(2):179–191, 1956.
- [36] K. Attenborough. Acoustical characteristics of porous materials. *Phys. Rep.*, **82**(3):179–227, 1982.
- [37] K. Attenborough. Acoustical characteristics of rigid fibrous absorbents and granular materials. *J. Acoust. Soc. Am.*, **73**(3):785–799, 1983.
- [38] J. F. Allard, R. Bourdier, and C. Depollier. Biot waves in layered media. *J. Appl. Phys.*, **60**(6):1926–1929, 1986.

- [39] Y. Champoux and M. R. Stinson. On acoustical models for sound propagation in rigid frame porous materials and the influence of shape factors. *J. Acoust. Soc. Am.*, **92**(2):1120–1131, 1992.
- [40] M. E. Delany and E. N. Bazley. Acoustical properties of fibrous absorbent materials. *Appl. Acoust.*, **3**(2):105–116, 1970.
- [41] Y. Miki. Acoustical properties of porous materials-Modifications of Delany-bazley models. *JASJ*, **11**(1):19–24, 1990.
- [42] L. L. Beranek and I. L. Ver. Noise and vibration control engineering-principles and applications. *John Wiley & Sons, Inc.*, 814 p., 1992.
- [43] J. F. Allard and Y. Champoux. New empirical equations for sound propagation in rigid frame fibrous materials. *J. Acoust. Soc. Am.*, **91**(6):3346–3353, 1992.
- [44] I. P. Dunn and W. A. Davern. Calculation of acoustic impedance of multi-layer absorbers. *Appl. Acoust.*, **19**(5):321–334, 1986.
- [45] W. Qunli. Empirical relations between acoustical properties and flow resistivity of porous plastic open-cell foam. *Appl. Acoust.*, **25**(3):141–148, 1988.
- [46] N. Kino and T. Ueno. Evaluation of acoustical and non-acoustical properties of sound absorbing materials made of polyester fibres of various cross-sectional shapes. *Appl. Acoust.*, **69**(7):575–582, 2008.
- [47] D. Dragna, K. Attenborough, and P Blanc-Benon. On the inadvisability of using single parameter models to represent the acoustical properties of ground surfaces. *J. Acoust. Soc. Am.*, **138**(4):2399–2413, 2015.
- [48] N. Voronina. Acoustic properties of fibrous materials. *Appl. Acoust.*, **42**(2):165–174, 1994.
- [49] N. Voronina. An empirical model for rigid frame porous materials with high porosity. *Appl. Acoust.*, **51**(2):181–198, 1997.
- [50] N. Voronina. An empirical model for rigid-frame porous materials with low porosity. *Appl. Acoust.*, **58**(3):295–304, 1999.
- [51] N. Kino, G. Nakano, and Y. Suzuki. Non-acoustical and acoustical properties of reticulated and partially reticulated polyurethane foams. *Appl. Acoust.*, **73**(2):95–108, 2012.
- [52] H. T. Luu, R. Panneton, and C. Perrot. Effective fiber diameter for modeling the acoustic properties of polydisperse fiber networks. *J. Acoust. Soc. Am.*, **141**(6):EL96–EL101, 2017.

- [53] D. Lafarge. *Propagation du son dans les matériaux poreux à structure rigide saturés par un fluide viscothermique: Définition de paramètres géométriques, analogie électromagnétique, temps de relaxation*. PhD thesis, Le Mans, 1993.
- [54] R. W. Blanning. The construction and implementation of metamodels. *Simulation*, **24**(6):177–184, 1975.
- [55] K. Willcox and J. Peraire. Balanced model reduction via the proper orthogonal decomposition. *Aiaa J.*, **40**(11):2323–2330, 2002.
- [56] R. G. Regis and C. A. Shoemaker. Constrained global optimization of expensive black box functions using radial basis functions. *J. Global Optim.*, **31**(1):153–171, 2005.
- [57] A. OHagan. Bayesian analysis of computer code outputs: a tutorial. *Reliabi. Eng. Syst. Safe.*, **91**(10):1290–1300, 2006.
- [58] H. P. Bieker, O. Slupphaug, T. A. Johansen, et al. Real-time production optimization of oil and gas production systems: A technology survey. *SPE Prod. Oper.*, **22**(04):382–391, 2007.
- [59] T. D. Robinson, M. S. Eldred, K. E. Willcox, and R. Haimes. Surrogate-based optimization using multifidelity models with variable parameterization and corrected space mapping. *Aiaa J.*, **46**(11):2814–2822, 2008.
- [60] R. L. Hardy. Multiquadric equations of topography and other irregular surfaces. *J. Geophys. Res.*, **76**(8):1905–1915, 1971.
- [61] R. K. Goodrich and K. E. Gustafson. Weighted trigonometric approximation and inner-outer functions on higher dimensional Euclidean spaces. *J. Approx. Theory*, **31**(4):368–382, 1981.
- [62] I. M. Sobol. Sensitivity estimates for nonlinear mathematical models. *Matem. Model.*, **1**(4):407–414, 1993.
- [63] H. Rabitz, Ö. F. Aliş, J. Shorter, and K. Shim. Efficient input-output model representations. *Comput. Phys. Commun.*, **117**(1-2):11–20, 1999.
- [64] D. G. Krige. A statistical approach to some basic mine valuation problems on the witwatersrand. *J. S. Afr. I. Min. Metall.*, **52**(6):119–139, 1951.
- [65] R. Dawes, D. L. Thompson, A. F. Wagner, and M. Minkoff. Interpolating moving least-squares methods for fitting potential energy surfaces: A strategy for efficient automatic data point placement in high dimensions. *J. Chem. Phys.*, **128**(8):084107, 2008.
- [66] A. Ammar, B. Mokdad, F. Chinesta, and R. Keunings. A new family of solvers for some classes of multidimensional partial differential equations encountered in kinetic theory modeling of complex fluids. *J. Non-Newtonian Fluid*, **139**(3):153–176, 2006.

- [67] B. A. Le, J. Yvonnet, and Q. C. He. Computational homogenization of nonlinear elastic materials using neural networks. *Int. J. Numer. Meth. Eng.*, **104**(12):1061–1084, 2015.
- [68] A. Chkifa, A. Cohen, and C. Schwab. High-dimensional adaptive sparse polynomial interpolation and applications to parametric pdes. *Foundations of Computational Mathematics*, **14**(4):601–633, 2014.
- [69] A. Chkifa, A. Cohen, and C. Schwab. Breaking the curse of dimensionality in sparse polynomial approximation of parametric pdes. *Journal de Mathématiques Pures et Appliquées*, 103(2):400–428, 2015.
- [70] A. Chkifa, A. Cohen, G. Migliorati, F. Nobile, and R. Tempone. Discrete least squares polynomial approximation with random evaluations- application to parametric and stochastic elliptic pdes. *ESAIM: Mathematical Modelling and Numerical Analysis*, **49**(3):815–837, 2015.
- [71] M. Abramowitz and I. A. Stegun. *Handbook of mathematical functions: with formulas, graphs, and mathematical tables*, volume **55**. Courier Corporation, 1964.
- [72] M. Arnst and J. P. Ponthot. An overview of nonintrusive characterization, propagation, and sensitivity analysis of uncertainties in computational mechanics. *Int. J. Uncertain. Quan.*, **4**(5), 2014.
- [73] B. M. Van, M. Vargas, S. Inoue, Y. Yoshida, J. Perdigao, P. Lambrechts, and G. Vanherle. Microscopy investigations. Techniques, results, limitations. *Am. J. Dent.*, **13**(Spec No):3D–18D, 2000.
- [74] N. Kränzlin and M. Niederberger. Controlled fabrication of porous metals from the nanometer to the macroscopic scale. *Mater. Horizons*, **2**(4):359–377, 2015.
- [75] K. Gao, J. A. W. van Dommelen, and M. G. D. Geers. Microstructure characterization and homogenization of acoustic polyurethane foams: Measurements and simulations. *Int. J. Solids Struct.*, **100**:536–546, 2016.
- [76] M. Hiraiwa, M. A. Ghanem, S. P. Wallen, A. Khanolkar, A. A. Maznev, and N. Boechler. Complex contact-based dynamics of microsphere monolayers revealed by resonant attenuation of surface acoustic waves. *Phys. Rev. Lett.*, **116**(19):198001, 2016.
- [77] H. T. Luu, C. Perrot, V. Monchiet, and R. Panneton. Three-dimensional reconstruction of a random fibrous medium: Geometry, transport, and sound absorbing properties. *J. Acoust. Soc. Am.*, **141**(6):4768–4780, 2017.
- [78] E. B. Matzke. The three-dimensional shape of bubbles in foam-an analysis of the role of surface forces in three-dimensional cell shape determination. *Am. J. Bot.*, pages 58–80, 1946.

- [79] O. Doutres, N. Atalla, and K. Dong. Effect of the microstructure closed pore content on the acoustic behavior of polyurethane foams. *J. Appl. Phys.*, **110**(6):064901, 2011.
- [80] S. Beatriz, N. Luis, C. Leonor, M. Laura, M. Elena, and F. N. Yolanda. Imaging techniques and scanning electron microscopy as tools for characterizing a si-based material used in air monitoring applications. *Materials*, **9**(2):109, 2016.
- [81] L. Barguet, C. Pezerat, M. Bentahar, R. El Guerjouma, and V. Tournat. Ultrasonic evaluation of the morphological characteristics of metallic powders in the context of mechanical alloying. *Ultrasonics*, **60**:11–18, 2015.
- [82] M. Hiraiwa, S. P. Wallen, and N. Boechler. Acoustic wave propagation in disordered microscale granular media under compression. *Granul. Matter*, **19**(3):62, 2017.
- [83] V.H. Trinh, M. T. Hoang, C. Perrot, V. Langlois, Y. Khidas, and O. Pitois. A systematic link between microstructure and acoustic properties of foams: A detailed study on the effect of membranes. In *Poromechanics VI*, pages 1405–1412.
- [84] M. Joshi. *A class of stochastic models for porous materials*. University of Kansas, Chemical and Petroleum Engineering, 1974.
- [85] J. A. Quiblier. A new three-dimensional modeling technique for studying porous media. *J. Colloid Interf. Sci.*, **98**(1):84–102, 1984.
- [86] C.L.Y. Yeong and S. Torquato. Reconstructing random media. *Phys. Rev. E*, **57**(1):495, 1998.
- [87] K. K. Bodla, S. V. Garimella, and J. Y. Murthy. 3D reconstruction and design of porous media from thin sections. *Int. J. Heat Mass Tran.*, **73**:250–264, 2014.
- [88] A. P. Roberts and E. J. Garboczi. Elastic properties of a tungsten–silver composite by reconstruction and computation. *J. Mech. Phys. Solids*, **47**(10):2029–2055, 1999.
- [89] S. Adhikari and M. I. Friswell. Distributed parameter model updating using the Karhunen–Loève expansion. *Mech. Syst. Signal Pr.*, **24**(2):326–339, 2010.
- [90] J. Serra. *Image analysis and mathematical morphology*. Academic Press, 1983.
- [91] I. Malinetskaya, V. V. Mourzenko, J. F. Thovert, and P. M. Adler. Wave propagation through saturated porous media. *Phys. Rev. E*, **77**(6):066302, 2008.
- [92] C. Peyrega, D. Jeulin, C. Delisée, and J. Malvestio. 3D morphological characterization of phonic insulation fibrous media. *Adv. Eng. Mater.*, **13**(3):156–164, 2011.
- [93] P. Kumar and J. Topin, F. and Vicente. Determination of effective thermal conductivity from geometrical properties: application to open cell foams. *Int. J. Therm. Sci.*, **81**:13–28, 2014.

- [94] M. T. Hoang. *Modélisation et simulation multi-échelle et multi-physique du comportement acoustique de milieux poroélastiques: Application aux mousses de faible densité*. PhD thesis, Université Paris-Est, 2012.
- [95] K. Schladitz, S. Peters, D. Reinel-Bitzer, A. Wiegmann, and J. Ohser. Design of acoustic trim based on geometric modeling and flow simulation for non-woven. *Comp. Mater. Sci.*, **38**(1):56–66, 2006.
- [96] K. Cinar and I. Guven. Micro-computed tomography as a tool to investigate the deformation behavior of particulate-filled composite materials. *J. Eng. Mater. Technol.*, **140**(2):021001, 2018.
- [97] X. Sagartzazu, L. Hervella-Nieto, and J. M. Pagalday. Review in sound absorbing materials. *Arch. Comput. Method. E.*, **15**(3):311–342, 2008.
- [98] L. Egab, X. Wang, and M. Fard. Acoustical characterisation of porous sound absorbing materials: A review. *Int. J. Vehicle Noise Vib.*, **10**(1-2):129–149, 2014.
- [99] R. Panneton. Acoustics of porous materials: Experimental techniques. *Winter school on the Acoustics of Poro-Visco-Elastic Media*, 2013.
- [100] L. L. Beranek. Acoustic impedance of porous materials. *J. Acoust. Soc. Am.*, **13**(3):248–260, 1942.
- [101] Y. Champoux, M. R. Stinson, and G. A. Daigle. Air-based system for the measurement of porosity. *J. Acoust. Soc. Am.*, **89**(2):910–916, 1991.
- [102] Y. Salissou and R. Panneton. Pressure/mass method to measure open porosity of porous solids. *J. Appl. Phys.*, **101**(12):124913, 2007.
- [103] ASTM D6226-05. Standard test method for open cell content of rigid cellular plastics. Technical report, 2005.
- [104] Z. E. A. Fellah, W. Berger, Sand Lauriks, C. Depollier, and M. Fellah. Measuring the porosity of porous materials having a rigid frame via reflected waves: A time domain analysis with fractional derivatives. *J. Appl. Phys.*, **93**(1):296–303, 2003.
- [105] Z. E. A. Fellah, S. Berger, W. Lauriks, C. Depollier, C. Aristegui, and J. Y. Chapelon. Measuring the porosity and the tortuosity of porous materials via reflected waves at oblique incidence. *J. Acoust. Soc. Am.*, **113**(5):2424–2433, 2003.
- [106] T. Iwase, Y. Izumi, and R. Kawabata. A new measuring method for sound propagation constant by using sound tube without any air spaces back of a test material. In *INTER-NOISE and NOISE-CON Congress and Conference Proceedings*, volume 1998, pages 1265–1268. Institute of Noise Control Engineering, 1998.

- [107] X. Olny and R. Panneton. Acoustical determination of the parameters governing thermal dissipation in porous media. *J. Acoust. Soc. Am.*, **123**(2):814–824, 2008.
- [108] J. F. Allard, B. Castagnede, M. Henry, and W. Lauriks. Evaluation of tortuosity in acoustic porous materials saturated by air. *Rev. Sci. Instrum.*, **65**(3):754–755, 1994.
- [109] A. Schiavi, C. Guglielmono, P. Miglietta, and F. Alasia. Influence of static-load on airflow resistivity determination. *J. Acoust. Soc. Am.*, **123**(5):3764, 2008.
- [110] R. L. Brown and R. H. Bolt. The measurement of flow resistance of porous acoustic materials. *J. Acoust. Soc. Am.*, **13**(4):337–344, 1942.
- [111] ASTM C522. Standard test method for airflow resistance of acoustical materials. Technical report, 1990.
- [112] M. R. Stinson and G. A. Daigle. Electronic system for the measurement of flow resistance. *J. Acoust. Soc. Am.*, **83**(6):2422–2428, 1988.
- [113] P. Lemarinier, M. Henry, J. F. Allard, J. L. Bonardet, and A. Gedeon. Connection between the dynamic bulk modulus of air in a porous medium and the specific surface. *J. Acoust. Soc. Am.*, **97**(6):3478–3482, 1995.
- [114] M. Henry, P. Lemarinier, J. F. Allard, J. L. Bonardet, and A. Gedeon. Evaluation of the characteristic dimensions for porous sound-absorbing materials. *J. Appl. Phys.*, **77**(1):17–20, 1995.
- [115] P. Leclaire, L. Kelders, W. Lauriks, C. Glorieux, and J. Thoen. Determination of the viscous characteristic length in air-filled porous materials by ultrasonic attenuation measurements. *J. Acoust. Soc. Am.*, **99**(4):1944–1948, 1996.
- [116] P. Leclaire, L. Kelders, W. Lauriks, M. Melon, N. Brown, and B. Castagnede. Determination of the viscous and thermal characteristic lengths of plastic foams by ultrasonic measurements in helium and air. *J. Appl. Phys.*, **80**(4):2009–2012, 1996.
- [117] A. Moussatov, C. Ayrault, and B. Castagnède. Porous material characterization—ultrasonic method for estimation of tortuosity and characteristic length using a barometric chamber. *Ultrasonics*, **39**(3):195–202, 2001.
- [118] H. W. Chalkley, J. Cornfield, and H. Park. A method for estimating volume-surface ratios. *Science*, **110**(2856):295–297, 1949.
- [119] X. Olny, R. Panneton, and J. Tran-Van. An indirect acoustic method for determining intrinsic parameters of porous materials. In *2nd Biot conference on poromechanics, Grenoble, France*, pages 731–738, 2002.

- [120] R. Panneton and X. Olny. Acoustical determination of the parameters governing viscous dissipation in porous media. *J. Acoust. Soc. Am.*, **119**(4):2027–2040, 2006.
- [121] A. N. Gent and A. G. Thomas. The deformation of foamed elastic materials. *J. Appl. Polym. Sci.*, **1**(1):107–113, 1959.
- [122] A. N. Gent and A. G. Thomas. Mechanics of foamed elastic materials. *Rubber Chem. Technol.*, **36**(3):597–610, 1963.
- [123] V. A. Matonis. Elastic behavior of low density rigid foams in structural applications (low density rigid foam design for sandwich structure cores and yield stress for compressive loading). *SPE Journal*, 1964.
- [124] J. K. Weaver and J. Chalmers. Cancellous bone: Its strength and changes with aging and an evaluation of some methods for measuring its mineral content: I. age changes in cancellous bone. *JBJS*, **48**(2):289–299, 1966.
- [125] C. Perrot, F. Chevillotte, and R. Panneton. Dynamic viscous permeability of an open-cell aluminum foam: Computations versus experiments. *J. Appl. Phys.*, **103**(2):024909, 2008.
- [126] X. H. Yang, S. W. Ren, W. B. Wang, X. Liu, F. X. Xin, and T. J. Lu. A simplistic unit cell model for sound absorption of cellular foams with fully/semi-open cells. *Compos. Sci. Technol.*, **118**:276–283, 2015.
- [127] B. Buffel, F. Desplentere, K. Bracke, and I. Verpoest. Modelling open cell-foams based on the Weaire–Phelan unit cell with a minimal surface energy approach. *Int. J. Solids Struct.*, **51**(19):3461–3470, 2014.
- [128] W. S. Thomson. On the division of space with minimum partitional area. *Acta Math-Djursholm*, **11**(1-4):121–134, 1887.
- [129] A. M. Kraynik, D. A. Reinelt, and F. van Swol. Structure of random monodisperse foam. *Phys. Rev. E*, **67**(3):031403, 2003.
- [130] M. T. Hoang and C. Perrot. Solid films and transports in cellular foams. *J. Appl. Phys.*, **112**(5):054911, 2012.
- [131] L. Gong, S. Kyriakides, and W. Y. Jang. Compressive response of open-cell foams. part i: Morphology and elastic properties. *Int. J. Solids Struct.*, **42**(5):1355–1379, 2005.
- [132] J. Köll and S. Hallström. Generation of periodic stochastic foam models for numerical analysis. *J. Cell. Plast.*, **50**(1):37–54, 2014.
- [133] D. Weaire and R. Phelan. A counter-example to kelvin’s conjecture on minimal surfaces. *Phil. Mag. Lett.*, **69**(2):107–110, 1994.

- [134] P. Kumar and F. Topin. Influence of morphology on flow law characteristics in open-cell foams: An overview of usual approaches and correlations. *J. Fluid. Eng.*, **139**(7):071301, 2017.
- [135] K. A. Brakke. The surface evolver. *Exp. Math.*, **1**(2):141–165, 1992.
- [136] W. Y. Jang, A. M. Kraynik, and S. Kyriakides. On the microstructure of open-cell foams and its effect on elastic properties. *Int. J. Solids Struct.*, **45**(7):1845–1875, 2008.
- [137] N. Kino, G. Nakano, and Y. Suzuki. Non-acoustical and acoustical properties of reticulated and partially reticulated polyurethane foams. *Appl. Acoust.*, **73**(2):95–108, 2012.
- [138] M. T. Hoang, G. Bonnet, H. T. Luu, and C Perrot. Linear elastic properties derivation from microstructures representative of transport parameters. *J. Acoust. Soc. Am.*, **135**(6):3172–3185, 2014.
- [139] J. H. Park, S. H. Yang, H. R. Lee, C. B. Yu, S. Y. Pak, C. S. Oh, Y. J. Kang, and J. R. Youn. Optimization of low frequency sound absorption by cell size control and multiscale poroacoustics modeling. *J. Sound Vib.*, **397**(9):17–30, 2017.
- [140] E. Sánchez-Palencia. Non-homogeneous media and vibration theory. *Lect. Notes Phys.*, **127**, 1980.
- [141] C. Boutin, P. Royer, and J. L. Auriault. Acoustic absorption of porous surfacing with dual porosity. *Int. J. Solids Struct.*, **35**(34-35):4709–4737, 1998.
- [142] C. Y. Lee, Michael J. Leamy, and J. H. Nadler. Acoustic absorption calculation in irreducible porous media: A unified computational approach. *J. Acoust. Soc. Am.*, **126**(4):1862–1870, 2009.
- [143] M. Avellaneda and S. Torquato. Rigorous link between fluid permeability, electrical conductivity, and relaxation times for transport in porous media. *Phys. Fluids A-Fluid*, **3**(11):2529–2540, 1991.
- [144] D. Lafarge. Comments on “rigorous link between fluid permeability, electrical conductivity, and relaxation times for transport in porous media”. *Phys. Fluids A-Fluid*, **5**(2):500–502, 1993.
- [145] J. L. Auriault, L. Borne, and R. Chambon. Dynamics of porous saturated media, checking of the generalized law of Darcy. *J. Acoust. Soc. Am.*, **77**(5):1641–1650, 1985.
- [146] J. L. Auriault, C. Boutin, and C. Geindreau. *Homogenization of coupled phenomena in heterogenous media*, volume **149**. John Wiley & Sons, 2010.
- [147] O. Sen, S. Davis, G. Jacobs, and H. S. Udaykumar. Evaluation of convergence behavior of metamodeling techniques for bridging scales in multi-scale multimaterial simulation. *J. Comput. Phys.*, **294**:585–604, 2015.

- [148] P. Benner, A. Cohen, M. Ohlberger, and K. Willcox. *Model reduction and approximation: Theory and algorithms*, volume **15**. SIAM, 2017.
- [149] A. Chkifa, A. Cohen, and C. Schwab. High-dimensional adaptive sparse polynomial interpolation and applications to parametric PDEs. *Found. Comput. Math.*, **14**(4):601–633, 2014.
- [150] A. Chkifa, A. Cohen, G. Migliorati, F. Nobile, and R. Tempone. Discrete least squares polynomial approximation with random evaluations- application to parametric and stochastic elliptic PDEs. *ESAIM-Math. Model. Num.*, **49**(3):815–837, 2015.
- [151] T. J. Sullivan. *Introduction to uncertainty quantification*, volume **63**. Springer, 2015.
- [152] L. J. Gibson and M. F. Ashby. *Cellular solids: structure and properties*. Cambridge University Press, 1999.
- [153] N. C. Hilyard and A. Cunningham. *Low density cellular plastics: physical basis of behaviour*. Springer Netherlands, 1994.
- [154] W. E. Warren and A. M. Kraynik. The linear elastic properties of open-cell foams. *J. Appl. Mech.*, **55**(2):341–346, 1988.
- [155] A. Testouri, M. Ranft, C. Honorez, N. Kaabeche, J. Ferbitz, D. Freidank, and W. Drenckhan. Generation of crystalline polyurethane foams using millifluidic lab-on-a-chip technologies. *Adv. Eng. Mater.*, **15**(11):1086–1098, 2013.
- [156] J. L. Auriault. Dynamic behaviour of a porous medium saturated by a newtonian fluid. *Int. J. Eng. Sci.*, **18**(6):775–785, 1980.
- [157] C. Boutin. Rayleigh scattering of acoustic waves in rigid porous media. *J. Acoust. Soc. Am.*, **122**(4):1888–1905, 2007.
- [158] R. Burridge and J. B. Keller. Poroelasticity equations derived from microstructure. *J. Acoust. Soc. Am.*, **70**(4):1140–1146, 1981.
- [159] C. Peyrega and D. Jeulin. Estimation of acoustic properties and of the representative volume element of random fibrous media. *J. Appl. Phys.*, **113**(10):104901, 2013.
- [160] C. Perrot, F. Chevillotte, R. Panneton, J. F. Allard, and D. Lafarge. On the dynamic viscous permeability tensor symmetry. *J. Acoust. Soc. Am.*, **124**(4):EL210–EL217, 2008.
- [161] C. Perrot, R. Panneton, and X. Olny. Computation of the dynamic thermal dissipation properties of porous media by brownian motion simulation: Application to an open-cell aluminum foam. *J. Appl. Phys.*, **102**(7):074917, 2007.

- [162] C. Perrot, F. Chevillotte, and R. Panneton. Dynamic viscous permeability of an open-cell aluminum foam: Computations versus experiments. *J. Appl. Phys.*, **103**(2):024909, 2008.
- [163] O. Doutres, M. Ouisse, N. Atalla, and M. Ichchou. Impact of the irregular microgeometry of polyurethane foam on the macroscopic acoustic behavior predicted by a unit-cell model. *J. Acoust. Soc. Am.*, **136**(4):1666–1681, 2014.
- [164] C. Perrot, F. Chevillotte, M. T. Hoang, G. Bonnet, F. X. Bécot, L. Gautron, and A. Duval. Microstructure, transport, and acoustic properties of open-cell foam samples: Experiments and three-dimensional numerical simulations. *J. Appl. Phys.*, **111**(1):014911, 2012.
- [165] C. Chevillotte, F. Perrot and E. Guillon. A direct link between microstructure and acoustical macro-behavior of real double porosity foams. *J. Acoust. Soc. Am.*, **134**(6):4681–4690, 2013.
- [166] M. T. Hoang and C. Perrot. Identifying local characteristic lengths governing sound wave properties in solid foams. *J. Appl. Phys.*, **113**(8):084905, 2013.
- [167] M. T. Hoang and C. Perrot. Solid films and transports in cellular foams. *J. Appl. Phys.*, **112**(5):054911, 2012.
- [168] E. Lorenceau, N. Louvet, F. Rouyer, and O. Pitois. Permeability of aqueous foams. *Eur. Phys. J. E*, **28**(3):293–304, 2009.
- [169] Y. Khidas, B. Haffner, and O. Pitois. Capture-induced transition in foamy suspensions. *Soft matter*, **10**(23):4137–4141, 2014.
- [170] Y. Khidas, B. Haffner, and O. Pitois. Critical size effect of particles reinforcing foamed composite materials. *Compos. Sci. Technol.*, **119**:62–67, 2015.
- [171] K. Yasunaga, R. A. Neff, X. D. Zhang, and C. W. Macosko. Study of cell opening in flexible polyurethane foam. *J. Cell. Plast.*, **32**(5):427–448, 1996.
- [172] Y. Salissou and R. Panneton. Wideband characterization of the complex wave number and characteristic impedance of sound absorbers. *J. Acoust. Soc. Am.*, **128**(5):2868–2876, 2010.
- [173] S. Torquato. Relationship between permeability and diffusion-controlled trapping constant of porous media. *Phys. Rev. Lett.*, **64**(22):2644, 1990.
- [174] D. L. Weaire and S. Hutzler. *The physics of foams*. Oxford University Press, 2001.
- [175] *COMSOL Multiphysics® v.5.2 User's Guide*. Stockholm, Sweden, 2015.

- [176] Y. Achdou and M. Avellaneda. Influence of pore roughness and pore-size dispersion in estimating the permeability of a porous medium from electrical measurements. *Phys. Fluids A-Fluid*, **4**(12):2651–2673, 1992.
- [177] V. Langlois, V. H. Trinh, C. Lusso, C. Perrot, X. Chateau, Y. Khidas, and O. Pitois. Permeability of solid foam: Effect of pore connections. *Phys. Rev. E*, **97**(5):053111, 2018.
- [178] C. Lusso and X. Chateau. Disordered monodisperse 3D open-cell foams: Elasticity, thermal conductivity and permeability. *Poromechanics VI*, pages 1347–1354, 2017.
- [179] P. Kumar and F. Topin. Predicting pressure drop in open-cell foams by adopting forchheimer number. *Int. J. Multipha. Flow*, **94**:123–136, 2017.
- [180] M. P. Adler. Porous media: Geometry and transports. Butterworth/Heinemann, 1992.
- [181] G. Mavko and A. Nur. The effect of a percolation threshold in the Kozeny-Carman relation. *Geophysics*, **62**(5):1480–1482, 1997.
- [182] H. L. Frisch, J. M. Hammersley, and D. J. A. Welsh. Monte Carlo estimates of percolation probabilities for various lattices. *Phys. Rev.*, **126**(3):949, 1962.
- [183] H. K. Versteeg and W. Malalasekera. *An introduction to computational fluid dynamics: the finite volume method*. Pearson Education, 2007.
- [184] D. R. Durran. *Numerical methods for fluid dynamics: With applications to geophysics*, volume 32. Springer Science & Business Media, 2010.
- [185] T. Krüger, H. Kusumaatmaja, A. Kuzmin, O. Shardt, G. Silva, and E. M. Viggen. *The Lattice Boltzmann Method*. Springer, 2017.
- [186] S. Kirkpatrick. Percolation and conduction. *Rev. Mod. Phys.*, **45**(4):574, 1973.
- [187] A. P. Jivkov, C. Hollis, F. Etiese, S. A. McDonald, and P. J. Withers. A novel architecture for pore network modelling with applications to permeability of porous media. *Journal Hydrol.*, **486**:246–258, 2013.
- [188] P. Van Marcke, B. Verleye, J. Carmeliet, D. Roose, and R. Swennen. An improved pore network model for the computation of the saturated permeability of porous rock. *Transp. Porous Media*, **85**(2):451–476, 2010.
- [189] H. J. Vogel. A numerical experiment on pore size, pore connectivity, water retention, permeability, and solute transport using network models. *Eur. J. Soil Sci.*, **51**(1):99–105, 2000.

- [190] Q. Xiong, T. G. Baychev, and A. P. Jivkov. Review of pore network modelling of porous media: Experimental characterisations, network constructions and applications to reactive transport. *J. Contam. Hydrol.*, **192**:101–117, 2016.
- [191] Q. Xiong, C. Joseph, K. Schmeide, and A. P. Jivkov. Measurement and modelling of reactive transport in geological barriers for nuclear waste containment. *Phys. Chem. Chem. Phys.*, **17**(45):30577–30589, 2015.
- [192] I. Fatt et al. *The network model of porous media*. Society of Petroleum Engineers, 1956.
- [193] F. Hecht. New development in freefem++. *J. Numer. Math.*, **20**(3-4):251–266, 2012.
- [194] R. A. Sampson. On stokes’s current function. *Phil. T. Roy. Soc. A*, **182**:449–518, 1891.
- [195] I. E. Idelchik and E. Fried. *Handbook of hydraulic resistance*. Hemisphere, 1986.
- [196] P.A. J. Van Melick and B. J. Geurts. Flow through a cylindrical pipe with a periodic array of fractal orifices. *Fluid Dyn. Res.*, **45**(6):061405, 2013.
- [197] B. Berkowitz and R. P. Ewing. Percolation theory and network modeling applications in soil physics. *Surv. Geophys.*, **19**(1):23–72, 1998.
- [198] S. Galam and A. Mauger. Universal formulas for percolation thresholds. *Phys. Rev. E*, **53**(3):2177, 1996.
- [199] M. Sahimi, B. D. Hughes, L. E. Scriven, and H. T. Davis. Real-space renormalization and effective-medium approximation to the percolation conduction problem. *Phys. Rev. B*, **28**(1):307, 1983.
- [200] A. Okabe. *Spatial tessellations*. Wiley Online Library, 1992.
- [201] J. Feder. Random sequential adsorption. *J. Theor. Biolo.*, **87**(2):237–254, 1980.
- [202] A. V. Anikeenko, N. N. Medvedev, and T. Aste. Structural and entropic insights into the nature of the random-close-packing limit. *Phys. Rev. E*, **77**(3):031101, 2008.
- [203] D. Weaire and T. Aste. *The pursuit of perfect packing*. CRC Press, 2008.
- [204] W. S. Jodrey and E. M. Tory. Computer simulation of isotropic, homogeneous, dense random packing of equal spheres. *Powder Technol.*, **30**(2):111–118, 1981.
- [205] W. S. Jodrey and E. M. Tory. Computer simulation of close random packing of equal spheres. *Phys. Rev. A*, **32**(4):2347, 1985.
- [206] X. H. Yang, J. J. Kuang, T. J. Lu, F. S. Han, and T. Kim. A simplistic analytical unit cell based model for the effective thermal conductivity of high porosity open-cell metal foams. *J. Phys. D Appl. Phys.*, **46**(25):255302, 2013.

- [207] S. Krishnan, J. Y. Murthy, and S. V. Garimella. Direct simulation of transport in open-cell metal foam. *J. Heat Transf.*, **128**(8):793–799, 2006.
- [208] A. M. Kraynik, D. A. Reinelt, and F. van Swol. Structure of random foam. *Phys. Rev. Lett.*, **93**(20):208301, 2004.
- [209] Y. Hangai, K. Takahashi, T. Utsunomiya, S. Kitahara, O. Kuwazuru, and N. Yoshikawa. Fabrication of functionally graded aluminum foam using aluminum alloy die castings by friction stir processing. *Mat. Sci. Eng. A-Struct.*, **534**:716–719, 2012.
- [210] A. H. Brothers and D. C. Dunand. Density-graded cellular aluminum. *Adv. Eng. Mater.*, **8**(9):805–809, 2006.
- [211] P. A. Cundall and O. D. Strack. A discrete numerical model for granular assemblies. *Geotechnique*, **29**(1):47–65, 1979.
- [212] K. Hitti and M. Bernacki. Optimized dropping and rolling (ODR) method for packing of poly-disperse spheres. *Appl. Math. Model.*, **37**(8):5715–5722, 2013.
- [213] H. G. Matuttis and J. Chen. *Understanding the discrete element method: simulation of non-spherical particles for granular and multi-body systems*. John Wiley & Sons, 2014.